Ultrastructural Characterization of Cellular Interactions Within Resting, Developing and Tumorigenic Breast Epithelium

by

Danielle Mary Jorgens

A dissertation submitted in partial satisfaction of the

requirements for the degree of

Doctor of Philosophy

in

Comparative Biochemistry

in the

Graduate Division

of the

University of California, Berkeley

Committee in charge:

Professor Joe Gray, Co-Chair

Professor Fenyong Liu, Co-Chair

Professor Kenneth H. Downing

Professor Gary Firestone

Fall 2013

Ultrastructural Characterization of Cellular Interactions Within Resting, Developing and Tumorigenic Breast Epithelium

Danielle Mary Jorgens

Abstract

Ultrastructural Characterization of Cellular Interactions Within Resting, Developing and Tumorigenic Breast Epithelium
by

Danielle Mary Jorgens

Doctor of Philosophy in Comparative Biochemistry

University of California, Berkeley

Professor Joe Gray, Co-chair

Professor Fenyong Liu, Co-Chair

Epithelial to mesenchymal transition (EMT) and collective cell migration events are of interest for understanding cancer progression and metastasis. The use of in vitro cell lines to model these processes are widely used and help to shed light upon the mechanisms that lead to tumorigenesis. Here we use two such models: the human mammary epithelial cell line HMT-3522 and ex vivo mouse mammary primary culture epithelial organoids. The HMT-3522 cell line provides an encapsulated system to study cancer progression, however detailed ultrastructural analyses of this cell line are lacking. To study collective cell migration we used the murine ex vivo epithelial "organoid" system, which upon growth factor stimulation undergoes branching morphogenesis. Growth of these systems in 3D cell culture is an important component in understanding the highly dynamic and complex processes of EMT and collective cell migration. High resolution imaging via transmission electron microscopy and three dimensional scanning electron microscopy provide a way to discern ultrastructural features of both collective cell migration and EMT.

Electron microscopy imaging of the HMT-3522 S1 cell line, grown in 3D to form acini, demonstrated an abundance of membrane protrusions at all interior lateral and apical surfaces. Furthermore, these acinar structures were determined to have a semi-polarized state as defined by the appearance of a basement membrane, but lack all hallmarks of apical polarization. Three dimensional imaging of the membrane protrusions revealed they have a variety of lengths and an interdigitated nature. Determining this semi-polarized state to be more representative of a transitive tissue state, we sought to image the transient terminal end bud (TEB) of organoids undergoing branching morphogenesis. Ultrastructural analysis of in vivo murine mammary gland and ex vivo un-stimulated organoids revealed nearly identical tissue organization, with typical apico-basal polarity and almost no intercellular membrane protrusions. However, data of the stimulated organoids and specifically the TEB revealed a semi-polarized state of the cells very similar to the HMT-3522 S1 acini, with prolific membrane protrusions. Hypothesizing these membrane protrusions were aiding in normal collective cell migration, we investigated whether disruption of actin polymerization via drug treatments within the TEB would recapitulate the ultrastructure of the tumorigenic cell line HMT-3522 T4-2. RhoA kinase inhibition lead to a remarkably similar tissue and cellular morphology between the two cell types.

This work is dedicated to my parents, Steve and Anne, and my grandparents, Buck and Rosemary, for their invaluable support, love and commitment to my education and development; for giving me so much more than life, I am indebted to you all. And to Jonathan, your unending belief in me has kept me warm throughout my journey to the peak of Mordor and back.

Table of Contents

List of Figures

List of Symbols and Abbreviations

2D	Two dimensional
3D	Three dimensional
3D-SEM	Three dimensional scanning electron microscopy
α	alpha
α6β1 integrin`	Integrin, beta 1, extracellular matrix binding protein
β1-integrin	Integrin, beta 1, extracellular matrix binding protein
β	beta
°C	Degrees Centigrade
aPKC-ζ	Atypical protein kinase C
Apr2/3	Actin related proteins 2 and 3
ATP	Adenosine triphosphate
BSE	Back scattered electron (detection)
CCD	Charge-coupled device
Cdc42	Cell division cycle 42
DAPI	4',6-diamidino-2-phenylindole
DNA	Deoxyribonucleic acid
E-cadherin	Cadherin 1, type 1
E-cad	Cadherin 1, type 1
ECM	Extracellular matrix
EGF	Epidermal growth factor
EGFR	Epidermal growth factor receptor
EM	Electron microscopy (microscope)
EMT	Epithelial to mesenchymal transition
F-actin	Filamentous actin
FEG	Field emission gun
FEGSEM	Field emission gun scanning electron microscope
FIB-SEM	Focused ion beam scanning electron microscopy (microscope)
FS	Freeze substitution
GTPase	Guanosine triphosphatase
HER2	v-erb-b2 avian erythroblastic leukemia viral oncogene homolog 2
HMECs	Human mammary epithelial cells
HMT-3522	Human mammary epithelial tissue cell line series
HPF	High pressure freezing
HPF-FS	High pressure freezing-freeze substitution
kV	Kilovolt
keV	Kilo electron volt
M	Molar
MCF-10a	Michigan Cancer Foundation human breast adenocarcinoma line 10a
ML-7	Myosin light chain kinase inhibitor
MLCK	Myosin light chain kinase
mM	Millimolar
MMP14	Type 1 matrix metalloprotease 14 (aka MT1MMP)
MW	Microwave -assisted
MW-HPF-FS	Microwave assisted –high pressure frozen – freeze substituted
nm	Nanometer

nM	Nanomolar
N-WASP	Wiskott-Aldrich syndrome-like
NSC23766	Rac1 inhibitor
OTO	Osmium thiocarbohydrazide osmium
OTO-MW-HPF-FS	Microwave assisted –high pressure frozen – freeze substituted
pA	picoamp
Par3	Coagulation factor II receptor like-2
Par6	Partitioning defective 6 homolog alpha
Par/aPKC-ζ	Par3/Par6/aPKC complex
PIP_2	Phosphatidylinositol 4,5-bisphosphate
PL1	Power Level, setting 1
PLT	Progressively lowering temperature
PTEN	Phosphatase and tensin homolog
Rac1	Small GTPase
RhoA	Small GTPase
ROCK	RhoA kinase effector protein
ROI	Region of interest
ROTO	Ruthenium red-osmium thiocarbohydrazide osmium
rRNA	Ribosomal ribonucleic acid
S1	HMT-3522 wild type, non-malignant
S2	HMT-3522 subline 2, non-malignant
S3	HMT-3522 subline 3, non-malignant
SBF-SEM	Serial block face scanning electron microscopy (microscope)
SED	Secondary electron detector
SEM	Scanning electron microscopy (microscope)
SRC	Tyrosine kinase protein
T4-2	HMT-3522 malignant
TAO	Tannic acid osmium
TEB	Terminal end bud
TEM	Transmission electron microscopy (microscope)
TJ	Tight junction
TKS4	Adaptor proteins Tyr kinase substrate with four SH3 domains
TKS5	Adaptor proteins Tyr kinase substrate with five SH3 domains
μm	Micrometer
μM	Micromolar
v-SRC	Tyrosine kinase protein
WASP	Wiskott-Aldrich syndrome protein
WAVE	WASP family verprolin-homologous protein
Y27632	Inhibitor of RhoA kinase effector protein
ZO-1	Zona occludins protein 1

Acknowledgements

This work would not have been possible without the generous support, encouragement and instrumental collaborations of Dr. Manfred Auer, Dr. Kent McDonald, Dr. Andrew Ewald, Dr. Mina Bissell, Dr. Hildur Palsdottir and Dr. Joe Gray. Dr. Manfred Auer has nurtured me in research for nearly a decade; his enthusiasm, creativity and passion for science has been invaluable and has had dramatic influence on my life. In Dr. Kent McDonald I have found a kindred spirit and unparalleled creativity that is constantly inspiring.

Thank you to Dr. Joe Gray, Dr. Fenyong Liu, Dr. Ken Downing and Dr. Gary Firestone for their dedicated service on my dissertation committee. This overwhelming process felt possible due to your support, advice, critique and overall encouragement, thank you.

The following have provided experimental help, intellectual discussions, and/or encouragement and for this, and more, I am extremely grateful: Wenting Tsai, Kester Coutinho, Jamie Inman, Amita Gorur, Michael Joo, Dr. Zoltan Metlagel, Dr. Hildur Palsdottir, Dr. Alison Killilea, Dr. Jessie Lee, Melissa Perez, Amy Biddle, Timothy Chung, Monica Lin, Reena Zalpuri, Dr. Bernhard Knierim, Dr. Birgit Luef, Marcin Zemla, Purbasha Sarkar, Michelle Lim, Polly Huang, Nisreen Hejab, Mary Singer, Judieann Tadeo, Dr. Tamas Torok, Andrew Tauscher, Tom Goddard, Elena Bosneaga, Dr. Jeff Triffo, Yekaterina Miroshnikova, Dr. Valerie Weaver, Kevin Cheung, Dr. Zena Werb, Robert Huebner, Dr. Roseann Csientis, Dr. Claudia Uhde-Stone, Dr. Rick Webb, Dr. Bing Jap, Dr. Eva Nogales, and Dr. Andreas Stahl. A special thank you to Dr. George Sensabaugh, who, as my academic advisor, has been supportive, so very encouraging and has kept me focused.

Chapter 1.
Introduction to actin-rich protrusions of the breast

Introduction

The regulatory mechanism for mammary gland epithelia development is hypothesized to be the basis of mammary tumor development and metastasis. *Herein, we seek to place in vitro studies of cancer development into a physiologically relevant context via high-resolution electron microscopy*. A conspicuous feature we observed early on by transmission electron microscopy (TEM) within the cancer progression model HMT-3522 S1 was prolific intercellular membrane protrusions. A review of the literature revealed that studies of cancer progression focused heavily on roles of actin-rich protrusions such as invadopodia and filopodia and further digging led us to review early papers describing the develop of the murine mammary gland imaged by TEM in which intercellular membrane protrusions were a prominent, yet unexplained, component.

Therefore, we aim to address these questions: *(1) what are the ultrastructural characteristics of the non-malignant cancer model HMT-3522 S1 acinus? (2) do the ultrastructures of the HMT-3522 S1 acini and ex vivo culture models of mammary branching morphogenesis match the ultrastructure of the in vivo mammary gland? (3) can we characterize the protrusion features that are consistent between the representations of the mammary gland? and (4) does the tumorigenic HMT-3522 T4-2 colony share ultrastructural similarities with the ex vivo model of mammary gland development when actin polymerization is disrupted?*

The types of membrane protrusions likely to be involved in mammary epithelial development and cancer progression are invadopodia or podosomes, filopodia and microvilli. Cell signaling, cellular dynamics and architecture of epithelial cells has been widely demonstrated to be altered from *in vivo* by growth in 2D cell culture; current studies into epithelial cell mechanics and signal transduction now routinely use 3D cell culture microenvironments to simulate *in vivo* tissue tension (i.e. tensional homeostasis or dynamic reciprocity) (Nelson and Bissell, 2005; Paszek et al., 2005). Importantly, nearly all of the data describing actin-rich membrane protrusions comes from experiments with 2D cell culture and thus it remains largely unclear whether these structures are similar in morphology and function within the 3D context of tissues. Furthermore, past studies have been limited in the detection and characterization of actin-rich membrane protrusions due to the use of light microscopy imaging which due to the diffraction limit cellular features smaller than 200 nm can be difficult to image.

The specific context of the 3D cell culture environment has recently been demonstrated to influence the membrane protrusion migratory method utilized by cells. For example, in a 2012 study of fibroblasts cultured in a cell derived matrix versus collagen1 only matrix migrated via bleb-based lobopodia or the smoothly contoured lamellipodia, respectively (Petrie et al., 2012). A difference in elasticity of the matrices was determined to be the cause of this difference, with lobopodial migration occurring in cell derived matrix which has linear elasticity. This study underlines the concept that context matters for cellular dynamics. To that end, studying membrane protrusions in a 2D context provides limited data on cellular dynamics that occur in tissues (Serebriiskii et al., 2008). Additionally, as 3D cell culture does not directly recapitulate native tissues, it remains important to compliment experiments in 3D cell culture with *in vivo* studies as well.

The remainder of this chapter will focus on providing short reviews of mammary gland development, the cell culture systems used for our studies, and the various actin-rich protrusions.

Mammary gland development

The mammary gland develops from a thickening of the ectoderm, which forms a multi-layered knob-like structure that invades the mesenchymal layer upon which it sits (Hogg et al., 1983). During embryonic development, the knob elongates to form a solid cord of epithelial cells that branch out into the mesenchyme and the cords develop interior lumina, and by birth, these interconnecting tubes have formed the mammary gland (Hogg et al., 1983). In the development of murine mammary gland, by day 12 of fetal development the small spherical cluster of epithelial cells has formed as a knob situated between the ectoderm and mesenchyme, the boundary well defined by basement membrane of the former. Between days 12 and 15 the knob is pushed slightly further into the mesenchyme a neck forms between the knob and the ectoderm (Hogg et al., 1983). At day 15, a cleft has developed at the base of the knob where the basement membrane is now less distinct and intercellular spaces appear; also glycogen and keratin is increased in the cells of the neck and ectoderm. In day 16 and 17, solid cords bifurcate, originating from the cleft, to invade the mesenchyme; the intercellular spaces now have membrane protrusions extending into them and they are also observed in the neck of the gland (Hogg et al., 1983). At day 18, the cords and neck still have a cohesive outermost layer of cells while the interior cells are loosely connected across protrusion filled intercellular spaces. The branching of the cords is clear, but the body from which they protrude remains larger in size than the individual branches. By day 20, the intercellular spaces and small lumina have unified to form a single lumen surrounded by an ordered polarized epithelium 1-3 cell layers thick, which is separated from the mesenchyme by a once again well form basement membrane populated with plentiful hemidesmosomes (Hogg et al., 1983). Following birth around day 21, the mammary gland will remain largely inactive until puberty, 4-8 weeks later, whereupon substantial increases in steroidal hormones occur. It is in the post-natal period when the mammary gland is expounded upon, undergoing multiple morphogenesis cycles and modified further through the reproductive hormonal estrus cycle, pregnancy and lactation followed by involution (Sternlicht et al., 2006). During puberty, the resting ductal tree is stimulated by estrogen, insulin like growth factor and epidermal growth factor to elongate out into the extracellular matrix through branching morphogenesis (Hinck and Silberstein, 2005; Hovey et al., 2002). In pregnancy, milk secretion depends on stimulation from pituitary prolactin and progesterone that act to initiate side branching of the ductal tree, which will proceed to fill out the fat pad. Terminal alveoli, located at the end of ductal branches, generate milk proteins and cytoplasmic lipid droplets; upon progesterone decrease at birth, a mass synthesis of milk components ensues and is completed when suckling is stopped, thus causing the epithelium to undergo involution (Oakes et al., 2008; Watson, 2006).

Polarization of the mammary epithelium

The epithelium of the breast is a simple bilayered epithelia, defined by a single layer of luminal columnar epithelial cells, tightly connected through junctional complexes, surrounded by myoepithelial squamous supporting cells. In the breast, the epithelium is responsible for milk production during and following pregnancy. The resting epithelium forms a functional barrier between the lumen above the surface of the luminal cells (i.e. the space in which milk would be

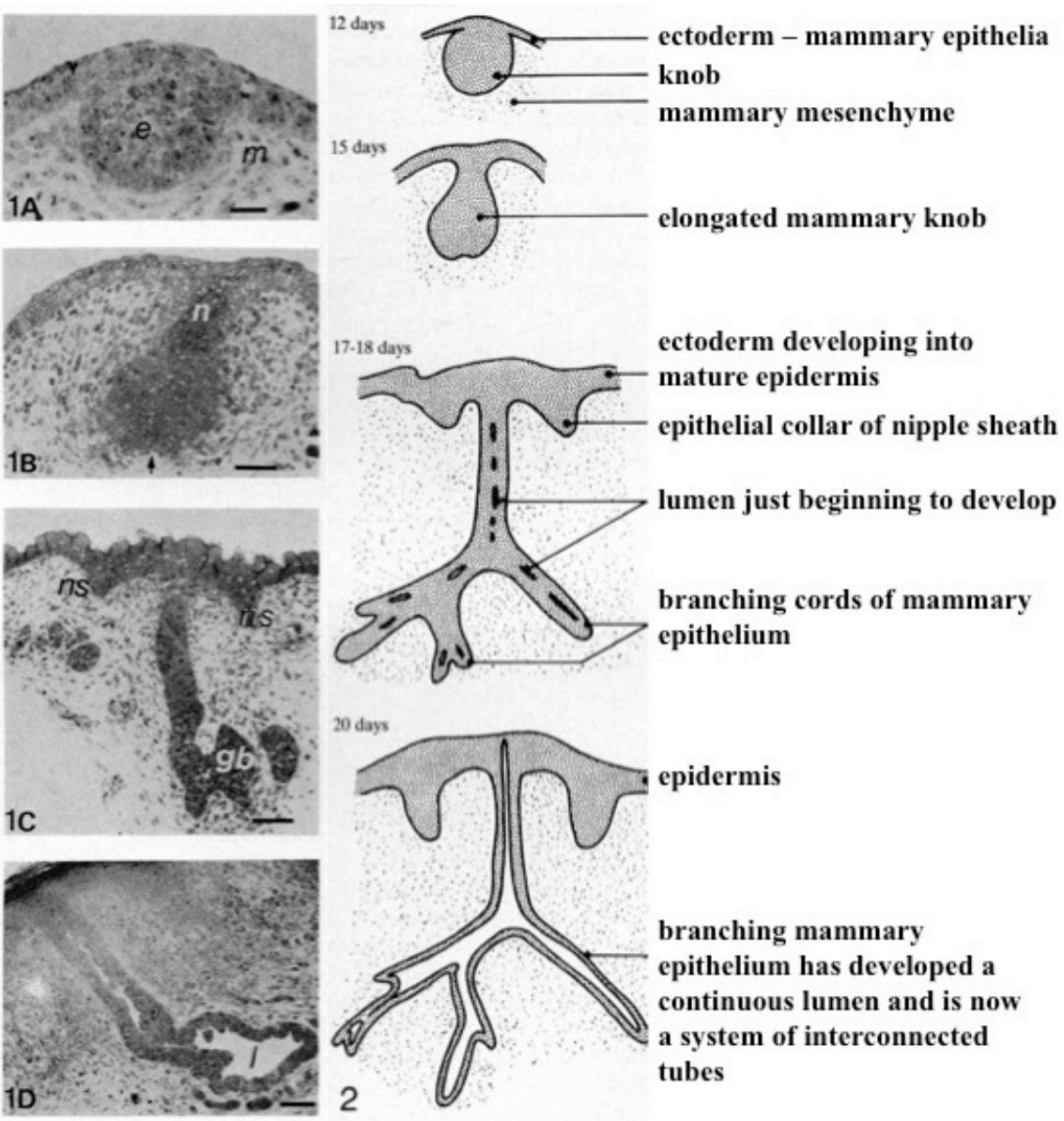

Figure 1. Overview of developing mammary gland. (1A) A 12-day mammary gland: an almost spherical knob of epithelial cells protruding from the ectoderm (e) into the mesenchyme (m). (1B) 15-day mammary gland: the gland has increased in size and a clear neck (n) is present. At the base of the knob is a small cleft (arrowed): the first sign of branching. (1C) 17-day mammary gland: branching is established. Note intercellular spaces within the gland body (gb). Localized proliferation of epithelial cells in the skin has led to the formation of the nipple sheath (ns). (1D) 20-day mammary gland with a continuous lumen (1) lined by a polarized epithelium one to three cells thick. (2) Sequence of diagrams showing the development of the mouse mammary gland. Scale bars: (A) = 10 μm; (B) = 20μm; (C) & (D) = 40 μm. Figure 1 was adapted from Hogg et al., 1983.

secreted during lactation) and the stromal tissue below the myoepithelial cells. Luminal epithelial cells display asymmetrical apico-basal polarization denoting this directionality. The apical surface typically corresponds to the area of the cell, which is exposed to external space concurrent with the outside environment (e.g. gut epithelia apical surface makes up the lining of a continuous tube running through the entire vertebrate body). On the basal side of the polarized epithelial cells lies a barrier, the basement membrane (or basal lamina) located between them and the ECM or stroma.

Polarization of epithelia is the result of a complex mixture of biochemical and mechanical signals from both the cell itself and the surround cells (Bryant and Mostov, 2008). Polarization provides a paracellular diffusion barrier to restrict external materials from the underlying cell space and tissue, resulting in spatial regulation of signaling complexes (Gibson and Perrimon, 2003; Vermeer et al., 2003). The sequence of events building of asymmetry begins with apical orientation being defined by the surrounding mechanical feedback whether it be from ECM or other cells (Bryant and Mostov, 2008). This is done through cell-ECM binding via integrin receptors at the cell surface, this promotes an enrichment of PIP_2 at the membrane by PTEN, establishing the initial apical orientation (Bryant and Mostov, 2008). Recruitment to the apical membrane by the PIP_2 binding protein annexin-2 of Cdc42 (a small GTPase) leads to the activation of the Par6/aPKC complex and binding of Par3 (Bryant and Mostov, 2008). Another driving factor in polarization at the cellular and tissue level are tight junctions (TJ), cell-cell adhesion structures that localize to the apical surface of an epithelial cell (Gibson and Perrimon, 2003). Localization of the polarity complex Par/aPKC (Par3/Par6/aPKC) to TJs plays an important role in both TJ formation and establishing cell polarity (Hurd et al., 2003).

Modeling breast epithelia in vitro

Ex vivo organoid system

The mouse mammary gland encompasses one of the best model systems for providing insight into human development, despite the fact that human mammary gland development and structure are divergent in many ways from the mouse (Daniel and Smith, 1999; Russo and Russo, 2004). Undoubtedly, the accessibility, drug-ability, genetic variety and robustness of sample size are features of mouse model that would be impossible to obtain within a human sample set for the study of breast development. Additionally, in the previous decade an explosion of imaging capabilities, cell culture technique, as well as biochemical and genetic techniques have brought the ability to study both mouse and human cell models *in vitro* under conditions that recapitulate *in vivo* conditions (Debnath et al., 2003; Ewald et al., 2008; Lee et al., 2007). These *ex vivo* and *in vitro* approaches span the range of small (tens of cells) to large scale (hundreds to thousands of cells) tissue features and architecture.

The murine *ex vivo* culture system is one of the most robust, versatile and physiologically representative mammary epithelium models. Optimized by the Werb group, the mammary gland of a mouse is dissected, diced and embedded into 3D extracellular matrix generating an "organoid" (Ewald et al., 2008; Ozzello, 1971). These organoids form bilayered cysts in the 3D cell culture matrix and can be stimulated with growth factors to expand into the surrounding ECM in a process called branching morphogenesis. The organoid system, in addition to many other three-dimensional culture systems, particularly those based on laminin-rich extracellular matrices, provides a way to directly visualize cell dynamics with light microscopy in real time in small scale tissues in near native states. These recapitulated tissue environments, with regulated variables, being *in vitro* are thus easily imaged by other types of microscopy, including electron

microscopy. As these organoids are easily treated by exogenous agents, they are an excellent tool to study features of developmental biology, in particular the epithelial to mesenchymal transition state the mammary epithelia transiently displays during branching morphogenesis.

Cancer progression model

As it is necessary to study normal development of tissues, the investigation of disregulation in tissue development must also be studied to provide insight into the disease

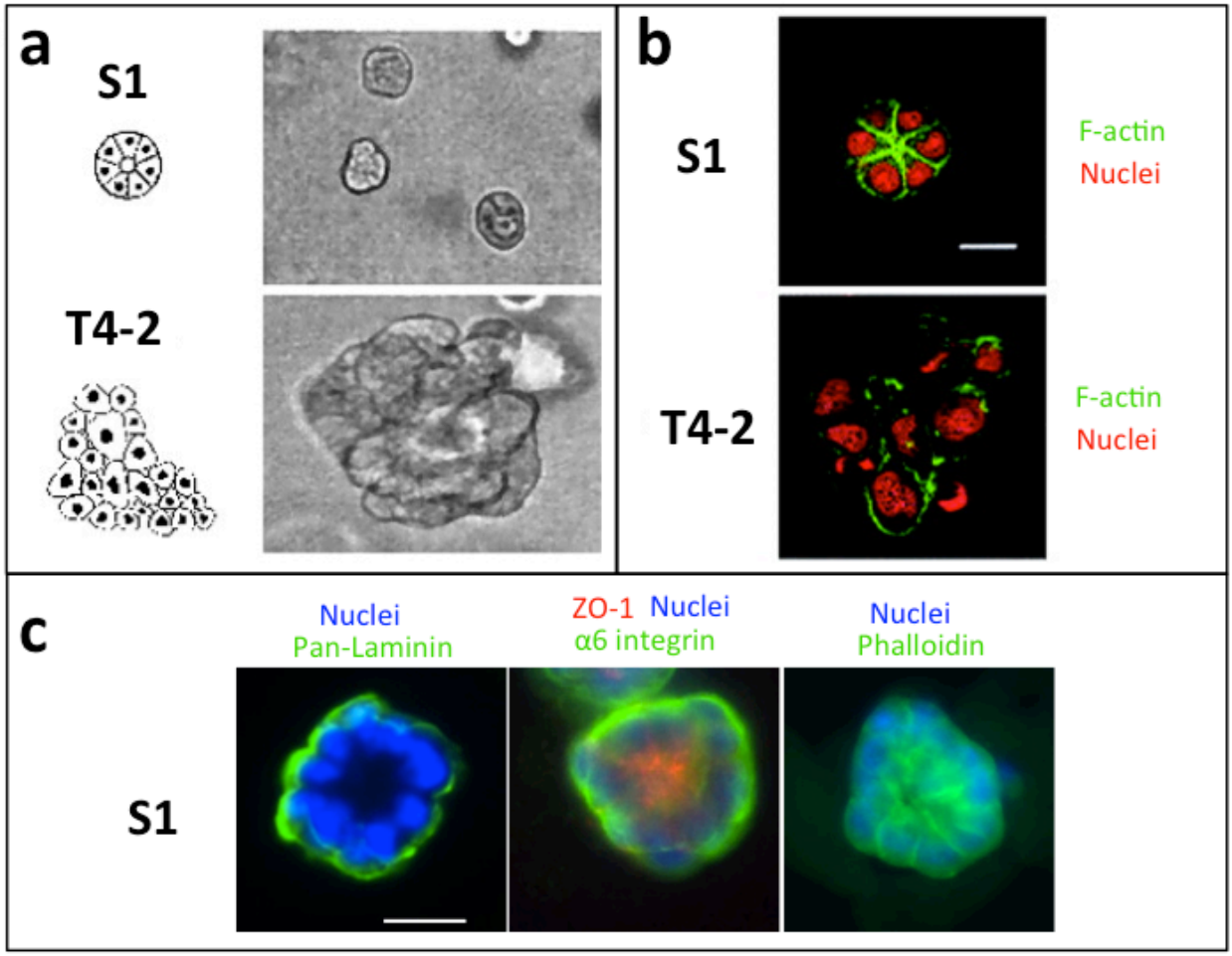

Figure 2. The HMT-3522 cancer progression cell lines "S1" and "T4-2". (A) Phase contrast images of S1 acini and a T4-2 colony grown embedded in 3D matrigel growth medium. A schematic of the overall organization is on the left. (B) Confocal images of S1 and T4-2 organization with immunofluorescence labeling of F-actin (green, fluorescein isothiocyanate) and nuclei (red) labeled with propidium iodide. Cells were grown embedded in 3D matrigel medium, 5 μm cryo-sections were stained for confocal imaging. The largely apico-lateral organization of the F-actin in S1 is used as a hallmark for polarization. (A) and (B) adapted from Figure 2 of (Wang et al., 1998). (C) Confocal images of three separate S1 acini. Cells were grown embedded in 3D matrigel medium, 5 μm cryo-sections were stained for immunofluorescence imaging. Laminin (ECM component) and α6-integrin (ECM receptor) display basal localization while phalloidin (F-actin) and ZO-1 (tight junction component) display apico-lateral organization. Images in (C) courtesy of Jamie Inman.

development. Cancer has long been thought to be a result of disregulation of normal development. In vitro cell culture systems are an important tool used to model both the development of and progression toward invasion of breast cancer cells. An important *in vitro* system, which has been well characterized genetically and phenotypically is the human mammary epithelial cell line HMT-3522. Uniquely, this *in vitro* model system encapsulates the spontaneous progression toward malignancy in human mammary epithelia, a departure from the more commonly used transgenic transition. First developed from a reduction mammoplasty of a patient with fibrocystic disease in the 1980's, the epithelial portion of the breast tissue gave rise to the immortalized wild type cell line called S1 (Briand et al., 1987). The S1 cell line is epidermal growth factor dependent, non-malignant, nearly diploid, and when grown in three-dimensional laminin rich medium forms growth-arrested acini displaying differentiation markers of polarization which are very similar to normal *in vivo* breast epithelium (Petersen et al., 1992). Furthermore, S1 cells grown in 3D ECM cell culture have been genetically validated as suitable model for breast cancers with good prognoses (Fournier et al., 2006). Continuing cell cycle passages of the S1 cell line led to the development of a subline, designated S2, which could grow without the addition of EGF to the medium (Madsen et al., 1992). Further culturing of the S2 subline without EGF and subsequent mouse xenografts revealed the development of a highly tumorigenic transformed cell line, called T4-2 (Briand et al., 1996). The T4-2 cell line was discovered to have lost EGF sensitivity and acquired an extra chromosome 7p, which contains the EGF receptor gene. Distinct differences between the S1 and T4-2 cell line are demonstrated by growth in 3D ECM due to the dramatic loss of tissue polarity, distinct macroscopic morphologies and high invasive potential of the T4-2 cell line (Briand et al., 1996; Kenny et al., 2007; Weaver et al., 1997). The T4-2 cells, grown in 3D ECM, also fail to growth arrest. In a large scale morphological classification of multiple human mammary epithelial cells (HMECs), the S1 and T4-2 cells grown in 3D ECM were found to have a basal B molecular subtype displaying round and mass-like phenotypes, respectively (Kenny et al., 2007; Neve et al., 2006). The evaluation of morphologies of the HMT-3522 cell lines in relation to each other and *in vivo* tissue has almost exclusively been performed using light and fluorescence microscopy.

A short review of actin-rich membrane protrusions

Microvilli and Filopodia

Filopodia are finger-like protrusion adhered to the ECM or other cells. Microvilli are also finger-like protrusions but they do not adhere to other structures. Microvilli and filopodia are structurally very similar, sharing many of the same molecular features and morphologically they can be indistinguishable. Each structure has been described as an actin-rich membrane protrusion, with an actin core of 10-30 filaments. This actin core and the general similarity in shape is the cause for the speculative hypothesis that microvilli and filopodia share the same regulator of assembly (Khurana and George, 2011). Both structures can use, but do not require the WAVE or Arp2/3 actin nucleating complex for assembly or elongation and have common actin cross-linker proteins (DeRosier and Tilney, 2000; Steffen et al., 2006; Svitkina and Borisy, 1999).

Microvilli are consistent in length and diameter, particularly at the brush border of gut epithelia. Occurring exclusively on differentiated cells, microvilli are thought to have a role in gating of ion fluxes, calcium signaling, volume regulation, and regulation of substrate transport (Lange, 2011). Some cells have highly specialized microvilli, which are capable of

mechanotransduction (hair cells) or perceiving light (photoreceptors) or chemical gradients (taste sensor cells). These specialized microvilli have provided fundamental insight into general mechanisms of microvilli regulation. A current hypothesis for microvillar formation is the stabilization of exocytic vesicles at the plasma membrane, which also leads to the enrichment of microvilli in integral membrane proteins (Lange, 2011). Stabilization of the microvillus is promoted by the linkage of myosin tails to the microvillar membrane, via PIP_2 clusters, and to filamentous actin. Actin treadmilling, lead by membrane anchored myosin along actin filaments, causes microvilli elongation and the overall length of the structure is highly dependent on the number of myosin, meaning the more myosin present the longer the microvillus (Rzadzinska et al., 2004). The core of the microvillus is made up of an actin bundle with 10-30 actin filaments oriented with the plus-end toward the tip of the microvillus. Tips of microvilli are thought to be enriched with membrane proteins and these tips have been demonstrated to shed as vesicles upon ATP stimulation, which causes plus-end directed migration of membrane components (McConnell and Tyska, 2007). The retrograde movement of membrane proteins toward the base can be accomplished by myosin VI.

The shape, size and dynamics of filopodia can range widely depending on the cell type and circumstance of the cell growth. In contrast with microvilli, filopodia are employed by undifferentiated cells or cells that are in a state of movement (Khurana and George, 2011). Filopodia are largely restricted in occurrence to epithelial cells. Initiation of filopodia can be accomplished by actin bundling that causes a protrusion under the membrane; this essential step of actin bundling is done by either fascin, villin or espin. These protrusions are necessary for creating or enabling cell-cell contact between the layers of epithelia, guiding in cell motility and establishing cellular contact with the extracellular matrix (Galbraith et al., 2007; Raich et al., 1999; Vasioukhin et al., 2000). At the tips of filopodia, ECM binding proteins are observed to be enriched in 2D monolayer culturing; whereas in 3D cell culture these adhesive proteins are observed along the length of a protruding filopodium (Shibue et al., 2012). Filopodia are also involved in extensive cell-cell contact. Adhesion zippering is a well documented process in which filopodia from adjacent cells interlock allowing E-cadherin proteins to bind and ultimately these binding sites mature into adherens/tight junctions. Interestingly, filopodia have also been observed to shed vesicles from their tips, often over very long distances as observed in *Xenopus* blastomeres (Danilchik and Brown, 2008).

Invadopodia and Podosomes

Originally described in 1980, podosomes form a rosette arrangement of focal adhesions on the ventral surface of cells grown in 2D cell culture (David-Pfeuty, 1980). Closely following this discovery, similar feet-like cellular protrusions were observed to colocalize to sites of ECM degradation and these protrusions were thusly named invadopodia (Chen, 1989; Tarone et al., 1985). The tips of these podosome and invadopodia structures were discovered to be enriched with v-SRC (a tyrosine kinase) at sites of ECM degradation and they have been found in a variety of cell types and tumors and are therefore thought to be used by tumor cells to intravasate surrounding ECM and for metastasis (Eckert et al., 2011). The nomenclature typically follows that invadopodia refer to protrusions of tumorigenic cells or tumors and podosome references protrusions of normal cells (Murphy and Courtneidge, 2011).

However, current evidence suggests that invadopodia and podosomes are either identical structures or share much of the same regulators for assembly, elongation and function (Gimona et al., 2008; Murphy and Courtneidge, 2011). Both consist of an actin-rich core of unbranched or

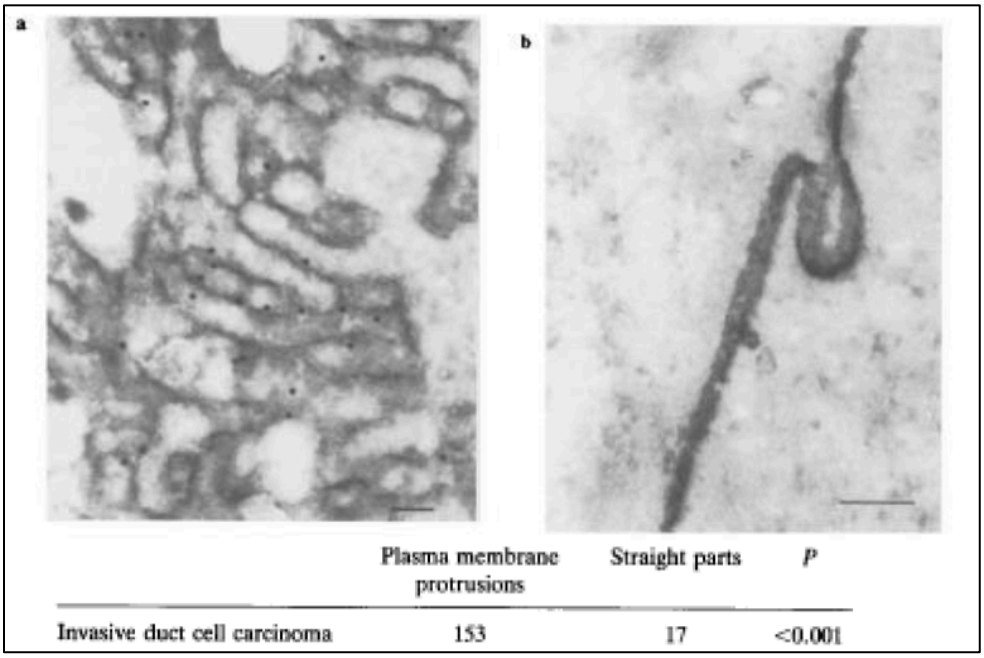

Figure 3. Filopodia-like protrusions in breast cancer tissue. (a-b) Immunogold labeling for HER2 receptor demonstrates 9X higher preferential labeling at intercellular filopodia as compared to straight cell-cell interfaces. Adapted from Figure 1 of (Potter and Quatacker, 1993).

branched filaments surrounded by adhesion proteins common to focal adhesion sites (β1-integrin) and scaffolding proteins that link the actin core to the surrounding plasma membrane (Murphy and Courtneidge, 2011). Most data for podosomes and invadopodia come from 2D cell culture experiments, which have yet to be robustly reproduced 3D culture or *in vivo*. Thus leaving open the question of culturing conditions influencing the reported similarities and differences, such as whether both structures are involved in ECM degradation. Furthermore, 2D microscopy and a few immunohistochemical markers are the currently the only methods used to classify and characterize the different types of actin-rich protrusions.

Some specific characteristics of the two structures include the actin rich center with actin turnover occurring on the scale of minutes to hours, various actin nucleators (Arp2/3, WAVE), actin binding proteins and kinases (Gimona et al., 2008). Proposed unique and important components of the protrusions include TKS4 and TKS5 (both of which are tyrosine kinase adaptor proteins), SRC (a tyrosine kinase), MMP14 (aka, MT1MMP, a type 1 matrix metalloprotease), cortactin (actin regulator) and N-WASP (neural Wiskott-Aldrich syndrome protein, an actin regulator) (Murphy and Courtneidge, 2011). Invadopodia formation requires the SRC family kinase mediated tyrosine phosphorylation of TKS4, TKS5, cortactin (Eckert et al., 2011). Extracellular matrix degradation occurs via multiple matrix metalloproteases, the most important for invadopodial function being MMP14 (Linder, 2007). To date few studies have viewed invadopodia directly with TEM, although the intriguing results of these studied led to the discovery that mature invadopodia, with a lifetime of multiple hours, can also have intermediate filaments and organelles within the actin rich core and can be bifurcated (Schoumacher et al., 2010; Tolde et al., 2010).

Significance in breast cancer

Morphogenesis of the mammary gland has long raised questions about whether the cell layer invasion required for this normal development may be related to the mechanisms of solid tumor formation, intravasation and metastasis. Cellular motility of epithelial cells is a complex and plastic process that provides cells wide-ranging abilities such as forming tissues or even breaking away from an established epithelium during early tumor metastasis. Such processes occur by either single cell or multicellular motility. An epithelial cell which breaks away from an established epithelium to move individually is consider to have undergone an epithelial to mesenchymal transition (EMT). Whereas epithelial cells moving as clusters, tubes or sheets, of 2 or more cells are utilizing a strategy called collective cell migration (Ewald et al., 2008; Friedl and Gilmour, 2009). Collective cell migration occurs when cells maintain adhesive apico-lateral junctional complexes and consistent positions to move in a coherent directional manner (Friedl and Gilmour, 2009; Ilina and Friedl, 2009). Both EMT and collective cell migration have strongly been indicated to promote and play crucial roles in tumorigenesis and metastasis. Evidence suggests that invadopodia and podosomes play a role in the first steps of an epithelial cell physically intravasating through the basement membrane of the mammary epithelium and is hypothesized to play a role during the EMT of early mammary tumors (Eckert et al., 2011). Filopodia and filopodium-like structures have also been implicated in tumor metastasis and progression and are known sites of tumor promoting cell receptors such as HER family receptors (Potter and Quatacker, 1993; Shibue et al., 2012).

Chapter 2.
Ultrastructure of HMT-3522 acini

Introduction

Research utilizing the HMT-3522 cell lines (S1, S2, S3 and T4-2) has increased in the past decade and focused on their potential to model breast cancer progression. Growth of these cells upon or within 3D extracellular matrix substrates that recapitulate physiological stiffness of the stromal tissue of the mammary gland reveal that they form small spheroid structures (Rizki et al., 2008; Weaver et al., 1995). Thorough genetic and phenotypic analyses of the S1, S2, S3 and T4-2 cells grown in 3D cell culture established that they can model *in vivo* breast cancer progression within an *in vitro* system (Kenny et al., 2007; Lee et al., 2007; Neve et al., 2006). It was demonstrated that the HMT-3522 cell lines are suitable models for particular subtypes (4 molecular subtypes are luminal A, luminal B, basal-like, HER2-type) of breast cancer, basal-like, which either have been difficult to immortalize in cell culture from patient samples or have not had a previous model system that could recapitulate that type of cancer *in vitro* (Neve et al., 2006; Rizki et al., 2008). The analysis of the S1 cell line suggested that it is genotypically and phenotypically similar to an acinar feature found at the end of the polarized simple epithelia of the mammary duct. This suggested that the S1 cell line, when grown in 3D culture conditions to form an acinus, could act as the normal control of any experiment involving the HMT-3522 lines (Briand et al., 1987; Weaver et al., 1995). The identification of the S1 acinus as a normal, physiologically relevant structure, was done in large part through immunofluorescence studies which localized proteins, such as ZO-1, β-catenin, E-cadherin, actin, keratins, to particular regions within the acini thus indicating the structure was polarized.

Polarization of epithelia refers to the cells' pre-determined arrangement where the apical (top) surface of the cell contains microvilli and the Golgi organelle's vesicular traffic travels toward this apical surface. At the apical surface, the cells have formed around an enclosed space called the lumen. In S1 acini, the lumen forms when cells within the middle of the spheroid lose contact with the cells surrounding them and undergo programmed cell death. Also, the apico-lateral surfaces (the sides of the cell toward the top) are tightly chained together by tight and adherens junctions, which contain ZO-1, β-catenin and E-cadherin molecules, responsible for linking the actin cytoskeleton from one cell to another. These tight junctions are also barriers between the material that lay above the cells within the lumen and the material below the epithelial cell, either the stroma or the myoepithelial cell. At the apical surface, the cells form around an enclosed space called the lumen. In S1 acini, the lumen forms when cells within the middle of the spheroid lose contact with the cells surrounding them and undergo programmed cell death.

On the basal side of the polarized epithelial cells lies a physical barrier, the basement membrane (or basal lamina) located between them and the ECM or stroma. In tissue, the barrier is constructed by the myoepithelial cells, or supporting cells, that have a fibroblastic morphology and hug closely to the basal side of multiple epithelial cells at once. The basement membrane is made of laminin 1, a protein that is secreted from the S1 cells basally and assembled into this barrier structure. In vitro cultures of S1 acini are typically one cell deep between the lumen and basement membrane. S1 cells are able to remodel extracellular matrix, a substance derived from mouse sarcoma cells composed of a complex assortment of ~60% laminin, ~ 30% collagen IV,

~8% entactin (which links laminin and collagen), and small quantities of a variety of growth factors, plasminogen activator, and fibronectin (Orkin, 1977). The commercially available BD Matrigel™ is generated by large-scale cell culture of Engelbreth-Holm-Swarm mouse sarcoma cells, which secrete and release vast quantities of the basement membrane components, which can then be harvested from the top of the 2D cell culture. Remodeling appears to occur through the release of matrix metalloproteases, such as MMP14, which degrade the matrix components, specifically fibronectin and collagen. Upon degradation, interaction with membrane proteins such as $\alpha 6\beta 1$ -integrin and uPAR allows the matrix components to rearrange into the basement membrane, thus creating a barrier for the epithelial cells to the stroma. Hemi-desmosomes establish a physical link between this barrier layer, the stroma and the epithelial cell.

Again, most data on S1 acini, specifically evidence for its polarization, has come from detailed immunofluorescence studies with, at best, 3D confocal imaging. However, the resolution of these imaging techniques are limited to 200 nm at best, and as with any kind of fluorescence imaging, the data collected only reflects the location of the fluorophore. These types of studies are limited by a lack of perspective. With an imaging technique like TEM, one can immediately survey the entirety of a cell, or even tissue, collecting data on nearly every kind of molecule within the cell as well as its location and neighbors. Beyond the advantage of gathering information on all structures contained within a cell or tissue, the resolution of this information is 100 fold superior to light microscopy as TEM tomography is capable of obtaining 2nm X-direction and 2nm Y-direction resolution.

Recent ultrastructural TEM-based studies of other types of epithelial cells that form acinar structures in 3D cell culture have proved to be enlightening. Specifically recent analyses of another HMEC, MCF-10a cells, demonstrating a semi-polarized state when cells were grown in 3D culture (Underwood et al., 2006). Therefore, we decided to perform an ultrastructural characterization of the 3-dimensionally grown and growth arrested S1 acini to map out features of polarization within the structure. What we discovered upon looking deep inside the S1 acinus was far more complicated than could have been anticipated from light microscopy studies. We found the cells of the acini had features of being only partially polarized and often displayed characteristics thought only to be found in malignant epithelial phenotypes consistent with epithelial to mesenchymal transition.

Experimental Procedures

HMT-3522 cell culture

2D cell culture: HMT-3522 mammary epithelial cells (Briand et al 1987, 1996) were grown on Falcon tissue culture plastic flasks as two dimensional (2D) monolayers in H14 medium (see Blaschke et al 1994). H14 medium is composed of DMEM:F12 medium (UCSF Cell Culture Facility) with 250ng/ml insulin (Sigma), 10ug/ml transferrin (Sigma), 2.6ng/ml sodium selenite (Sigma), 10^{-10} M estradiol (Sigma), 1.4 X 10^{-6} M hydrocortisone (Sigma) and 5ug/ml prolactin (Sigma). The S1 cells were propagated on Falcon tissue culture plastic with the addition of 10ng/ml of epidermal growth factor (EGF; Sigma) to the H14 medium.

3D cell culture: Three dimensional (3D) cultures were constructed using confluent 2D monolayers of S1 cells. Cells were trypsinized with trypsin-EDTA (UCSF Cell Culture Facility), trypsin was quenched with Soybean Trypsin Inhibitor (SBTI, Sigma), cells were counted and the desired number of cells was spun down into a pellet. S1 cells were plated into 3D at 0.8 million cells per milliliter of matrigel. Each assay was composed with the appropriate number of pelleted

cells (240K of S1) resuspended into 300ul of matrigel and pipetted into a 4-well Nunc plate (1.9cm^2/well) that had been pre-coated with 50ul of matrigel to prevent invasion to the bottom plastic surface. The matrigel assays were placed into a 37˚C incubator for 30 minutes for the matrigel to polymerize. The assays were fed with 500ul H14 medium. The S1 cells were fed with H14 + EGF as described above. Assay medium was changed every 2-3 days. The assays were harvested after 10 days of growth.

High pressure freezing and freeze substitution

HMT-3522 S1 acini, unfixed in matrigel were placed 1 mm wide by 200 μm deep aluminum freezing hats, and prior to freezing were surrounded with 20% bovine albumin as a cryoprotectant. The acini were then cryo-immobilized using a BAL-TEC HPM-010 high-pressure freezer (BAL-TEC, Inc., Carlsbad, CA). The samples were placed in freeze-substitution medium made up of 1% osmium tetroxide, 0.1% uranyl acetate, and 5% ddH_2O in acetone. All samples were freeze-substituted either using a Leica AFS2 (Leica Microsystems, Vienna, Austria) following a previously described protocol (McDonald, 2007) or by a method of super quick freeze substitution (McDonald and Webb, 2011). Upon completion of freeze-substitution, the "unfixed" acini samples were rinsed five times in pure acetone and then progressively infiltrated with an epon-araldite resin (McDonald and Muller-Reichert, 2002). All samples were flat embedded between two slides using two layers of parafilm as a spacer before being polymerized in an oven at 60° C overnight (Muller-Reichert et al., 2003).

Transmission electron microscopy

80 to 90 nm thin sections were generated using a Reichert Ultracut Ultramicrotome (Leica Microsystems, Wetzlar, Germany) and then collected onto formvar coated rhodium reinforced copper 2 mm slot grids. The grids were not post-stained. The sections were imaged using a FEI Tecnai 12 TEM (FEI, Eindhoven, The Netherlands) and images were recorded using a Gatan CCD with Digital Micrograph software (Gatan Inc., Pleasanton, CA). ImageJ software and Adobe Photoshop CS4 were used for further image processing (Abramoff Magelhaes, P. J., Ram, S. J., 2004; Adobe Systems Inc., San Jose, CA).

Results

Our first observations of the S1 acini came from slicing and staining 250-500 nm thick sections with toluidine blue, which allowed us to see that small spherical multicellular structures had been successfully infiltrated and embedded in resin. Thin sections of these blocks ranged from 80-100 nm and revealed a similar story in the TEM images. The variety of acini sizes, apparent from the macro-level light microscopy, was confirmed via TEM and ranged between 30-80 microns in diameter and contained 5-12 cells per structure. Due to this variety, we chose to selectively collect TEM data on mid-sized acini, which typically had ~10 cell per structure and were 40-50 microns in diameter. This midrange of size was consistent with the confocal imaging studies previously performed on the acini.

Next we sought to determine the overall level of polarization within the acini. To do this we carried out TEM imaging of more than 10 acini as a way to ensure that the features we observed were a consistent phenomenon of these acini and not isolated to a very small percentage

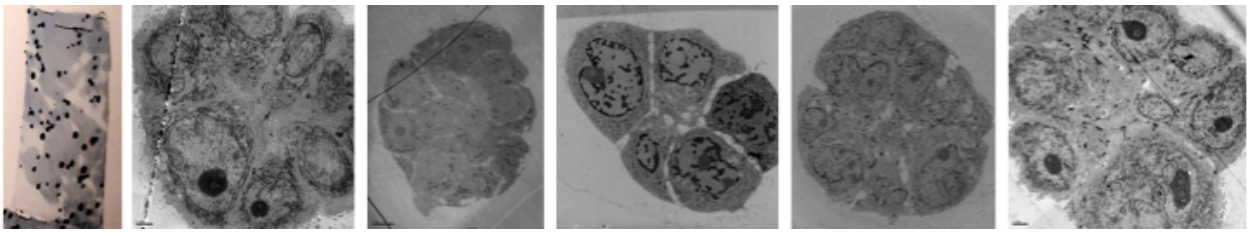

Figure 4. Overview of S1 acini imaged by TEM. At the furthest left is a light microscopy image of the toluidine blue stained 500nm section of resin embedded acini. This cross-section through the matrigel embedded field of acini displays the wide range of sizes of the acini. The other images are low magnification TEM of complete acini, highlighting the variety of cell arrangements and cell density observed. No central lumen are present and cells have electron lucid intercellular spaces filled with membrane protrusions.

of the structures. We looked for markers of polarity in the cellular features, such as visible tight junctions, lumen, basement membrane, apical microvilli, and hemidesmosomes. At what should be the apical surface of the epithelial cells, we often observed a lack of tight junctions; however, the junctions seen were intermittent and short. Furthermore, when a tight junction joined two cells, it was not at the boundary of a luminal opening, although there were often microvilli-like structures flanking the junction on both sides. We observed no lumens, though we did see plentiful intercellular spaces between cells, which were filled with the microvilli-like protrusions. The intercellular spaces were largely formed between desmosomes, which were propagated across all interior surfaces of the cell, with the exception of the basal surface. At the basal surface, we observed hemidesmosomes that connected the epithelial cells to the intermittent basement membrane. When present, the basement membrane appeared robust and normal as previously described. Additionally, we did observe that mostly the organelles, specifically the Golgi, were positioned toward the "top" of the epithelial cells. Also of note were the strongly stained tonofilaments observed throughout the cytoplasm, which are most likely to be a variety of keratins. S1 cells are typically identified as luminal epithelial cells by immunofluorescence labeling for the expression of keratins 8 or 18 (Briand et al., 1987; Weaver et al., 1995).

Discussion

The striking mixture of organization and disorder was quite unexpected as light microscopy based experiments over the past few decades have made a clear case for the S1 acini's strict/faithful/ organization and polarization (Lo et al., 2012; Rizki et al., 2008; Wang et al., 1998; Weaver et al., 1996). These studies typically rely upon biochemical analyses and fluorescence microscopy for their conclusions (Figure 2). To date only a few publications have imaged HMT-3522 S1 cells by TEM and none have explored the detailed ultrastructure of these cells in 3D cell culture (Briand et al., 1987; Weaver et al., 1997). To our surprise, we have discovered that S1 acini demonstrate a state of semi polarized tissue. A recent TEM ultrastructural analysis of another cell culture grown human mammary epithelial cell line,

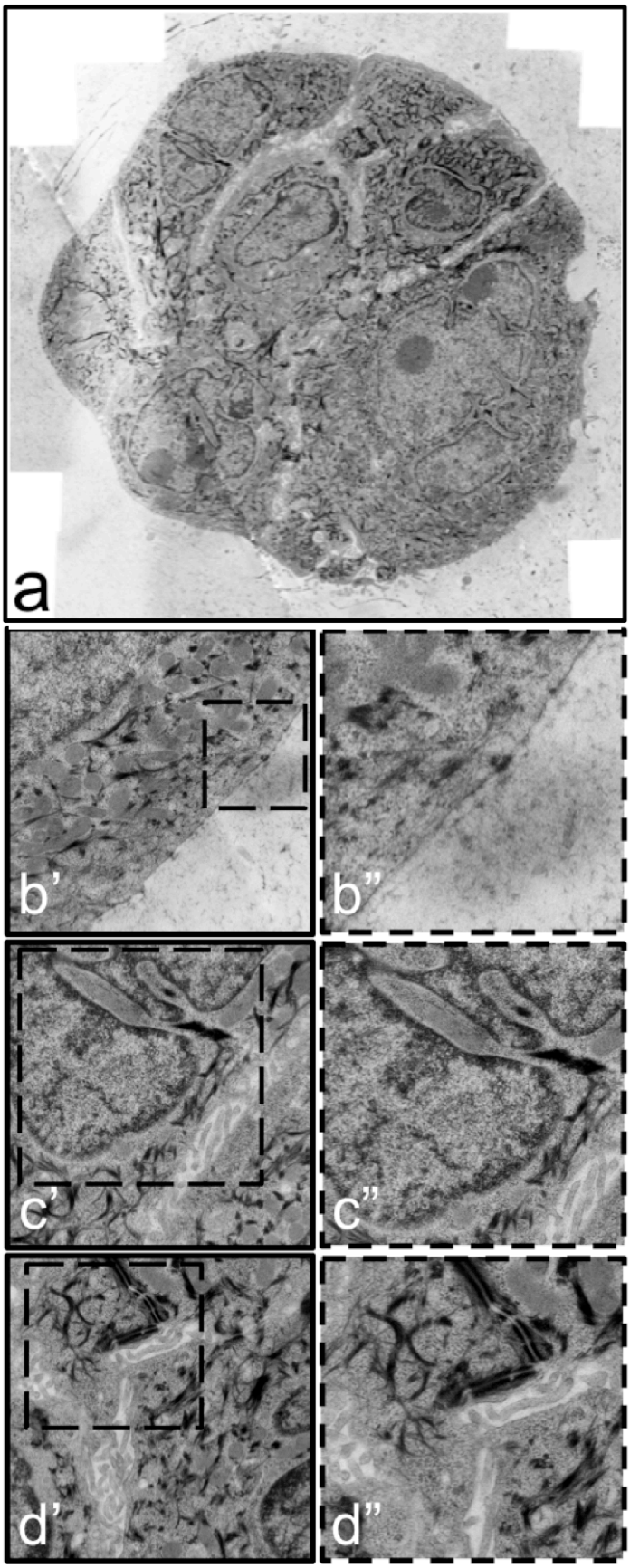

Figure 5. Mixed state of epithelial cell polarization within S1 acini. (**a**) Montaged TEM overview of S1 acinus cross section showing 8 cells present. No lumen is observed and all junctional complexes detected are desmosomes. (**b, b'**) Basal surface of acinus cells have intermittently organized basement membrane stabilized by hemidesmosomes complexes. (**c, c'**) S1 cells have complex nuclear invaginations present, indicating the cells are not fully polarized. (**d, d'**) Further implicating the cells a not fully polarized are the extensive membrane protrusions within the intercellular spaces of nearly all the interior cell surfaces. These membrane protrusions are observed to be of variable lengths and appear on every surface except the basal surface in contact with ECM. The protrusions are always found intermixed with desmosome junctions.

MCF-10a, demonstrates a similar phenomena of disorder at the apical surface (Underwood et al., 2006). While MCF-10a acini contained lumen and an organized basement membrane, further inspection of the TEM data demonstrate that these acini may also be more disorganized than first thought.

Artifacts caused by chemical fixation, dehydration and infiltration are known to cause distortions of tissues, at both micro- and macro- scales (Hayat, 2000). We propose a follow up study to address the issue of whether the methods used here for sample preparation could be improved, thus providing the best possible and most native preservation of the S1 acini structures. We would specifically aim to ensure that cellular features such as nuclear invaginations

and intercellular membrane protrusions are not the result of sample processing, whether by chemical or cryo-preservation methods. To perform such a study, it would be advisable to utilize a tissue with well-characterized ultrastructure for evaluation of differing sample preparation methods, therefore providing an improved confidence in the unexpected features of the HMT-3522 S1 acini.

Further, the current study lays clear a main limitation for TEM analyses, namely the quite limited volume of a cell or tissue that can be evaluated in a timely manner. Proper size and distribution evaluation of features described herein, such as the membrane protrusions and filament networks, requires large scale, high-resolution and volume-centric approaches. Until recently, serial-section EM and EM-tomography were the only two choices for these high volume approaches; however, over the past few years serial block face and focused ion beam EM have become more widely used and offer an ideal strategy to further analyze the important ultrastructural features of the S1 acinus (Mikula et al., 2012; Schroeder-Reiter et al., 2009).

The consistency of the disorganization across nearly a dozen S1 acini causes us to search for physiological relevance for the state of these cells and to rule out the possibility of sample preparation artifacts. The intercellular spaces filled with membrane protrusions are particularly reminiscent of what has been described in the developing mammary gland (Hogg et al., 1983). Recently, an *ex vivo* system for studying the developing mammary gland and branching morphogenesis has been developed (Ewald et al., 2008; Lee et al., 2007). Use of this *ex vivo* system would provide a physiologically accurate background in which to study whether the membrane protrusions are “normal”, while also allowing for perturbations of the system to investigate the nature of the protrusions. For validating the sample preparation technique, in particular high pressure freezing, a well characterized complex model system would be ideal.

Chapter 3.
Comparative Sample Preparation Strategies for Optimal Tissue Preservation for Transmission Electron Microscopy

Introduction

Methodologies for ultrastructural analysis in complex tissues

Data obtained using TEM to analyze the HMT-3522 S1 cell line raised small concerns regarding any potential artifacts generated by sample processing methods. To properly dispel apprehensions, we sought a well-documented model system with a range of complex tissues to evaluate the HPF-FS methodology. A careful evaluation of the HPF-FS technique and comparison to other standard TEM sample preparation methods would provide insight into the strengths and weaknesses of each approach. The goal is to address whether HPF-FS technique could be introducing artifacts into the S1 cells, which could lead to unsuitable interpretations. Specifically, we sought to address concerns over sample shrinkage, disruption of large macromolecular complexes and degradation of fine cellular architecture.

The zebrafish (*Danio rerio*) has been recognized as a powerful model organism for the study of vertebrate physiology and human disease (Amatruda et al., 2002; Avanesov and Malicki, 2010; Dooley, 2000; Lieschke and Currie, 2007). While the advantages for use with optical microscopy long have been appreciated, the zebrafish promises to be a near-perfect model organism for electron microscopy, given the slim body plan during the larvae stage and the relatively small size of fully functional organs. This system displays the essential and fundamental mechanisms of tissue and organ function of higher vertebrate physiology. Certainly, from the small size of the animal one may reason that most vital organs can be studied in the context of an intact animal without the need of prior dissection, which may result in trauma and therefore damage to the dissected tissue. The analysis of differential preparation methodologies will pave a path for nearly any kind of tissue sample.

Meaningful transmission electron microscopic (TEM) imaging crucially depends on the faithful preservation of the cellular and tissue ultrastructure. Traditional approaches that are based on room temperature chemical fixation, metal staining, dehydration with an organic solvent, followed by resin-embedding and polymerization often result in poor preservation. These artifacts manifest as large gaps between cells as well as clear signs of aggregation and extraction of the cytoplasmic content, thus substantially altering cell and tissue organization (Hayat, 2000; Wang et al., 2005). Over the last two decades, steady improvements in sample preparation protocols, such as the progressively lowering temperature dehydration, microwave-assisted protocols, as well as the increased availability of ultra-rapid freezing and low-temperature dehydration (freeze-substitution), have led to an increased interest in the ultrastructural imaging of prokaryotic and eukaryotic cells and dissected tissues (McDonald and Auer, 2006).

In this study, three widely-used sample preparation protocols are systematically compared: progressively lowering temperature dehydration (PLT), microwave-assisted processing (MW), and high-pressure freezing followed by freeze substitution (HPF-FS). We demonstrate how well these different protocols preserve the tissue organization in various organs, as well as their respective cellular and subcellular macromolecular complexes

organization. In addition to overall evaluation of the tissue integrity, we have specifically conducted an in depth examination of the zebrafish ear and eye, where we found that HPF-FS provides the best, close-to-native state of preservation. While HPF-FS not too surprisingly delivered best preservation in all tissues studied, MW and PLT processing can deliver nearly equal preservation in some specific tissues. Electron tomography provided a 3D stack of data for molecular resolution analysis of skeletal muscle, possible only with samples prepared by HPF-FS.

Conventional processing

Conventional fixation strategies rely solely on diffusion of the solutes into a specimen during immersion in primary (glutaraldehyde, formaldehyde, etc) and secondary (osmium tetroxide, uranyl acetate) fixation and organic solvent dehydration followed by resin infiltration all at ambient temperatures or "bench top". The efficacy of this strategy is limited significantly by the damaging effects of the chemicals at each step of processing whose effects are exacerbated by the ambient temperature and long exposures required for proper diffusion of the solutes. Effectively, the resulting samples can have severe alterations in the organization of the cellular ultrastructure, complete types of macromolecular complexes or even organelles can be missing or damaged. Other regular artifacts of conventional processing can include bloated organelles, membrane blebbing, empty or cleared cytoplasms, aggregation of filamentous proteins and DNA. Some of these effects can be caused by fixation with chemical, particularly during the first fixation, others can be due to osmolarity differences in the cell and the fixation buffers, however most of the damage is done during the slow ambient temperature dehydration process. During dehydration samples are immersed in an ascending gradient of ethanol up to 100% where upon the sample is transitioned to acetone for resin infiltration; the process can take hours. These damaged samples can lead to misconceptions of the underlying architecture of cells and unfortunately, it is only recently that biologists have begun to appreciate the value of transmission electron microscopy studies again. Convergently, there have been vast technological advances in the field of TEM sample preparation to address and resolve these long-standing issues, some of which will be explored herein.

High pressure freezing and freeze substitution

Considered the gold standard of sample processing techniques for any high-resolution ultrastructural or morphological characterization, high-pressure freezing has been a consistently changing field since its inception in 1968 by Hans Moor. The subsequent development of freeze substitution has solidified high-pressure freezing as the standard by providing a stable transition between the frozen and ambient state of samples during processing. Using a high pressure freezer live cells can be fixed without chemicals through cryo-immobilization. HPF accomplishes excellent sample preservation by freezing with up to 2000 bar pressure (roughly 30,000 psi) (Moor, 1987). Further, this pressure reduces the freezing point of water by about 20°C impeding the nucleation and formation of ice crystals. By diminishing the chances of ice crystal formation freezing samples across a wide range of thicknesses can be frozen in liquid nitrogen. Though herein lies the limitation of HPF-FS, the sample size, while substantially larger than in plunge freezing or slam freezing, is still limited to a maximum of 600 μm by 1.25 mm (McDonald and Auer, 2006). This is the both the limit of maintaining good sample preservation, and therefore freezing, as well as the size of the freezing chamber within the HFP machine. Another limitation to the HPF-FS approach is the requirement for the special equipment, whereas

conventional sample preparation can be performed within any laboratory setting. However, the usefulness and robust sample preparation capabilities of the HPF system has spurred much interest and many institutions now have this tool within their EM suites.

Samples frozen using HPF and then processed by FS are considered to be as near to the native state as can be for anything being processed for imaging by electron microscopy. Data obtained by HPF-FS processed tissues are now the benchmark for understanding delicate and precise organization of cellular machinery. Artifacts are however possible with this technique and are linked to the state of the tissue prior to the freezing process. Specifically, the water content of the sample can influence the creation ice crystals, necessitating the use of cryoprotectants, which are typically protein rich aqueous mixtures that can fill in space between the sample and the specimen holder (McDonald et al., 2010). These cryoprotectants, such as bovine serum albumin and yeast paste, provide a substrate for heat conduction and reduce the available water content within the specimen holder, thereby protecting the sample from possible freeze damage. Freeze damage is the most common type of artifact of HPF processing, occurring when ice crystals are permitted to grow from a site of nucleation; in the final result it will appear as massive protein or nucleic acid aggregation.

Following HPF the specimen must remain frozen in liquid nitrogen until the freeze substitution process can be performed. Freeze substitution provides an advantage over conventional dehydration since the samples are cryo-immobilized at -50°C during the exchange of water into organic solvent. Furthermore, freeze substitution combines the metal staining of a secondary fixation with the dehydration process into one step. During freeze substitution the samples are slowly raised to 0°C over the course of hours or even days within a processing machine with precise temperature control. As the temperature rises, the acetone-heavy-metal-stain medium melts before the water based sample, allowing for a slow exchange of melting water molecules with acetone. The stability of the tissue is preserved during this exchange, minimizing extraction of molecular features of the cells (McDonald, 1999). Very recently, work by McDonald and Webb demonstrated this process can be condensed down to a simple and inexpensive protocol requiring only 3 hours (McDonald and Webb, 2011). The distinct advantage of HPF-FS is the superior preservation of fine cellular features.

Microwave assisted processing

Microwave processors have been demonstrated to speed fixation times and improve specimen morphology (Leong et al., 1985; Ruijter et al., 1997; Webster, 2007; Wendt et al., 2004). Generally, the microwave allows all sample processing steps to be shortened drastically and yet ultrastructural and immunogenicity of the sample are maintained at a higher level than compared to conventional bench-top approaches. Microwave processors can be utilized to rapidly fix tissue with aldehydes or osmium, perform accelerated alcohol dehydration, and to quickly infiltrate and polymerize specimens with resin. Often microwave processors are used for pieces of the processing work flow, such as primary and secondary fixation, and combined with other techniques.

Modern microwave processors have been utilized to produce consistent and reliable sample preservation through the use of water reservoirs and by allowing precise control over the radiation generated from the magnetron. In some processors, a large flat glass topped pad sits at the bottom of the microwave chamber, upon which samples will sit in contact with the glass. Within the glass topped pad is flowing temperature controlled water that will absorb the microwave radiation directly after it has passed through the sample, preventing further

propagating within the chamber. Additionally, the energy output of the magnetron is precisely controlled in laboratory microwave processors. While in conventional microwave ovens the goal is to cook food through irradiative dielectric heating, only a substantially small energy output is necessary for the subtle changes being affected in tissue samples for electron microscopy processing. The typical energy used to assist during fixation steps is 150 watts while up to 750 watts can be used during polymerization steps. This control of energy output is important in fine tuning protocols for specific samples and to prevent samples from being heated during processing (Giberson and Demaree, 1995). The exact mechanism for how microwave radiation enhances the speed of fixation and other processes has yet to be determined. The advantage of microwave assisted processing is its speed: short exposure times to damaging chemicals.

Progressively lowering temperature

Chemical processing of samples at room temperature can exacerbate artifacts from the preparation process. One way to minimize these effects is to dehydrate cells in progressively lowering temperatures (PLT), thereby stabilizing macromolecular complexes as the water is replaced with organic solvents. Some common artifacts that can occur by processing in ambient temperature include dissolution of lipids and denaturation of proteins, both of which cause extraction of features. Therefore, PLT is considered the next best method for low temperature processing behind freeze substitution (Schwarz and Humbel, 2007). During PLT, samples undergo chemical fixation steps on ice, or at 4°C, followed then by an ascending gradient of ethanol coupled with a descending gradient of temperature until samples are held in 100% ethanol on dry ice, -35°C. The advantage of PLT is the cold temperatures during dehydration: allows for cellular features to remain stabilized during the chemical exchange of water for solvent.

Experimental Procedures

Zebrafish stock and growth

Dr. Sharon Amacher, University of California, Berkeley generously provided zebrafish embryos at both 72 and 120 hours past fertilization, grown as previously described (Westerfield, 2000).

High pressure freezing and freeze substitution processing

Zebrafish larvae were anesthetized with 0.04% tricaine (Ethyl 3-aminobenzoate methanesulfonate) prior to being placed 20% glycerol, a cryo-protectant. Due to the length of the zebrafish, it was necessary to cut the fish in half just beneath the yolk sac to make a head containing portion and tail containing portion of the fish. Once the zebrafish had been cut, they fit into the 1 mm wide by 200 μm deep aluminum freezing hats, then surrounded with more cryoprotectant prior to freezing. The zebrafish were then cryo-immobilized using a BAL-TEC HPM-010 high-pressure freezer (BAL-TEC, Inc., Carlsbad, CA), as described in Chapter 2.

Microwave-assisted processing

All microwave steps were performed using a Pelco 3450 laboratory microwave oven with a Pelco Cold Spot insert cooled by a Pelco 3420 Load Cooler (Ted Pella, Redding, Ca). The

whole and cut zebrafish larvae were anesthetized with tricaine (0.04%) prior to primary fixation in 4% glutaraldehyde, microwaved for 1 min-on, 1 min-off, 1 min-on at 150 watts (Power Level 1). The zebrafish were washed with 0.1M phosphate buffer and microwaved 40 sec (PL1) a total of 3 times in fresh phosphate buffer. For secondary fixation, the samples were treated with 1% osmium tetroxide (in 0.1 M phosphate buffer), microwaved for 1 min-on, 1 min-off, 1 min-on at PL1 and then left on bench at room temperature for up to 1 hour. The samples were then rinsed thoroughly with 0.1M phosphate buffer, microwaved 40 sec (PL1) a total of 3 times in fresh phosphate buffer and then rinsed with distilled water by microwaving 40 sec (PL1) once, to remove the buffer. The *en bloc* staining of the samples was done by microwaving 1 min-on, 1 min-off, 1 min-on (PL1) in 2% uranyl acetate (in distilled water). Dehydration was done through progressively increasing series of ethanol concentrations (30%, 50%, 70%, 95%, 100%) for which the samples were microwaved 2 times for 40 sec (PL1). Infiltration began with two 100% acetone washes for 40 sec (PL1) followed by Epon-Araldite resin infiltration (McDonald & Muller-Reichert, 2002). The zebrafish were flat-embedded and polymerized in Epon-Araldite resin as described above.

Progressively lowering temperature processing

Zebrafish larvae were chemically fixed in 4% glutaraldehyde overnight at 4°C. The zebrafish larvae were then washed in cold 0.1M phosphate buffer 2 times for 10 minutes on a rocker at room temperature. The secondary fix was in 1% osmium tetroxide for 30 minutes on ice. The zebrafish were rinsed with 0.1M phosphate buffer 3 times for 10 minutes on ice and then rinsed in distilled water for 10 minutes. *En bloc* staining was done with 2% uranyl acetate for 20 minutes on ice. For ethanol dehydration with progressively lowering temperature the samples were exposed to 30% ethanol at 4°C, to 50% ethanol at –20°C, and to 70%, 95%, and 100% ethanol at –35°C, for 20 minutes per incubation period. The zebrafish were restored to room temperature in 100% ethanol before infiltration in an Epon-Araldite mixture and flat-embedding as described above.

Transmission electron microscopy

70 to 100 nm thin and 500 nm thick sections were sectioned and imaged as described in Chapter 2.

Results

Tractability of tissues in whole zebrafish using HPF-FS

A benefit to using the HPF-FS is the relatively light staining *en bloc* of biological tissue as compared to the typical opaqueness resulting from bench top conventional methods (Figure 6). The zebrafish, when exposed to osmium tetroxide in conventional fixation steps, microwave assisted or PLT, quickly (< 5 minutes) became darkly stained to point that all organs and regions of interest were obscured from view (Figure 6A). The heavy stain was likely due to the epidermis of the fish taking up the osmium stain first and does not necessarily reflect the overall amount of stain transmitted throughout the entire fish. However, with HPF-FS processing the zebrafish maintained a translucency that allowed for the tracking of regions of interest during

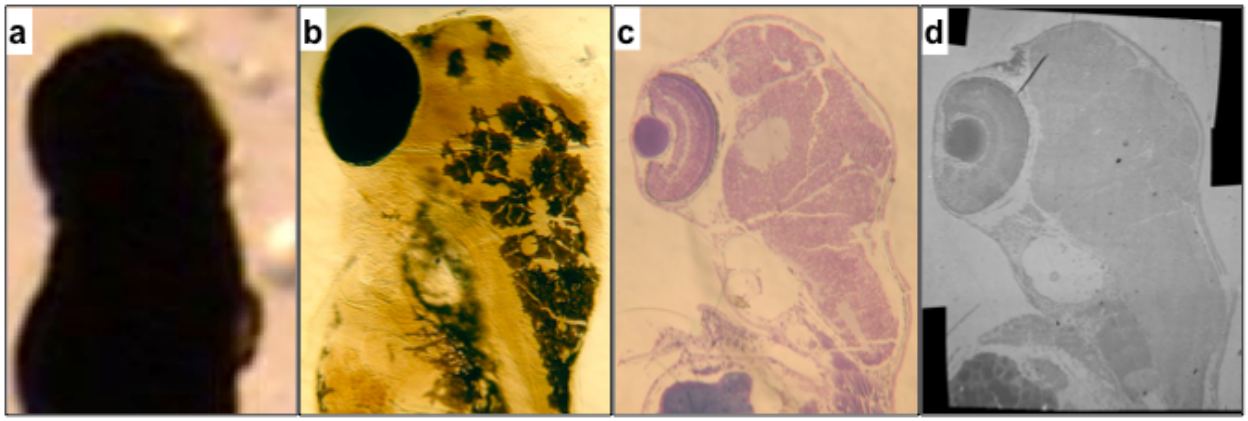

Figure 6: Tractability of specific organs and tissues of interest during sample preparation. (a) The outcome from using either microwave-assistance or progressively lowering temperature is an opaque black specimen; it impossible to discern even the most prominent feature, the eyes. By contrast, in a sample prepared by HPF-FS, exquisite detail is observed by light microscopy in the resin block (b) and a toluidine blue stained 250 nm thick section (c), which is then complimented by the TEM wide field imaging of the 70 nm thin section (d). By combining the HPF-FS with the thin embedding method, organs and various tissues of the zebrafish become quite visible allowing for enhanced orientation and tractability during sectioning and imaging.

sectioning (Figure 6b). Figure 6 displays the tractability of these regions of interest from embedment in resin, to the toluidine blue stained 250 nm thick sections, and into the 70 nm thin-section viewed by TEM. For the purposes of this study, we focused our attention on the eye, ear, and indicators of overall preservation including skeletal muscle tissue, all of which were easily identified en bloc using HPF-FS with thin resin embedding. Within one section, several areas of interest could be present, thus we applied wide-field TEM imaging using the montaging feature of Serial EM to map the entire section, allowing for efficient tracking of data collection sites (Figure 6c-d).

Markers of ultrastructure indicate overall tissue preservation

To assess the efficacy of the three processing methods, we evaluated features of tissue that can typically indicate the general state of cellular preservation for the sample. These standards of preservation are usually highly organized macromolecular structures or tissue that can easily indicate artifacts or damage from sample processing, through disruption of their organization. The ultrastructure and organization of the skeletal muscle tissue is often indicative of overall tissue preservation. The appearance of the regular spacing of the thin and thick filaments of the sarcomere, the striation patterns, and mitochondrial preservation in longitudinal sections was used to determine the level of sample preservation for each processing methodology. Mitochondria were not noticeably better preserved in any of the preparations. Differences between the three preparation methods in the skeletal tissue were somewhat subtle, with the most distinct difference being the Z-disc and I-band regions of the sarcomere more densely stained in the HPF-FS sample than in the other preparations. All skeletal muscle images were take from the tail region of the zebrafish.

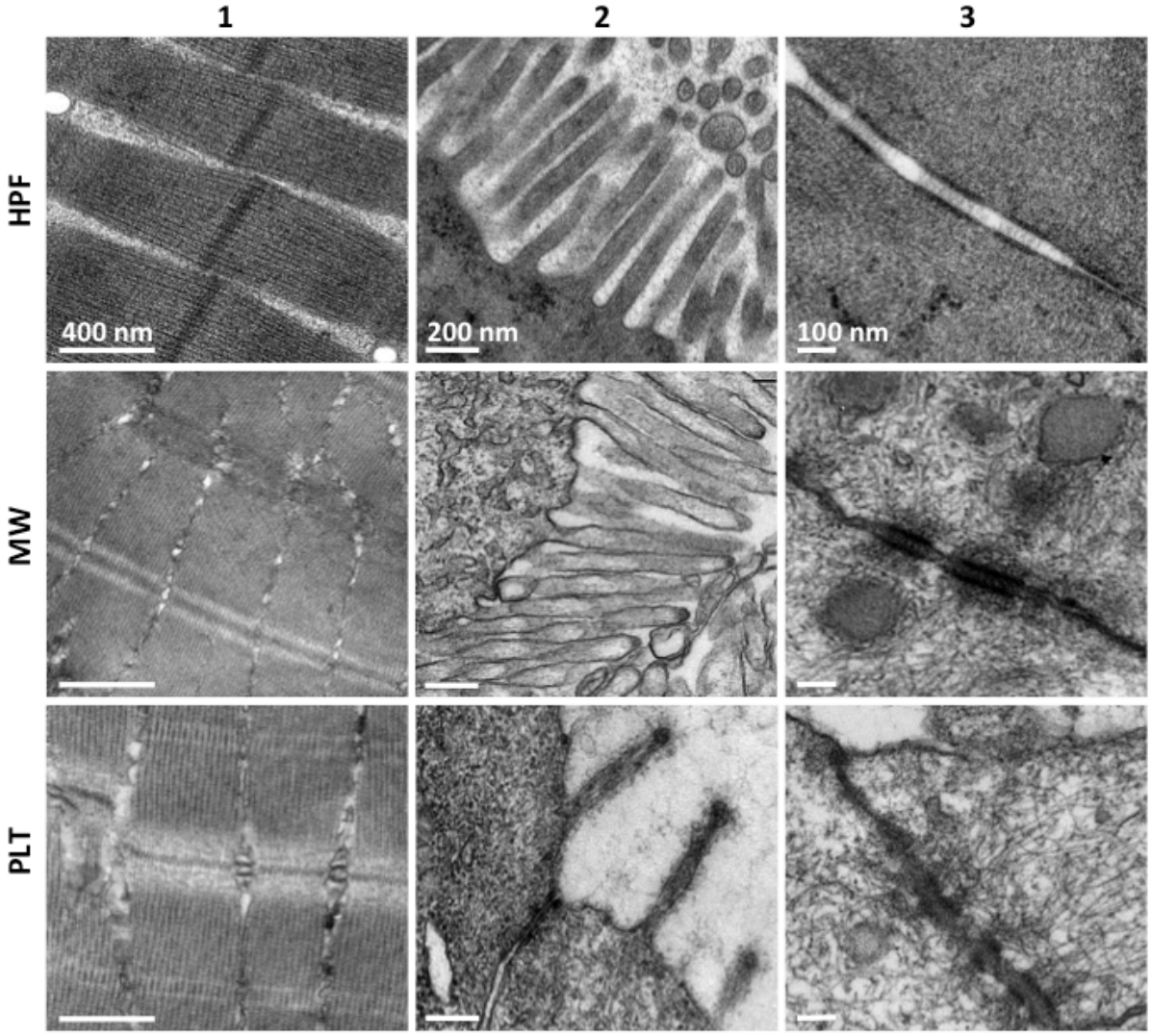

Figure 7: Comparison of preparation methods in preservation of cellular and ultra-structural features. HPF (FS), MW, and PLT processing are compared to analyze the preservation of markers of ultrastructure: skeletal muscle (1), gut microvilli (2) and desmosomes (3). The skeletal muscle (1) displays little difference; the gut microvilli (2) is best preserved with HPF-FS, as demonstrated by smooth membranes straight microvilli; the desmosomes (3) of HPF-FS are well preserved with the intercellular cadherin filaments visible.

The gut microvilli ultrastructure (Figure 7) varied between sample preparations and was judged by the appearance of parallel actin filaments, overall packing of microvilli and the straightness of the membranes of the microvilli. HPF-FS produced defined and robust appearing gut microvilli forming a brush border, which had visibly retained actin filaments within the microvillar protrusions. The microvilli of the HPF-FS samples were surrounded by well-defined and straight plasma membranes. Conversely, the microvilli in the PLT and MW sample preparations appear shrunken, having intermittent contrast, indicating that the actin filaments have likely suffered extraction during the dehydration processes. Further, the membranes of the

PLT microvilli are not well defined and are fewer in number, while the plasma membranes of the MW gut epithelia sample appear wavy. MW samples also lack consistent actin filaments; however, there are a similar number of microvilli present as compared to the HPF-FS samples.

The preservation of desmosomes in epidermis cells gave similar results as the gut microvilli. The HPF-FS sample had very well organized structures, in which desmoplakin proteins are aligned in parallel on opposite cells and the filamentous cadherin protein links spanning the intercellular space between the plaques are well separated and perpendicular to the membrane. Also of significance was the high density of cytoplasm in the two desmosome-linked cells, which is quite striking compared to the other preparation methods that produced a less dense, lighter cytoplasmic background indicating a lack of stained material. In the PLT sample, the darkly stained desmosomes are readily visible against the extracted cytoplasm. The desmosomes are not quite straight as they curve with the membranes of the cells. The cadherin and desmoplakin proteins of the desmosome are heavily stained, causing them to appear blurred out and hindering the discernibility of their organizational pattern. Due to the artifact of extraction of material from the cytoplasm during sample processing, the intermediate filaments of the MW and PLT samples are very easily observed connecting to the desmosomes. The MW samples had the most dense staining of desmosomes, which obscured the organized pattern of the structure. However, the cytoplasm of the cells in these samples seemed to be an intermediate density between the extracted space of the PLT samples and the full density observed in the HPF-FS samples.

Preservation of mechanosensitive hair cells of the inner ear

Mechanosensitive inner ear hair cells were examined because of their sensitivity to osmotic changes and chemical fixation (Triffo et al., 2008). There was a marked difference in the preservation of the inner ear maculae across the three methods. Excellent preservation of the delicate outer hair cells was observed using HPF-FS while the MW and PLT approaches resulted in intermediate to bad preservation. The outer hair cells were well preserved with HPF-FS from a wide field view of the entire row of the outer hair cells to the nanometer resolution of parallel actin filaments within the specialized stereocilia bundles at their apical surface (Figure 8). Plasma membranes are smooth and continuous for each cell observed within the maculae, hair cells and supporting cells. With HPF-FS the densely packed cytoplasmic content is precisely positioned and the apical stereocilia are straight and well defined. In high magnification views, the fine structure of the parallel actin filaments of the stereocilia are observed and importantly, the tip link filament protein is readily viewed as well (Figure 8). The membranes of the stereocilia are straight in the HPF-FS samples.

The MW method produced the most unsatisfactory tissue preservation, of the three methods, with the majority of cells ending up collapsed and disfigured (Figure 8). The inner ear hair cells of the macular were no longer the expected columnar shape; instead, the margins of the cells were obscured. The cellular components were also distorted and sometimes unrecognizable, with large vesicles lacking electron density spanning microns occurring where cells should be. There were considerably fewer stereocilia present in these samples as well and when observed, the stereocilia had irregular wavy membranes. Few defined tip link filament proteins were observed between stereocilia in the MW samples.

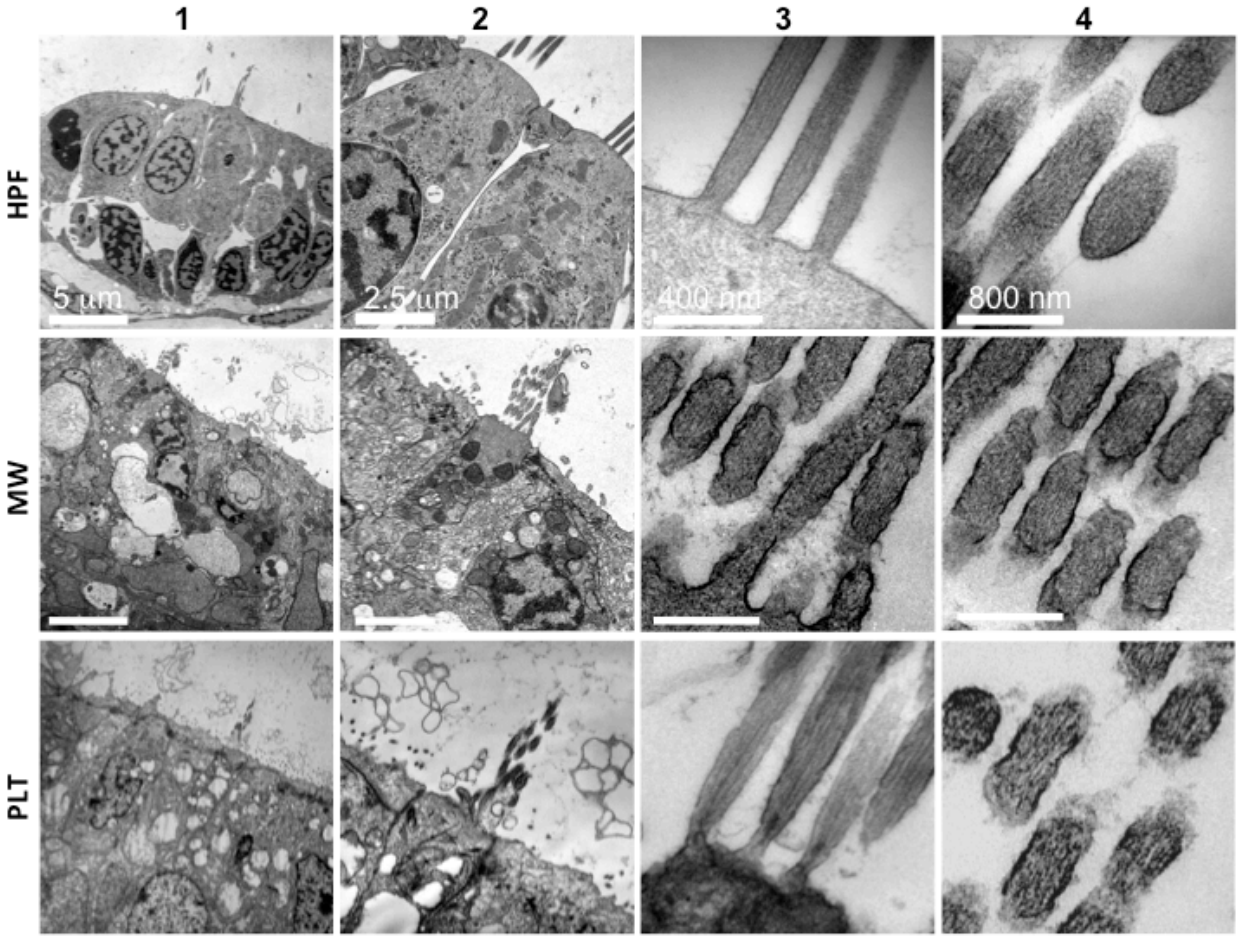

Figure 8: Mechanosensitive outer hair cell preservation of the inner ear. The fixation sensitive sensory cells of the zebrafish inner ear were examined for preservation. (top row) With HPF-FS, cells of the macula (1) remain intact and without any large distortions, the outer hair cells (2) and apical stereocilia (3-4) are well preserved. The MW samples (middle row) display large disruptions in overall cell shape in both the sensory and supporting cells (1); however, the stereocilia are still present and parallel actin can be observed (3-4). In the PLT samples (bottom row), the outer hair cells (1-2) retain the columnar shape but sample artifacts in the form of large vesicular bodies distort the cell cytoplasms; the stereocilia are maintained and parallel actin can be observed (3-4).

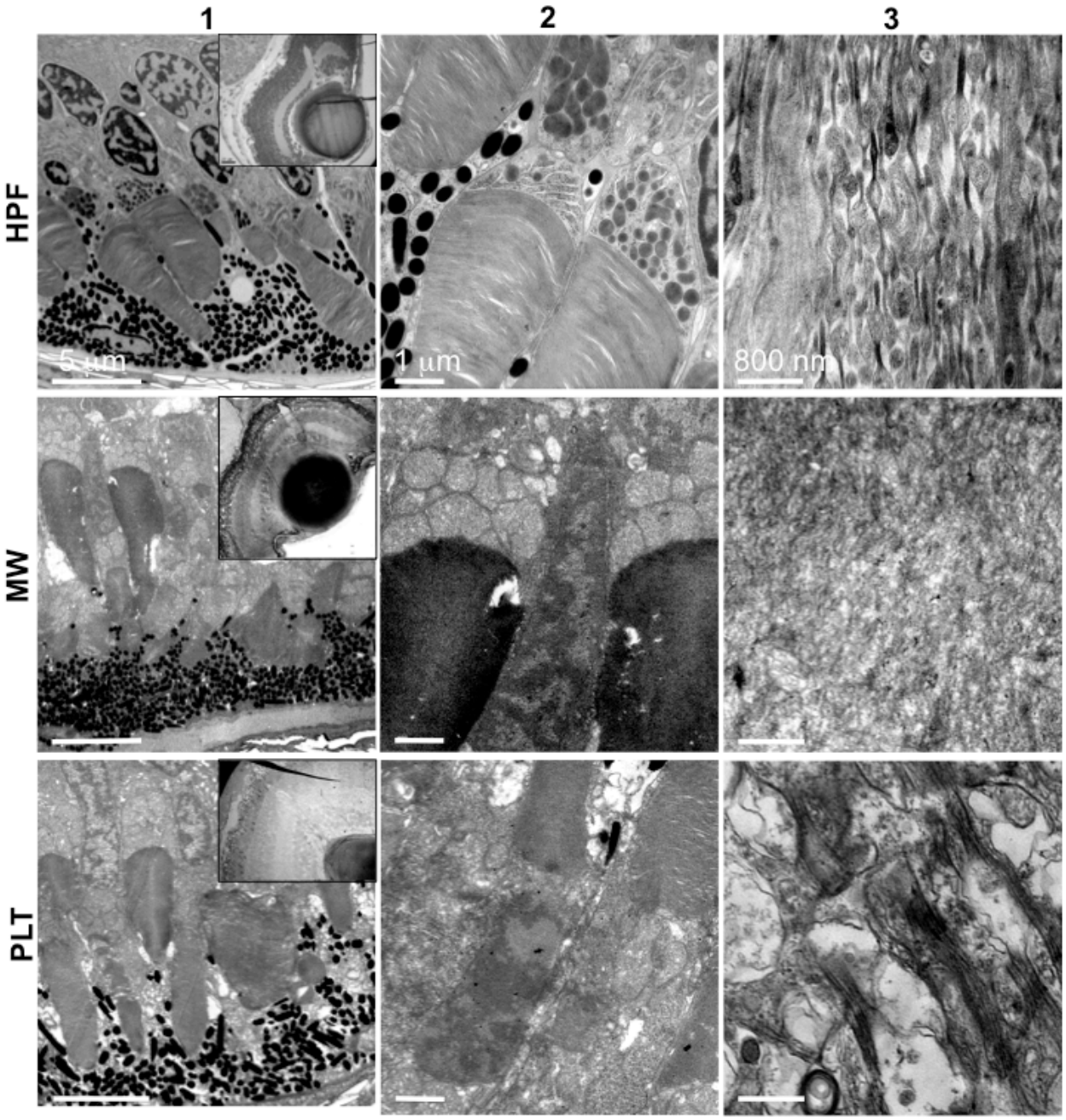

F**igure 9: Preservation of the retina and optic nerve.** In column 1, the layers of the retina are observed. At low magnification views, the level of preservation of fine structure in the retina is difficult to assess (insets of 1) for the 3 methods. Higher magnification of the photoreceptor layer and pigmented epithelium reveals distortions of the cellular ultrastructure (1), particularly within the MW and PLT samples. These artifacts of MW and PLT are observed in the photoreceptors (2), in which the organelles of cytoplasms indistinguishable; the HPF-FS is by far the best preserved. The delicate neurons of the optic nerve were also best preserved by HPF-FS (3); in the PLT sample, axons are aggregated and cell bodies are bloated, while the MW sample failed to have any preserved neurons (3).

The PLT samples maintained a recognizable cell structure of columnar shape but suffered major deformities to cell components. The endocytic vesicles are enlarged and more numerous than expected. Mitochondria, endoplasmic reticulum and cell junctions are either absent or unrecognizable. Of note is that the nuclei are reasonably intact although the chromatin content and distribution looks lighter and more scattered than expected. The stereocilia are regular in appearance, and their membranes are only slightly wavy. The actin filaments within the stereocilia appear to be straight, though in transverse sections aggregation is apparent.

Preservation of the eye and optic nerve

In each of the three sample preparations, the dorsal and ventral marginal zones are easily located and observed. The optic nerve, inner and outer nuclear zone, inner and outer plexiform layer, ganglion cell layer and retinal pigment epithelium are all easily tractable and characterized with all methods using thick and thin sections. These features are observed in the insets of the overview panel of Figure 9 and aid rapid judgment of depth and orientation for sectioning efforts. Orientation of the eye is more obvious with HPF-FS due to the transparent nature of the staining thus allowing for precise macroscopic orientation of the tissue (i.e. it is visible by light microscopy without the need for sectioning), with even the tapetum lucidum still observed; the tapetum lucidum is a reflective layer behind the retina useful for vision in low light settings. The size restrictions (600 micron depth limit) of the specimen holders used for HPF usually required the breaking or lysing of one eye to fit the fish trunk and head within the specimen holder. This can sometimes be avoided with 72 hour post fertilization embryos or younger; however, beyond the 72 hour range the size of the head is often too large to fit well within the specimen holders used for freezing. Embryo size is not an issue encountered with the other preparation methods; however, the preservation of the eye tissue with MW and PLT methods left much to be desired.

While the outer segments of the photoreceptors in each of the three methods survived processing to remain well-stacked membranes, the same result is not found when analyzing the inner segments (Figure 9). The inner segments of these specialized cells are best preserved by HPF-FS, in which the nuclear architecture and chromatin distribution are maintained as well as mitochondria, golgi, endoplasmic reticulum, and other cellular compartments. While the nuclei remain in place, the plasma membranes of each cell have become obscured in the MW and PLT samples. The notable cellular organelles are difficult to identify in both the MW and PLT inner segments of the photoreceptors.

Particularly of note is the poor preservation observed the optic nerve and in the inner segments of the photoreceptor cells of the PLT and MW processed embryos (Figure 9). While in the HPF-FS samples the cell bodies and axons of individual ganglion cells can be easily identified within the optic nerve, these cells in the PLT and MW samples are at best shadows of what is expected (Figure 9). In the PLT samples, the ganglion cell bodies appear as evacuated spaces surrounded by aggregated axons and plasma membrane debris. The optic nerve in MW prepared samples is a homogenized slurry of ganglia.

Discussion

Herein we evaluated commonly used sample preparation approaches for transmission electron microscopy imaging across a variety of tissues. The end goal was to determine which of these methods provides the most robust and useful sample preservation and also to identify the potential drawbacks for each approach. We decided on high-pressure freezing with freeze

substitution, progressively lowering temperature and microwave assisted processing as these are three techniques commonly used but which have not yet been directly and methodologically compared. Furthermore, each of these methods has previously been demonstrated to provide better sample preservation than conventional bench top processing (Hayat, 2000; Schwarz and Humbel, 2007; Sosinsky et al., 2008; Stradalova et al., 2008; Wendt et al., 2004). Utilizing a complete and complex vertebrate like the zebrafish we aimed to generate a roadmap across a range of tissue types matched with the best processing method for electron microscopy imaging. Sample processing for electron microscopy can be labor intensive and consume hours or days of work; therefore knowing the best possible method for a desired result within a particular tissue is of value, thereby reducing the requirement for multiple troubleshooting processing attempts.

From fine molecular structures through macroscopic features we have found HPF-FS to provide the highest level of preservation, as judged by specific markers of preservation such as membrane smoothness, cellular density, level of protein aggregation, etc. While confirming that HPF-FS, the gold standard, was indeed the best tool for preserving a wide range of tissue was no surprise, we did encounter a number of caveats worth discussing. The first of which being that freeze damage within the tissue occurs with some regularity and can be found dispersed throughout a wide area. For example, some regions of the zebrafish were more prone to freeze damage due to ice crystal formation, such as the yolk sac and brain tissue, however damage was also observed to a small extent elsewhere. Interestingly, freeze damage artifacts often appeared directly adjacent to areas displaying extremely good preservation. In practical terms, these results mean that inclusion of more samples will increase the chance of having the structure of interest well preserved by HPF-FS (i.e. if images of the heart is desired from one sample, prepare at least 3 by HPF-FS to ensure one of the samples has excellent preservation). Others have previously highlighted and thoroughly discussed proper HPF-FS technique and it is worth noting that augmenting sample size should be coupled with good HPF technique to produce optimal results (McDonald, 2007; McDonald et al., 2010). In our hands, nearly every zebrafish displayed some degree of freeze damage however the extent of the damage ranged widely between specimens and mostly the areas of freeze damage were localized to a few microns in volume. Size restriction for HPF is another issue; samples must be within the size of the specimen holders used for freezing. For zebrafish, we circumvented this by collapsing one of the eyes and/or manually bisecting the body with a thin razor. Other types of samples may encounter this size restriction and need to be undergo more extensive dissection or preparation prior to HPF, for these it is recommended to apply light aldehyde fixation to samples prior to HPF (Sosinsky et al., 2008).

Another caveat to HPF-FS, of course, is the need for specialized equipment as both a high pressure freezing unit and a freeze substitution machine are necessary. Only recently a protocol has been published demonstrating FS without the need for a specialized machine, however an HPF machine is still required as a starting point (McDonald and Webb, 2011). The tangible benefit of the novel FS protocol is the reduction in time the entire HPF-FS process takes, reducing it from a minimum 4 days to 1 day. However, the challenges of HPF-FS do not outweigh the advantages. The excellent preservation of a huge variety of tissue types with HPF-FS makes this technique appealing for any ultrastructural study, particularly investigations requiring high-resolution data (e.g. electron tomography). The combination of HFP-FS with flat-embedding produces resin polymerized samples, which can easily be imaged with light microscopy for precision localization of targeted regions, an extremely useful feature that saves time and increases efficiency.

Interestingly, PLT produced better preservation, though still quite limited, than MW processing for chemically sensitive tissues like the eye and inner ear of the zebrafish. This is likely due in part to cooling the tissue to 4°C during the chemical fixation and -35°C during dehydration; the cooling likely slows down cell death processes during fixation provides stabilization of the tissue and slower exchange of water molecules during dehydration. While, MW processing resulted in better preservation of macromolecular structures and features, such as desmosomes, microvilli and skeletal muscle. Neither technique preserved the mechano-chemically sensitive structures of the eye (optic nerve) or inner ear (stereocilia) as well as HPF-FS, however, they are still useful techniques for a variety of reasons. MW processing has the disadvantage of also requiring a special machine, however the speed with which one can process samples is dramatically increased in this approach. Compared to conventional processing, which can take up to 3 days, MW processing can be accomplished in the span of a few hours. Additionally, the samples are exposed to chemicals for a shortened amount of time, reducing potential adverse reactions within the sample. While PLT can take the same amount of time as conventional processing, the advantage of cooling samples during dehydration can lead to increased preservation of both fine molecular structures and increased antigenicity for immunolabeling approaches (Robertson et al., 1992). Ultimately, for biological questions such as the location or presence of particular organelles, the general morphology of a cell, the nature of cell-cell interactions, etc., the use of MW or PLT processing can be more accessible and efficient than using HPF-FS.

Considering the superior preservation of tissue architecture from the nanometer to millimeter scale with HPF-FS processing as compared to other approaches, it is reasonable to conclude this to be an efficacious approach for describing novel features of tissue morphology. One might also reason that some combination of the three techniques could provide useful advantages as well, particularly for samples too large for the HPF specimen holders and which require special staining regimens for alternative electron microscopy imaging approaches, such as serial block face and focused ion beam scanning electron microscopy.

Chapter 4.
3-dimensional scanning electron microscopy methods development

Introduction

Need for new imaging modalities

A strength of TEM is its ability to study precise spatial relationships of macromolecular complexes while retaining the context of the surrounding cellular and tissue architecture. While sample preservation is no longer a concern for modern, cryo-based TEM preparation approaches, one major shortcoming of TEM analysis is that only small portions of a cell can be visualized at molecular resolution due to the fact that cells need to be sectioned to a thickness typically not exceeding 100-200 nm, which means at best 1-2% of a cell's volume can be covered this way. The conventional solution to this is to employ montaging and electron tomography on serial sections to obtain 3D information about the macromolecular complexes of interest.

Wide-field imaging or montaging of ~100 nm thin sections with TEM requires approximately 5 times the amount of time as normal TEM image collection, about 30 minutes per sample. In addition, this aggressive imaging approach would need to be coupled to serial section imaging to be capable of any meaningful 3D information of the cellular architecture. This ambitious combination would be able to cover an entire 3D cell (assume 10 μm^3) though the information of each 2D section imaged would be collapsed onto itself, effectively creating 100nm gaps between each of the 100 physical sections, which would have to be imaged. Additionally, an optimistic time investment necessary for this effort would be about 2 weeks, which assumes efficiency at all steps. Even if an expert is wonderfully efficient at this approach, several technical issues, such as section-to-section alignment, missed section(s), uneven section thickness, and distortion, are difficult to minimize and can leave significant gaps in the Z direction data.

An alternative imaging modality is TEM tomography, in which a very small subset of a cell (1-2 μm XY, 200 nm Z) is serially imaged at different tilt angles (up to 70 degrees). The collection of 2D projections are back-projected into real space to create the 3D representation of the sample; however, as it is impossible to tilt the sample to 90 degrees and still pass the electron beam through it, there is always a missing wedge artifact in any tomogram. Thus, the modalities of wide-field TEM and tomography each suffer their own issues and are poor tools for collecting large 3D high-resolution datasets of cells and tissues. FIB-SEM and SBF-SEM can overcome such shortcomings of 3D TEM approaches.

Focused Ion Beam – Scanning Electron Microscopy

FIB-SEM allows 3D imaging at a resolution comparable to electron tomography, i.e. ~4-10 nm in XY and about 4 nm in Z direction, enabling the visualization of entire cell clusters (e.g. 30 μm x 30 μm x 30 μm) at molecular resolution. FIB-SEM is considered a dual beam approach, as it employs an ablating gallium ion source beam and a separate field emission gun electron (FEG) column for imaging. Oftentimes these microscopes can be outfitted with other useful tools such as an energy dispersive detector, a plasma spray gun, and a backscatter electron detector, all typically used in material science. Indeed, FIB-SEM, also known as Ion Beam Ablation, has long been used in the material science field for a variety of chemical analyses and

semiconductor work (Munroe, 2009; Prewett, 1984; Reyntjens and Puers, 2001). This method is even widely used among electron microscopists as a way to perform complicated lift-out preparations for tomography; most recently it has been adapted for cryo-conditions and optimized for biological material lift outs for cryo-tomogram collection (Rigort et al., 2012; Rubino et al., 2012).

Utilization of a FIB-SEM for 3D imaging of a biological sample includes producing a resin embedded sample block, similar to TEM samples, and mounting it onto 45° angled aluminum pin stub, necessary for the sample to be brought to a 90° tilt within the microscope. The extreme tilt allows perpendicular positioning of the gallium ion beam to the FEG, thus preventing the need for extreme trenching and allowing near continuous imaging through the depth of the resin block. The gallium ion beam is rastered across the edge of the block face, specifically the region of interest, ablating resin of a defined thickness; the current and the aperture setting define the size of the beam. Following each raster of the gallium ion beam, the FEG is used to generate an image via the backscatter electron detector.

Serial Block Face – Scanning Electron Microscopy

SBF-SEM, as first described by Denk & Horstmann in 2004 and then commercialized as 3View™ by Gatan, Inc. in 2010, uses a FEGSEM combined with an ultramicrotome that is fitted inside the door of the SEM (Denk and Horstmann, 2004; Dohnalkova et al., 2010). The ultramicrotome consists of a 45° diamond knife controlled by a piezo motor and allows for automated ultra-thin sectioning of a resin block mounted on a piezo stage that incrementally keeps the block precisely positioned on the edge of the knife. The diamond knife, which always cuts dry, typically can cut 30-50 nm sections depending on the hardness of the resin. The FEGSEM's current is kept within a range of 0.5–5 keV in low or high vacuum for image collection on the backscatter electron detector. SBF-SEM is limited in the Z-direction to 30-50 nm gaps between images, but it allows for collection of data in Z-direction for hundreds of microns, possibly even millimeters. In XY, SBF-SEM can achieve up to 5 nm resolution; however, there is a trade-off in resolution for scale. In other words, 5 nm resolution can be achieved when the field of view/data collection area is restricted to a small region (1 μm or smaller); alternatively, by sacrificing resolution to 15 nm (or more), the field of view can be increased to cover up to hundreds of microns in area. Key to successful analysis is the generation of sufficient contrast within the resin-embedded blocks, the development of which is non-trivial.

Backscattered Electron Detection

Both FIB-SEM and SBF-SEM rely on BSE detector imaging to collect data from the surface of a block face. The use of a secondary electron detector (SED), the normal mode for SEM imaging, is mostly useless for the imaging of stained biological material at and below the surface of the resin block face. Since the SED image generation is topographically dependent, the information garnered from the flat, smooth surface is too homogeneous to generate useful data. However, the SED is a necessary tool for the overall operation of the FIB-SEM, as it is needed during the alignment and generation of fiducial markers for the automated software. Therefore, it is the BSE detector that performs all of the data collection for 3D analysis of resin embedded tissues.

Generated from a variety of sources, secondary electrons are low energy electrons ejected from the specimen's atoms by the primary electron beam, resulting from inelastic scattering originating from the top few nanometers of the surface of the sample. Alternately, backscattered

electrons are primary beam electrons that are elastically scattered back out of the sample, typically generated from slightly further into the surface of the specimen than the source of secondary electrons. Backscatter detectors are mounted in an annular fashion concentric to the primary electron beam, enabling detection of high-energy backscatter electrons, which provides the best compositional contrast information. This compositional contrast, or atomic number, comes from differences in the local chemical composition and is thus responsible for image formation. Therefore, regions of high atomic number appear bright relative to low atomic number regions. Compositional contrast is similar to using multiple shades of color to optically generate contrasting dark and light regions. Full utilization of the BSE detector depends on developing staining regimens that infuse large amounts of heavy metal atoms into a biological sample.

Staining protocols for biological samples used in BSE detection date back to the 1980's, but until very recently, they have been constrained to whole mounted tissue and cells (Friedman and Ellisman, 1981; Willingham and Rutherford, 1984). Therefore, it is necessary to generate protocols easily adapted to different kinds of tissues and biological questions while simultaneously suited for optimal tissue preservation. The typical staining regimens used to provide a non-coating fixation are osmium-thiocarbohydrazide-osmium (OTO), ruthenium red-osmium-thiocarbohydrazide-osmium (ROTO), and tannic acid-osmium (TAO). Methods for implementing the staining regimens vary from conventional bench top to high-pressure freezing (Belton, 1979; Jongebloed et al., 1999a; Leser et al., 2009). Few studies have looked at the efficacy of these stains for the 3D-SEM imaging of stained samples embedded in resin. More recently published protocols lack optimal preservation for a wide variety of sub-cellular features. Purely bench top conventional protocols have been used, but they leave cell membranes wavy and broken and can lead to extraction artifacts within cells (Armer et al., 2009; Wierzbicki et al., 2013). Use of microwave assisted sample preservation has been found to drastically reduce samples' chemical exposure times and produce robust sample preservation (Giberson and Demaree, 1995; Login et al., 1990; Wendt et al., 2004). High pressure freezing with subsequent freeze substitution reduces or eliminates dehydration artifacts, thus generating resin embedded samples with the best possible preservation (McDonald, 1999).

As BSE stains require, by definition, a great deal of heavy metal dosing in the biological sample, it is advantageous to reduce the burden on delicate cellular structures by employing microwave-assisted methods in the beginning of sample preparation. For further production of the most faithfully preserved tissue possible, high-pressure freezing and freeze substitution can be performed on samples directly following the initial heavy metal staining. Here we have developed a unified protocol combining microwave-assisted and high-pressure freezing freeze substitution techniques for the 3D-SEM preparation of human mammary epithelial cells, HMT-3522S1.

The aim of this study is to employ these advanced staining methods to investigate the three-dimensional subcellular organization of HMT-3522S1 cells that have formed acinar structures in 3D cell culture. HMT-3522S1 cells (S1 cells) are an important and prominent human-derived cell line breast cancer model that has been used for decades to study cancer progression and test cancer treatments (Kenny et al., 2007; Weaver et al., 1997). Upon introduction into 3D cell culture conditions, S1 cells recapitulate the physiologic analog to a breast duct, called an acinus (Weaver et al., 1995). Our work providing the first high-resolution 3-dimensional look into the organization of these cells reveals information about the polarization and cohesiveness of the cells that is not apparent via confocal or TEM imaging. In this study, our

new method, MW-HPF-FS, is proven to be an effective tool for complicated BSE sample preparation including OTO, ROTO and TAO. Evaluation of these stains across a range of cellular features in HMT-3522 proved them to consistently generate robust heavy metal staining ideal for BSE detection with SBF-SEM and FIB-SEM.

Experimental Procedures

HMT-3522 cell culture

2D cell culture & 3D cell culture: Were performed as described in Chapter 2.

Microwave-assisted BSE staining

HMT-3522 acini embedded in Matrigel were chemically fixed with 2% paraformaldehyde and 0.1% glutaraldehyde in phosphate buffer, except the samples stained with ruthenium red. The acini were stained with an osmium-thiocarbohydrazide-osmium (OTO), ruthenium red osmium-thiocarbohydrazide-osmium (ROTO), or tannic acid osmium-thiocarbohydrazide-osmium (TAO) method in combination with microwave-assisted processing. TAO and ROTO staining have unique beginning steps, which then converge with those of OTO staining upon introduction of osmium tetroxide.

ROTO staining was performed by incubating the acini in 2.5% glutaraldehyde and 0.05% ruthenium red in 0.1M sodium cacodylate buffer, followed by thrice rinsing in buffer. Ruthenium red adversely reacts with phosphate-based buffers, which therefore should be avoided when this staining method is used, including during OTO steps (Belton, 1979). Samples were then thrice rinsed in buffer before being incubated in 2% osmium tetroxide and 0.05% ruthenium red in buffer and microwaved for 2 minutes at 150 W. Samples were rinsed three times in double-distilled water before proceeding through the remainder of the OTO protocol, beginning at the thiocarbohydrazide incubation.

TAO staining was carried out by rinsing the samples 3 times in 0.1M phosphate buffer. Acini were then incubated in 2% arginine-HCl + 2% tannic acid in double-distilled water, using a Pelco Biowave microwave (Ted Pella Inc., Redding, CA) for 2 minutes at 150 watts of power. Samples were rinsed three times in double-distilled water before proceeding through the remainder of the OTO protocol, beginning with the second osmium incubation.

For OTO staining, acini were rinsed three times with 0.1 M phosphate buffer or water and then incubated with a solution of reduced 2% osmium tetroxide (containing 1.5% potassium ferricyanide) in buffer or water. Following three rinses with buffer or water, the acini were microwaved for 40 seconds at 150 W in 0.1% thiocarbohydrazide in double-distilled water and then rinsed three times with water. Finally, they were microwaved for 1 minute at 150 watts with 2% osmium tetroxide and rinsed three times in water. To enhance preservation and contrast, the samples were high-pressure frozen and freeze substituted with a solution of 4% osmium tetroxide, 0.1% uranyl acetate and 5% water in acetone, as outlined below.

High-pressure freezing and freeze substitution

HMT-3522 S1 acini, unfixed in matrigel or BSE stained and in water, were placed 1 mm wide by 200 μm deep aluminum freezing hats, then surrounded with 20% bovine albumin as a cryoprotectant prior to freezing. The acini were then cryo-immobilized using a BAL-TEC HPM-010 high-pressure freezer (BAL-TEC, Inc., Carlsbad, CA). The samples that had been unfixed

prior to HPF were placed in freeze-substitution medium made up of 1% osmium tetroxide, 0.1% uranyl acetate, and 5% ddH_2O in acetone. In contrast, the samples BSE stained prior to HPF were put into a freeze-substitution medium made up of 4% osmium tetroxide, 0.1% uranyl acetate, 5% ddH_2O in acetone. All samples were freeze-substituted either by using a Leica AFS2 (Leica Microsystems, Vienna, Austria) following a previously described protocol (McDonald, 2007) or by a method of super quick freeze substitution (McDonald and Webb, 2011). Upon completion of freeze-substitution, the "unfixed" acini samples were rinsed five times in pure acetone and then progressively infiltrated with an epon-araldite resin (McDonald &Muller-Reichert, 2002). Following five rinses in pure acetone, the BSE stained acini samples were infiltrated with hard-forming epon resin with accelerator according to the following schedule: 2 hours in 2:1 acetone:resin; 2 hours in 1:1; 4 hours in 1:2; and overnight in pure resin. All samples were flat embedded between two slides using two layers of parafilm as a spacer before being polymerized overnight in an oven at 60° C (Muller-Reichert *et al*., 2003).

Serial block face SEM imaging

Organoids embedded in resin were mounted onto an aluminum pin with a cyanoacrylate adhesive and colloidal silver paint. The pin, which takes the place of a normal SEM stub, was loaded into a sample holder for the Gatan 3View, (Gatan, Pleasanton, CA). Serial block face scanning electron microscopy was carried out as previously described (Denk and Horstmann, 2004). Data were collected using an FEI Quanta 600 FEGSEM; serial images were 4k by 4k and acquired at 5 keV; z-dimension slices of 50 nm; approximately 400 images were collected. Image processing was performed using ImageJ and 3D volume representations of the data were prepared using CHIMERA and Amira (Abramoff Magelhaes, P. J., Ram, S. J., 2004; Pettersen et al., 2004; Stalling et al., 2005).

Focused ion beam SEM imaging

Resin-embedded samples were trimmed with a thin razor blade to expose the area of interest on both the top and one side of the block. This was then glued to a SEM stub using colloidal silver paint. Milling and imaging of the block was carried out using a FEI Helios 650 Dual Beam FIB (FEI, Hillsboro, OR). FIB milling at 50 pA generated a beam size of ~17 nm. 4k by 4k images were collected with a backscatter electron detector at 2.5 keV; z-dimension step size of 4 nm; approximately 600 images were collected. Image processing was performed using ImageJ, and 3D volume representations of the data were prepared using CHIMERA and Amira (Abramoff Magelhaes, P. J., Ram, S. J., 2004; Pettersen et al., 2004; Stalling et al., 2005).

Transmission electron microscopy

80 to 90 nm thin sections were generated and imaged as described in Chapter 2.

Results

Effective staining for BSE imaging

Initially, we attempted data collection using S1 acini prepared by an advanced TEM sample preparation method, high pressure freezing and freeze substitution, and embedded in epon-araldite resin (Triffo et al., 2008). These samples were exposed to 1% osmium tetroxide and 0.1% uranyl acetate during the freeze substitution process and in normal TEM 2D projection

imaging the level of stain is enough to produce an image of reasonable clarity, even without secondary on-section staining with lead citrate. However, in the backscatter imaging mode of the SBF-SEM, the signal from the block surface was so low it was difficult to discern where the sample was located in the plastic background, requiring a higher accelerating voltage (7-30 keV) than is desirable (0.5 – 5 keV). Further, the backscatter electron signal from the sample was not able to produce images of cells and their contents, with only the slight outline of the nuclei visible (Figure 10).

We suspected the resin composition was also inappropriate for use in the SBF-SEM. The block surface, after exposure to the electron beam for more than a few seconds, experienced charging effects. Build up of charge at the block surface caused a slight softening of the resin, which prevented sectioning of the resin below 100 nm per slice. From that point on, the resin was changed from the epon-araldite cross-linked mixture to pure hard-forming epon resin, producing a great reduction in charging effects. Having ruled out standard TEM staining as an option for BSE imaging, we prepared S1 acini in matrigel for staining with osmium, ruthenium red and tannic acid. In an effort to both reduce the time of sample preparation and maximize tissue/cellular preservation, we developed a unified method of microwave assisted, high-pressure freezing and freeze substitution. Conventional bench top BSE staining protocols are not optimized for preservation of internal cellular structures, generally do not take into account the effect of such large doses of heavy metals on the cells used, and emphasize use for normal SEM imaging (Friedman and Ellisman, 1981; Leser et al., 2009; Schroeder-Reiter et al., 2009). Our approach utilized the speed afforded by low-energy microwaves to rapidly fix the cells and expose them to the bulk of the heavy metals in quick succession (Giberson and Demaree, 1995). Post staining, high pressure freezing of the cells allowed them to be freeze substituted, which is an established method for decreasing extraction artifacts typical of conventional ethanol dehydration, thus generating more faithfully preserved samples (McDonald and Auer, 2006).

Figure 10. BSE image of cells with typical TEM staining. S1 acini embedded in matrigel were high-pressure frozen and freeze substituted in 1% osmium tetroxide and 0.1% uranyl acetate before being polymerized in epon-araldite resin. In the SBF-SEM, with BSE imaging, only the vaguely circular rings of nuclear envelopes are discernable. Additionally, upon exposure to the electron beam, over time the resin built up enough charge at the surface to soften, making sectioning with the microtome difficult.

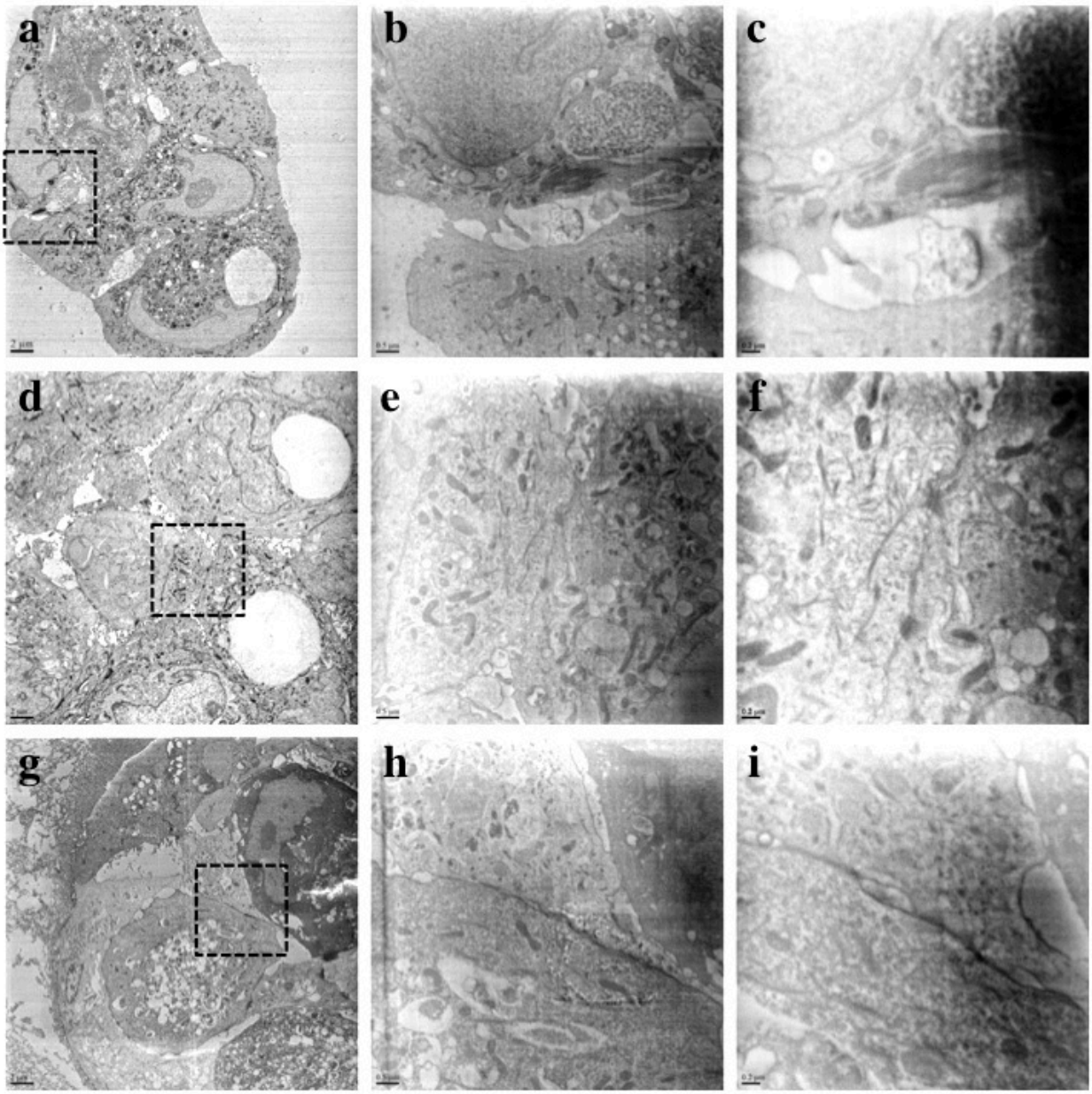

Figure 11: BSE staining efficacy and evaluation of S1 cell ultrastructure with SBF-SEM. Data was collected in backscatter mode of the 3View, SBF-SEM. The three staining approaches (**a-c**) OTO, (**d-f**) ROTO, and (**g-i**) TAO give comparable backscatter contrast. The dotted squares indicate the region of magnification for each row. The higher magnification images show signs of charging, with dark bias toward the right side of the image. The overviews (**a, d and g**) illustrate good tissue preservation across all stains. In higher magnification it is clear the OTO stain (**b, c**) and ROTO stain (**e, f**) result in very smooth plasma and internal membranes, indicating a high level of preservation with these stains. Scale bars: (**a, d, g**) 2 μm; (**b, e, h**) 0.5 nm; (**c, f, i**) 0.2 nm.

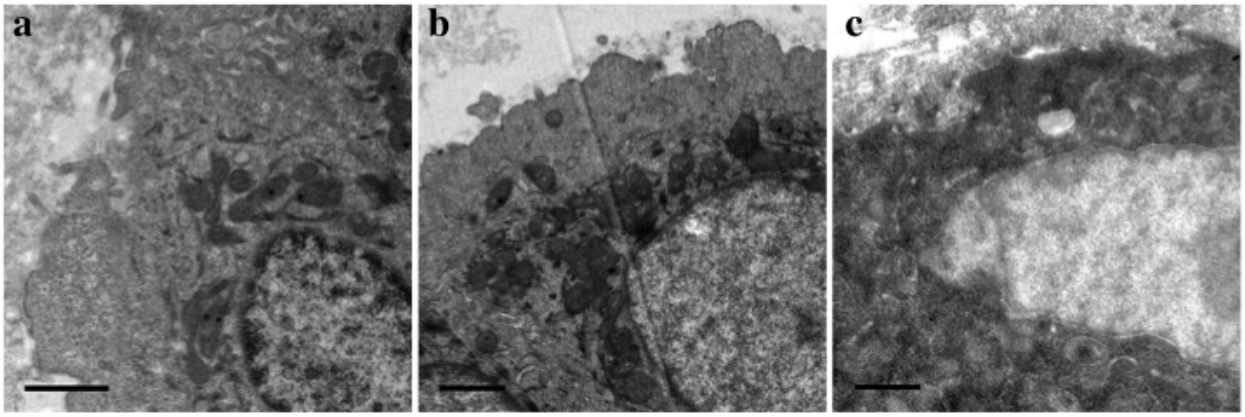

Figure 12: Stain evaluation by transmission electron microscopy. Sections of each staining regimen (**a** = OTO, **b** = ROTO, **c** = TAO) were collected onto grids and imaged with TEM. To determine whether TEM images would correlate to the level of BSE staining, the sections were not post-stained. Overall, each stain produces robust contrast in TEM, with little variation between metals. TAO, **c**, has less definition to membranes and organelles, possibly a result of over saturation. Scale bars: 1 μm.

The goal of our combined method was to produce samples with an appropriate heavy metal atomic dose and simultaneously constrain its burden on delicate structures within the cells, thus enabling high-resolution 3D data collection. Figure 11 compares the three staining approaches, OTO, ROTO and TAO as prepared by MW-HPF-FS. Imaged by SBF-SEM on a FEI Quanta at ~3 keV, the samples from all three approaches yield a strong BSE signal, producing clear images of S1 cells. At lower magnification (Figure 11 a, d, g), the three stains are comparable in signal intensity, with a resolution of approximately 15 nm X and 19 nm Y. Upon examination at high magnification, with a XY resolution of near 6 nm (Figure 11 c, f, i), the OTO and ROTO stains are clearly more effective for resolving individual mitochondria, vesicular traffic, intermediate filament bundles and ribosomes within the cytoplasm. The tannic acid stain resulted in too high a concentration of heavy metals to clearly resolve the borders between cytoplasmic contents, a result consistent with other BSE studies utilizing dual tannic acid and osmium tetroxide staining (Jongebloed et al., 1999a; Wierzbicki et al., 2013). Importantly, the preservation of the S1 breast epithelial cells was found to be very similar to previously described unfixed mammary epithelial cells that were high pressure frozen and freeze substituted (Triffo et al., 2008).

The density of TAO staining was also an issue when sections of the BSE stained samples were evaluated via TEM (Figure 12). The sections, which were not post-stained with lead citrate as is typically done prior to TEM imaging, demonstrate the intensity of the BSE staining thus providing a way to effectively pre-screen BSE staining protocols for their efficacy without needing access to a SBF-SEM or FIB-SEM. Such screening is important since TEMs are far more ubiquitous than the dual beam or serial block face enabled SEMs. However, while the mere density of the stain in TEM is obvious, it is less easily determined how finely or sharply the distribution of the staining is as demonstrated by comparing the clarity of subcellular features in Figure 12 to Figure 13.

FIB-SEM and SBF-SEM

The issue of block surface charging in the SBF-SEM led to the comparison with FIB-SEM. Additionally, to streamline data collection, we decided to use only the OTO stained samples in subsequent analysis as they were of comparable contrast to ROTO, but more easily prepared with fewer protocol steps. Using a FEI Helios 650 FIB-SEM, we collected a dataset of cells within a S1 acini up to a depth of ~2.5 microns, with a nearly isotropic voxel size of 3.7 nm X, 4.9 nm Y and 4 nm Z. The data collection process took roughly 25 hours to complete.

We also collected S1 data using the FEI Quanta 3View, SBF-SEM, over a depth of ~20 microns, with a voxel size of 15 nm X, 19 nm Y and 50 nm Z; the data collection was finished in about 6 hours. Figures 13a and 13b depict 3D representations of these datasets illustrating the difference in size between FIB-SEM and SBF-SEM data, with the latter being 2 orders of magnitude larger in volume. Figure 13c is a single image of each stack demonstrating the difference in resolving power between the two microscopes. It is important to note that these datasets were obtained at different magnifications, which certainly influenced the resolution per pixel. However, comparison of SBF-SEM images in Figure 11 to Figure 13c and Figure 14 reveals that in spite of being similar resolutions (~5 nm per pixel), the images reflect a difference in BSE signal sensitivity which appears inherent to the microscopes.

In panel (d) of Figure 13, segmented features in each dataset are displayed atop a grey-scale image for context. The primary cilium observed in panel (c), indicated by the white arrowhead, has been segmented from the volume data in Amira for further analysis. The positioning of the primary cilia at the apical surface of the cell is agreement with the proposed polarity of these acini as distinguished by immunofluorescence (Weaver et al., 1995). A disparate and irregular intercellular space was segmented out of the large volume SBF-SEM dataset as displayed in Figure 13d. The dimensional scope necessary to find indications of a defined lumen of any size is a question ideally answered by SBF-SEM. The shape, size and odd appearance of this intercellular space is not consistent with what is expected of a lumen within this acinus. Additionally, very few tight junctions are present along the edge of the intercellular space, and what appear to be irregular microvilli or filopodia are present on all surfaces of the cells not in contact with the extracellular matrix, contrary to expectations for polarized epithelia (Figure 13).

Ultrastructural analysis of S1 cells

The S1 acini were growth arrested at day 10 following embedment in matrigel for 3D cell culture. Therefore, it is reasonable to predict the cellular organization would show the hallmarks of apical-basal polarization: apical microvilli, apico-lateral tight junctions, basement membrane and apical positioning of organelles for directed exocytosis (Tanentzapf et al., 2000). Our high-resolution volumetric data suggests a semi-polarized resting state for these cells, rather than the fully polarized structure expected based solely upon immunofluorescence studies (Weaver et al., 1995; Weaver et al., 2002). Elements of polarization in the data include apically oriented primary cilia (Figure 13d), apical Golgi orientation (Figure 13c and 14a), and intermittent basement membrane deposition (Figure 14a). Unexpectedly, we observed a disorganized cell state including widespread extensive nuclear invaginations (Figure 14), few tight junctions, enrichment in desmosomes, and excessive irregular microvilli showing no polarized orientation (Figure 16). Particularly surprising were the observations of tunnels that run completely through

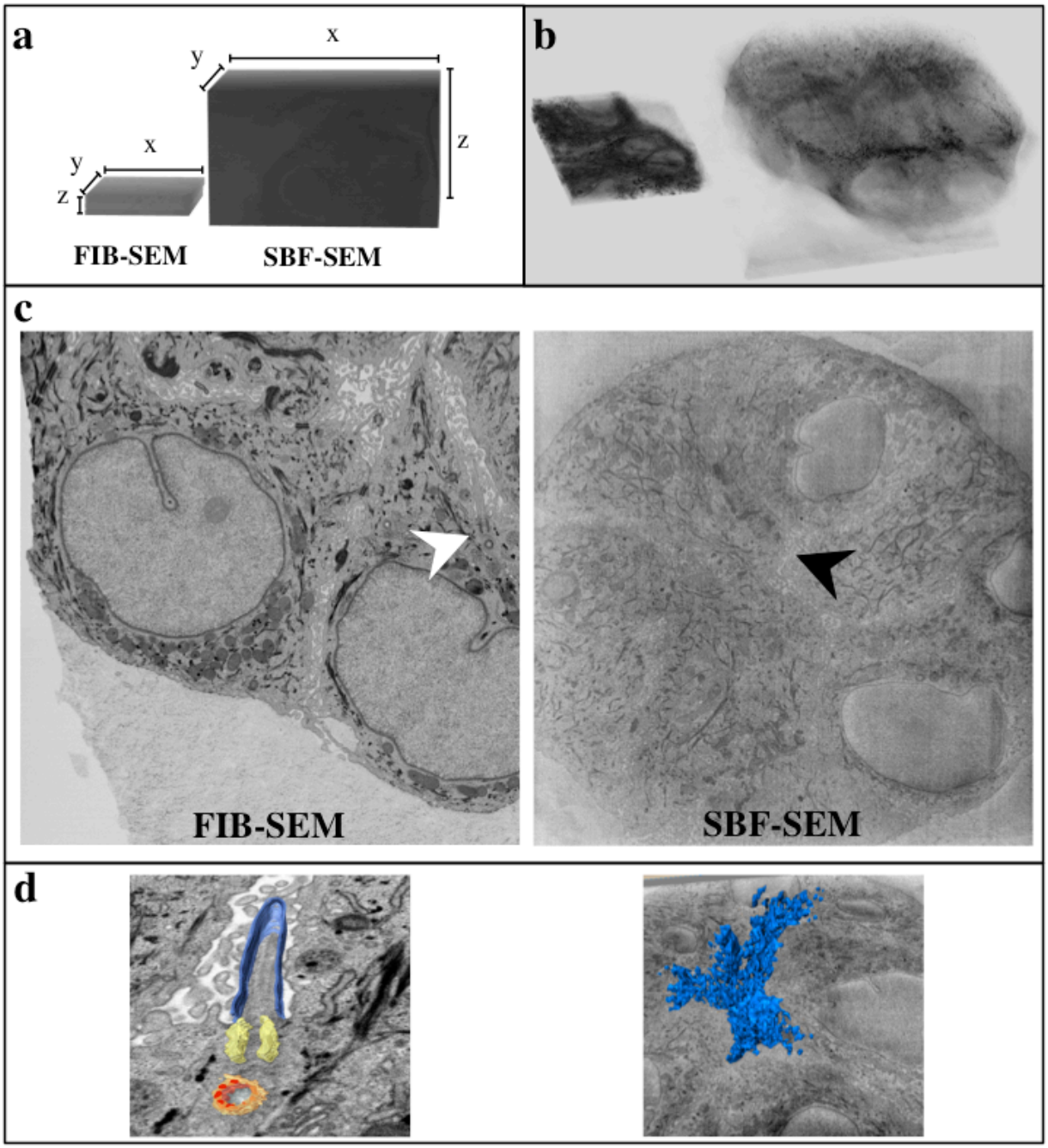

Figure 13. Comparison of FIB-SEM and SBF-SEM for BSE data collection of S1 acini. Panel (**a**) and (**b**) each demonstrate the scale size difference between a FIB-SEM and SBF-SEM dataset. With the volume of the FIB-SEM data being 540 μm^3 and the SBF-SEM is 18,000 μm^3, SBF-SEM is capable of producing datasets at least two orders of magnitude larger than FIB-SEM in a tradeoff for lower resolution, as demonstrated in panels (**c**) and (**d**). In panel (**d**), specific features were extracted out of the data: the primary cilium and basal body observed in the FIB-SEM image (white arrowhead in (**c**)) and the intercellular luminal space observed in the SBF-SEM image (black arrowhead). Scale for each panel: (a, b, c) FIB-SEM: 15.5 μm X, 14.5 μm Y, 2.4 μm Z; SBF-SEM: 30 μm X, 30 μm Y, 20 μm Z. (d) FIB-SEM: 2.7 μm X, 3.2 μm Y; SBF-SEM: 11 μm X, 11.4 μm Y.

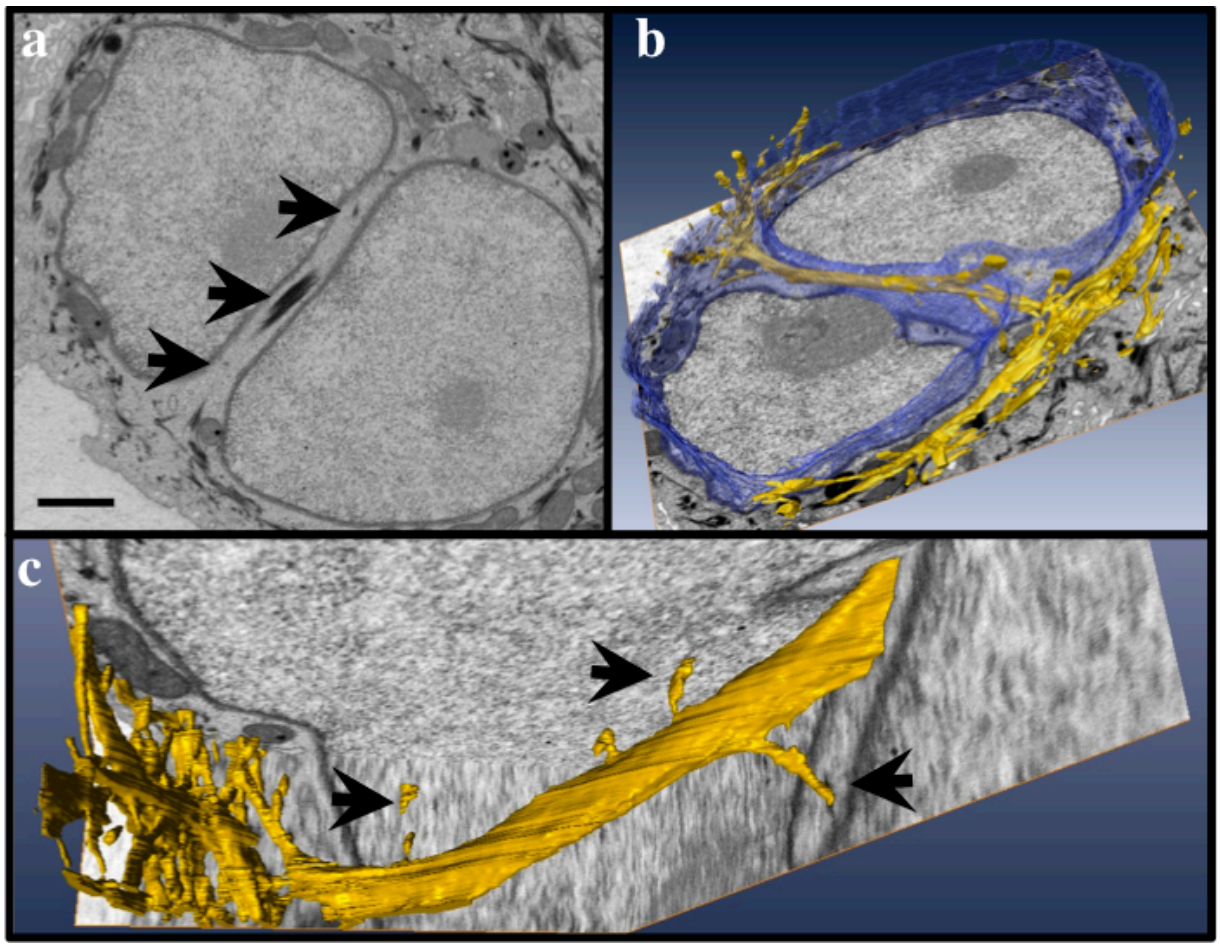

Figure 14. Nuclear invaginations and tunnels observed in S1 acinar cells. (**a**) One slice from a FIB-SEM dataset shows the thick and electron dense filament bundle inside a tunnel passing through the nucleus. Black arrowheads, the same in (**c**), point to the thick and thin pieces of the filament passing through the nucleus. (**b**) The nuclear envelope is segmented and displayed transparently in purple. The electron dense filament is observed passing completely through the nucleus within the nuclear tunnel. On each side of the nucleus, the filament is connected extensively with the intermediate filament network of the cytoplasm. (**c**) View of the segmented filament highlighting thin projections that appear to directly connect with the nuclear envelope within the nuclear tunnel. The thick filament is approximately 190 nm in diameter and runs 4.5 microns in length; the thin projections are approximately 70 nm in diameter; the tunnel itself is 430 nm in diameter. Scale bar = 1 μm.

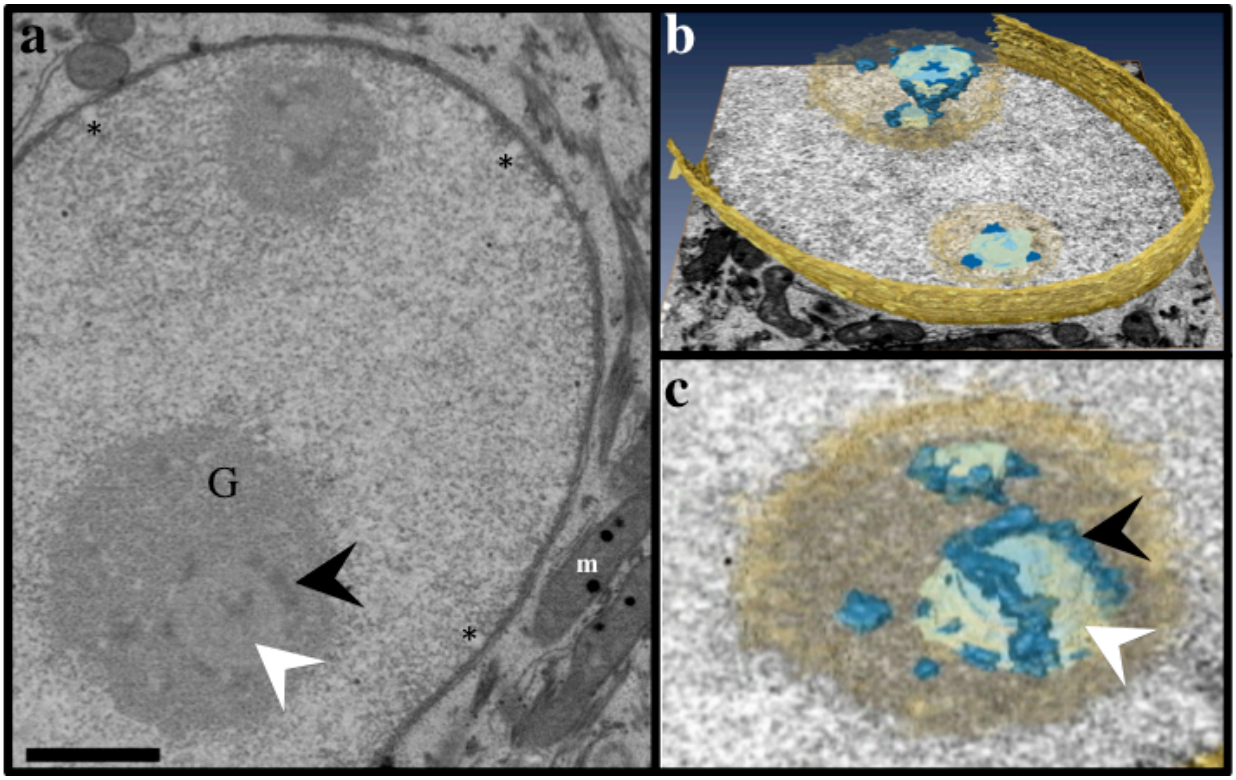

Figure 15. Tripartite staining pattern within the nucleoli of an S1 cell. The tripartite substructure of nucleoli in S1 acinar cells was observed in FIB-SEM data. (**a**) Two nucleoli are present within this nucleus. Each nucleolus contains the large (G) granular component, spherical shaped lightly stained fibrillar center (white arrowhead) surrounded loosely by the dense fibrillar component appearing more darkly stained (black arrowheads). A small amount of heterochromatin is observed, particularly nearby nuclear pores. (*) Indicate nuclear pore and (m) designates an example mitochondria. (**b** and **c**) 3D view of nucleus and individual nucleolus; dark aqua corresponds to the dense fibrillar component (black arrowhead), light aqua the fibrillar component (white arrowhead), orange shading is the granular component (G). The dense fibrillar component structure is observed winding around the outside of the more lightly stained spherical fibrillar component. Scale bar = 1 μm.

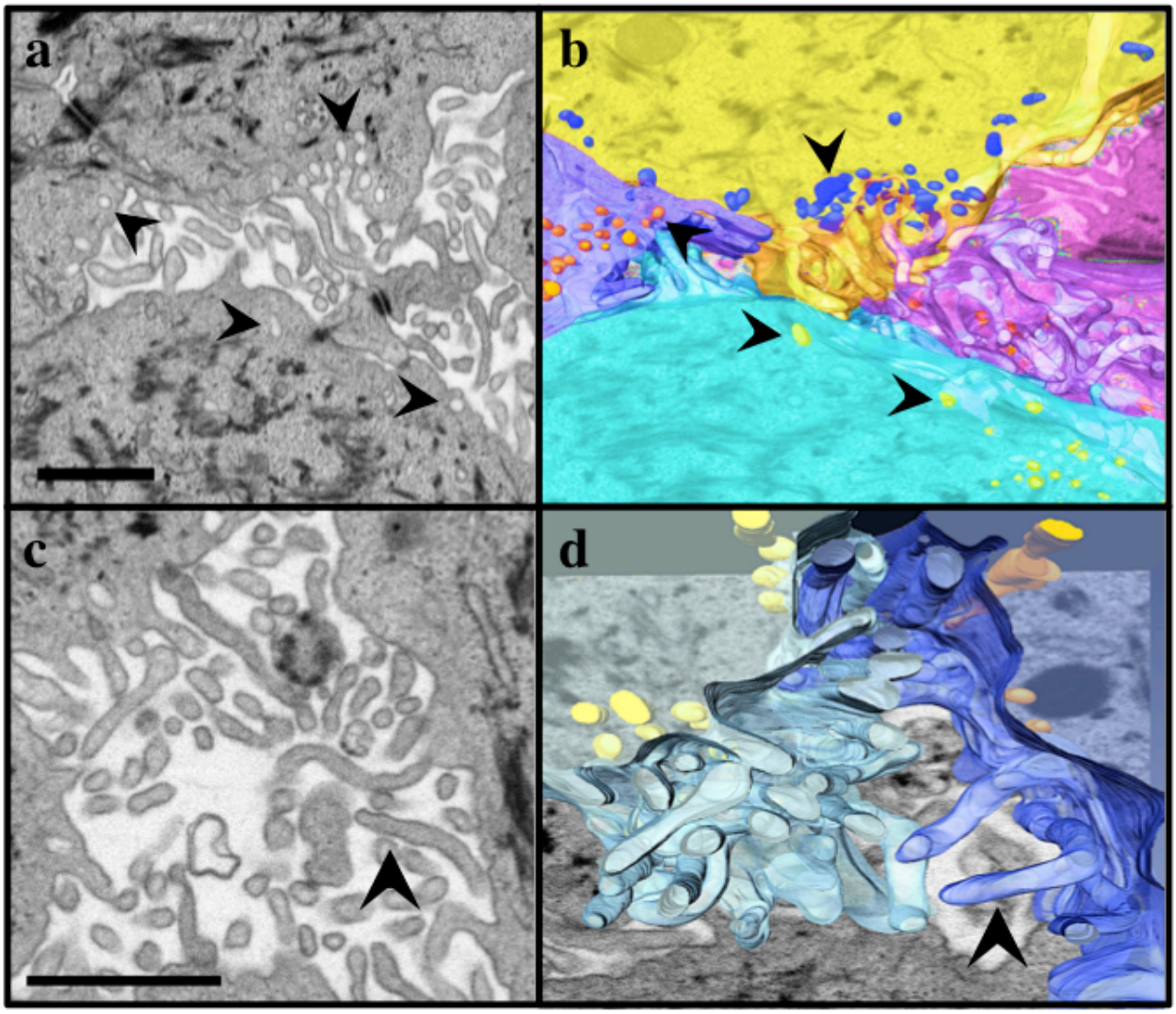

Figure 16. Extensive membrane projections and vesicular traffic at between S1 cells. (**a**) Large frequencies of vesicles at the plasma membranes near regions enriched with membrane protrusions was observed; (**b**), a 3D representation of the same area, confirms this association with an increase in vesicles corresponding to a high density of membrane protrusions originating from the same plasma membrane. The black arrowheads in (**a**) and (**b**) indicate the same vesicles in each image. The length of the membrane protrusions, as represented in (**c**) and (**d**), varied between 100 nm and over 1 micron; with the shapes occurring as everything from straight and rigid to bent and branched. The black arrowhead in (**c**) indicates the same protrusion, projected in 3D in (**d**). Scale bar = 1 μm.

nuclei and contain thick filament-like bundles of electron dense material (Figure 14). Such odd phenomena has been reported previously by Johnson et. al., findings that were limited to 2D cell cultures and hypothesized that monomeric actin was the largest component of these invaginations (Johnson et al., 2003). The authors found a correlation between nuclear activity and a higher frequency of invaginations as well as a correlation of increase invaginations with de-differentiation state. In the growth arrested state of the S1 acini it is unclear what implications these invaginations have on the cell programming.

Additionally, we found the nucleoli to be of interest as electron dense patterns were easily observed corresponding to the tripartite nucleolar structure that has been identified in other cell types and is responsible for ribosome generation (Thiry et al., 2011). Three dimensional segmentation of these 3 nucleolar components (Figure 15) reveals the dense fibrillar component snaking around the fibrillar component, suggesting a reason for the non-linear path pre-rRNA travel out of the nucleolus (Thiry et al., 2000). To our knowledge our data has provided the first 3D representation of a complete tripartite nucleolus.

Another striking feature of the S1 acini were the prevalent membrane protrusions along the interior facing surfaces of the cells. These membrane protrusions are extensive across the surfaces of the cells that do not come into contact with ECM, with a few exceptions of extensions into the matrix. Figure 16 displays the elaborate membrane protrusions extending into the intercellular space. Upon 3-dimensional rendering of the plasma membrane and peripheral vesicular traffic, it became clear there is a positive association between enrichment of membrane protrusions and vesicles at the base of the protrusions (Figure 16 a and b). These protrusions varied in length (from a few hundred nanometers to over a thousand) and shape and were observed to branch on occasion (Figure 16 c and d).

Discussion

MW-HPF-FS BSE staining

Developments in technology and new adaptations of well-established machines during the past few years have produced spectacular tools like SBF-SEM and FIB-SEM, poised to delve deep into some of biology's most complex outstanding questions, including neuron mapping of the brain and tumor heterogeneity. By building upon already established techniques, in this study we have pushed forward standard backscatter electron staining protocols and developed a method that is robust, efficient and particularly well suited for a wide-variety of tissues. The aim of this study was to employ these advanced staining methods in the investigation of the three-dimensional subcellular organization of S1 acini, grown in 3D cell culture.

The first set of experiments was conducted to evaluate the efficacy of three staining approaches that have been garnered for use with the MW-HPF-FS protocol in back scatter electron detection. Data collected with SBF-SEM confirmed that each of the stains contained appropriate levels of heavy metals for optimal BSE detection. It is also worth noting that most conventional BSE staining approaches have been used primarily for imaging the topography of critical point dried cells, rather than the fine details of macromolecular structures preserved in resin (Leser et al., 2009). Our study is one of the first to compare these stains for use in 3D-SEM microscopy with the specific purpose of 3D reconstruction of cellular features. Between the 3 stains, there were some slight differences in how the BSE signal was propagated within each sample, which could possibly be explained by the specific chemistry of each stain.

Tannic acid-arginine and osmium staining resulted in a very dense BSE signal through

out the cells, as observed by both SEM and TEM (Figure 11 and 12). Previous studies utilizing tannic acid and osmium together for increased backscatter electron signal have encountered similar results as ours (Jongebloed et al., 1999a; Jongebloed et al., 1999b; Wierzbicki et al., 2013). In those cases, the saturation of heavy metals was not an issue since the focus of the study was on topographical information of the samples rather than generating BSE signal for investigations on fine subcellular structures. TAO staining is meant to provide optimal preservation across a wide spectrum of structures, including carbohydrates and glycoproteins, often a feature of the surface of an epithelium's glycocalyx. The main component of tannic acid is galloyl glucose, which has 3 phenol groups bound to a glucose molecule; these groups can bind hydroxyl, carboxyl and sulphonic groups of amino acids; the fixation effect of tannic acid is due to phenolic radicals (Jongebloed et al., 1999b). Ultimately, we found the TAO staining to be too dense for our purposes. However, there are likely to be specific biological questions that will benefit from dense BSE staining.

Ruthenium red staining, first described in 1893 by Mangin, is specific for polysaccharides; it is an inorganic compound with a long history as a stain for polysaccharides (Carre, AH, Horne, 1927). The best results from ruthenium red staining for use in electron microscopy occur when it is combined with osmium tetroxide during *en bloc* staining (Belton, 1979; Luft, 1971a; Luft, 1971b). In this way, ruthenium should amplify the osmium signal as it provides more binding sites to react with osmium; at baseline it has 3 binding sites. From our data, the ROTO stain did not appear to provide a greater or lesser level of contrast than OTO alone. Thus, for simplicity, further experiments were carried out with only OTO as the mechanism for compositional contrast.

The osmium-thiocarbohydrazide-osmium method was developed by Seligman et. al. in 1966 with a few modifications, the most important being the addition of ferrocyanide to the first osmium step (Seligman, AM, Wasserkrug, HL, Hanker, 1966; Willingham and Rutherford, 1984). Osmium is reduced upon binding by its substrate; in regards to ferrocyanide its mechanism of action is to lower the energy of activation for further reduction, thus shifting more of the osmium in solution toward the reactive species Os (VIII) (White et al., 1979). Thiocarbohydrazide is an osmiophilic compound, which is typically added in excess to a sample previously exposed to osmium. The thiocarbohydrazide binds osmium with one of its 3 binding sites and thus, upon further exposure with osmium, the original osmium reaction site is amplified (Seligman, AM, Wasserkrug, HL, Hanker, 1966). This amplification is what generates consistent and robust BSE signal in our samples.

The OTO stain-MW-HPF-FS method produced high quality preservation of the features within the acini, from the tissue level to the macromolecular structure. A recent development enabling the excellent level of BSE content was made possible by the use of a bench top freeze substitution method. This freeze substitution method uses the property of the relatively long warm up time for liquid nitrogen frozen aluminum to gradually warm the frozen acetone-based media to 0°C, doing so over the time span of a couple hours. This approach reduces the time for the freeze substitution process from 2-4 days to 3 hours or less, thus resulting in a one day completion time for the MW-HPF-FS method (McDonald and Webb, 2011).

3D-SEM imaging

In the side-by-side comparison of the 3D image stack from each microscope (Figure 13), the scale difference of image capability is evident and striking. FIB-SEM and SBF-SEM are clearly complimentary techniques, with one being exquisite at high resolution details and the

other well suited for large scale analyses. This difference stems from many possible causes, the most important of which being that the Helios 650 (FIB-SEM) performs data collection under high vacuum conditions while the Quanta (SBF-SEM) runs in low vacuum. The vacuum status influences the accelerating voltage that the electron beam is operated at for data collection and therefore the amount of signal the backscatter detector receives. As a consequence, the SBF-SEM was run at a high voltage but detected less BSE signal than the FIB-SEM. The advantage of SBF-SEM is a greater flexibility in the size of the region of interest to be imaged, feature-oriented software (Digital micrograph 4 has packages tailored for SBF-SEM) and substantial time efficiency. The digital micrograph software is elegant and slanted toward biological user needs; it is enabled with montaging and the multi-ROI tool allows image collection to be scaled up to 100's of microns per slice. FIB-SEM is available on many platforms, FEI and Zeiss being the largest manufacturers of dual-beams. The advantages of the FIB-SEM are in the details, with high-content and high-resolution image collection easily obtainable.

Ultrastructural insights for S1 acini

Preservation of the S1 acini with the MW-HPF-FS protocol was comparable to the results previously obtained by our group using HPF-FS methods alone for breast epithelial cells, further indicating the success of the BSE staining method (Triffo et al., 2008). Imaging with SBF-SEM and FIB-SEM in tandem provided insights into the global architecture of the S1 acini as a tissue, along with exquisite nanometer resolution detail of the organization of the cells. The high volume, lower resolution data from the SBF-SEM provided detailed information about cell-cell connectivity across the entire tissue while enabling a complete view of the overall shape of an acinus, leading to the discovery of the pseudo-lumen. The high resolution, content-rich data from the FIB-SEM provided for 3D visualization of features like the primary cilium, nucleus and plasma membrane.

Interestingly, we found that there were certain structural elements of the S1 individual cells and acini as a whole that indicated either polarization of the cell or a more de-differentiated state. Our expectation was that these would be fully polarized and organized cells and tissues, in which we would visualize a well-formed lumen with apical microvilli, a band of apical tight junctions, organized organelles for polarized vesicular trafficking and a clear basement membrane. The results were a variation on those features, in which we found an extensive intercellular space (pseudo-lumen) with irregular microvilli (membrane protrusions), intermittent lateral tight junctions and an intermittent basement membrane. Additionally, we observed primary cilia apically oriented with the proper polarized vesicular traffic and organelles organized as such. In the 3D segmentation of the primary cilia (Figure 13d), it is possible to see the molecular details of the cilia, including the cilia pore complex between the base and top of the cilia (yellow, blue), recently described using cryo-electron tomography (Ounjai et al., 2013). Complete tripartite nucleoli were observed in all of the cells, appearing regular in shape and size, indicating the cell cycle has arrested. Reconstruction of the 3D ordering of the tripartite nucleolus reveal a spherical ball (fibrillar component) wrapped around by, in a snake-like fashion, the dense fibrillar component, both of which were contained within the granular component (Figure 15). This is the first 3D reconstruction of an entire nucleolus from electron microscopy; the nucleolus is particularly well suited for study via FIB-SEM, as its size places it outside the range of typical EM-tomography. It would be of interest to utilize correlative light and electron microscopy or photoconversion to investigate the localization of specific proteins known to be sequestered to the nucleolus and the machinery involved in rRNA polymerization,

questions that are as yet still unclear, with a such a high-resolution tool as FIB-SEM (Hernandez-Verdun et al., 2010; Thiry et al., 2000).

On the other spectrum of organization, the S1 cells also manifested some indicators of de-differentiated state. We have ruled out our method as any kind of cause of these features, e.g. as artifacts of sample preparation, by testing the MW-HPF-FS method with other biological samples, particularly tissue samples, which show no aberrations from their expected morphology. The two most interesting phenomena observed were the ubiquitous membrane protrusions and the highly unexpected nuclear invaginations. The membrane protrusions are likely to be aberrantly presented microvilli as they are of reasonably consistent diameter (100 nm) but of varying lengths and occur upon all surfaces of the S1 cell, which do not directly contact the ECM (Figures 13 and 16). This result, however, is in accordance with previously published data on S1 acini that demonstrates intense actin staining at all interior edges of the cells (Rizki et al., 2008). The increase in vesicular traffic at the base of the microvilli-like structures (Figure 16b) is particularly interesting, as it has been suggested that microvilli or filopodia may be involved in hormone receptor trafficking (Austin et al., 2004). Our data suggests that microvilli-like protrusions are engaged in other normal protein trafficking pathways, as the S1 cells were not treated with anything that would directly induce endocytosis. Future studies should investigate the role of these microvilli-like structures in protein trafficking and how they differ from *in vivo* microvilli and filopodia structurally.

Chapter 5.
Semi-polarized epithelium during branching morphogenesis provides physiological reference for HMT-3522 S1 3D cell culture

Introduction

The developing mammary gland remains the subject of intense study due to the potential insights to be gained for non-developmental processes like cancer metastasis. It is thought that similar mechanisms may be at play during branching morphogenesis of the ductal tree within the fat pad of the mammary gland and during epithelial to mesenchymal transition. To this end there are currently two approaches for studying branching morphogenesis: mouse models and *ex vivo* organoids.

Early ultrastructural studies of the developing mammary gland exposed transient changes in ultrastructural polarity manifested as a proliferation of intercellular membrane protrusions and reduction of cellular junctions as necessary for ductal expansion. These protrusions appear to be similar to the S1 acinus intercellular membrane protrusions we have previously described. We have utilized *in vivo* mouse mammary gland and *ex vivo* mouse mammary organoids in order to more fully characterize and investigate the potential role of these protrusions within a physiologically active tissue. The *ex vivo* organoid system has been demonstrated to adhere to a similar genetic sequence as the one employed in the *in vivo* gland development, therefore making it a viable substitute. The *ex vivo* organoids are primary cultures of mouse mammary gland fragments, recapitulated in 3D culture conditions, and can be stimulated with growth factors to grow into a branched ductal structure.

The organoids embedded in a 3D matrix provide direct access to these structures in ways not amenable to *in vivo* mammary gland. The *in vivo* mammary gland is embedded in a fat pad, which scatters light and makes real time live imaging difficult. This necessitates the dissection of the gland, which risks mechanical disruption of delicate features. Additionally, the *ex vivo* system is quite agreeable to external exposure to chemical agents and other perturbations that could cause more global system changes throughout the body if applied to an *in vivo* system. Another benefit of using the *ex vivo* organoids is the ability to halt growth of the structures at particular time points and prepare them for ultrastructural analysis with little to no mechanical disruption, important due to the transient nature of the cellular features during branching morphogenesis. The terminal end bud, where ductal expansion into the ECM occurs, is a transitory feature of the mammary gland and thought to also be relevant to the understanding of EMT, as epithelial cells must migrate and expand out into the stroma to create the length of a duct. The *ex vivo* organoid morphogenesis has previously been verified by immunofluorescence to have highly similar epithelial organization and polarity to TEB *in vivo*. Unlike other organs studied for their morphogenesis, the mammary epithelium retains the ability to reform TEB throughout the lifespan.

Here we first address the question of whether structural re-arrangement of epithelia cellular architecture can be seen in tissues that have been high-pressure frozen by using the well-documented *in vivo* mammary gland. We also set out to confirm that explantation of the mammary gland into primary culture recapitulates the ultrastructure of the *in vivo* structure, again verifying the efficacy of both the HPF-FS method and *ex vivo* culture approach. Given the interest in further understanding the morphological and ultrastructural changes associated with

branching morphogenesis, we characterized the TEB cellular architecture by TEM. In studying the organization of the multilayered epithelial TEB structure, we observed direct overlaps with the structural features of S1 acini and sought to compare the two cell arrangements for insight into the nature of transient apico-basal polarity and intercellular membrane protrusions.

Experimental Procedures

HMT-3522 cell culture

2D cell culture & 3D cell culture: Were performed as described in Chapter 2.

Ex vivo organotypic culture

Epithelial fragments ("organoids") were generated as previously described (Ewald, 2013a; Ewald et al., 2008), using 5-8-week-old Charles River FVB mice as the source material. For ease of dissection, TEBs were isolated from a 5-week-old fluorescent reporter transgenic mouse (Sca-1::EGFP) (Hanson et al., 2003). These mice were also used for the *in vivo* imaging and analyses. Animals were housed and handled in accordance with approved IACUC protocols at UCSF or JHU. To generate organoids we surgically isolated the mammary glands, minced them approximately 50 times with a scalpel and dispersed the glands for 30 min in 50 ml collagenase solution at 37°C, shaking at 100 rpm. The resulting mixture was then centrifuged at 520 X g for 10min at 25°C. We aspirated away the supernatant and resuspended the pellet thoroughly in 4 mL DNAse solution. We shook the tube by hand for 2 to 5 min at ambient temperature and then added 6 ml DMEM/F12. We then centrifuged at 520 X *g* for 10 min at 25°C and aspirated the supernatant. To separate the epithelial organoids from the single cells we used differential centrifugation, a total of 4 times. For each round we resuspended the pellet thoroughly in 10 mL DMEM/F12 and then pulsed the tube to 520 X *g* (typically 33 seconds). The resulting pellet was then resuspended in the desired volume of Matrigel (BD Biosciences Matrigel Growth Factor Reduced; #354230) and plated in 24-well non-tissue culture treated plates (more hydrophobic reducing cell adhesion to plastic) (Falcon, 351147). Organoids were grown for 5-6 days and then fixed during active branching morphogenesis.

Solutions and reagents for organotypic culture were as follows. DMEM (Dulbecco's modified Eagle's medium complete)/F12 (Gibco #11330). Collagenase solution consisted of: DMEM/F12, Fetal Bovine Serum (FBS, heat inactivated) (5% final), gentamicin (50 mg/mL), insulin (5 mg/mL final, Sigma I-5500), trypsin (2 mg/mL, Gibco #27250018), collagenase A (2 mg/mL, Type IV from Clostridium histolyticum, Sigma #C5138). DNAse I (Sigma #D4263) was resuspended at 4 U/mL in DMEM/F12. Bovine serum albumin (BSA; Invitrogen) was resuspended at 2.5 mg/mL in D-PBS. Basic medium: DMEM/F12, 1x Pen/Strep, 1x ITS (insulin, transferrin, sodium selenite, Sigma #I3146). Branching medium: Simple medium + 2.5 nM FGF2 (Sigma F0291).

High-pressure freezing and freeze substitution

Samples were pre-fixed overnight in 3% or 4% glutaraldehyde in organoid medium. They were then subjected to high-pressure freezing in a BAL-TEC HPM-010 high-pressure freezer (2,100 bars, 5-7 millisec) (BAL-TEC, Inc., Carlsbad, CA) using 20% Bovine Serum Albumin (w/v in ddH_2O) as cryoprotectant in 200 μm deep aluminum planchettes. Using either the quick freeze substitution method (McDonald and Webb, 2011) or a Leica automated freeze-substitution

system AFS (Leica Microsystems, Germany), cryofixed specimens were freeze-substituted in anhydrous acetone containing 1% osmium tetroxide, 0.1% uranyl acetate and 5% ddH_2O and after several rinses in pure acetone infiltrated with Epon-Araldite following established protocols (McDonald, 2007; McDonald and Muller-Reichert, 2002; Triffo et al., 2008). Specimens were flat-embedded between two glass slides and polymerized at 60°C over 1 to 2 days (Muller-Reichert et al., 2003). Resin-embedded samples were remounted under a dissecting microscope for precise orientation.

Transmission electron microscopy

70-100 nm sections were collected on formvar-coated grids using a Reichert Ultracut E ultramicrotome (Leica Microsystems, Germany). Sections were post-stained using 2% uranyl acetate in 70% methanol followed by Reynold's lead citrate. The sections were imaged in an FEI Tecnai 12 TEM (FEI, Hillsboro, OR) operated at 120 kV. Due to the large size of the samples, it was frequently necessary to collect multiple TEM images of overlapping adjacent areas to cover the relevant field of view at the necessary resolution. Montages of electron microscopy images were reconstructed using the freely available TrakEM2 program (Cardona et al., 2010; Saalfeld et al., 2010; Schmid et al., 2010). Images were aligned at full 2048 by 2048 pixel resolution and contrast was adjusted across adjacent images using TrakEm2. A custom python script was written to assist in reconstruction. The montage function in TrakEM2 was applied, with further manual alignment employed as necessary. Overlaps were linear blended, and montages were exported as tiffs.

3-dimensional SEM sample preparation

Mouse mammary organoids were chemically fixed with 2.5% glutaraldehyde. To produce enough back-scatter electrons for SBF-SEM imaging, the organoids were stained with an osmium-thiocarbohydrazide-osmium (OTO) method (Friedman and Ellisman, 1981; Willingham and Rutherford, 1984) in combination with microwave assisted processing, followed by high-pressure freezing and freeze substitution. Organoids or mouse tissue were rinsed 3 times with 0.1M phosphate buffer and then incubated with solution of reduced 2% osmium tetroxide (containing 1.5% potassium ferricyanide) in buffer. The samples were incubated using a Pelco Biowave microwave (Ted Pella Inc., Redding, Ca) for 2 minutes at 150 watts of power. Following 3 rinses with buffer, the organoids were microwaved for 40 sec at 150 watts in 0.1% thiocarbohydrazide in double-distilled water and then rinsed 3 times with water. Lastly, they were microwaved for 1 minute at 150 watts with 2% osmium tetroxide and rinsed 3 times in water. To enhance preservation and contrast, the samples were high-pressure frozen as described in Chapter 5 freeze substituted with a solution of 4% osmium tetroxide, 0.1% uranyl acetate, and 5% water in acetone. Following 5 rinses in pure acetone, samples were infiltrated with hard-forming Epon resin (Embed812, Ted Pella, Inc.) with BDMA accelerator according to the following schedule: 2 hours in 2 parts acetone: 1 resin; 2 hours in 1:1; 4 hours in 1:2; overnight in pure resin. Resin infiltrated samples were flat embedded as described for the TEM samples.

Focused ion beam and Serial block face SEM

Organoids embedded in resin were mounted onto an aluminum pin with a cyanoacrylate adhesive. The pin, which takes the place of a normal SEM stub, was loaded into a sample holder for the Gatan 3View (Gatan Inc., Pleasanton, Ca). Serial block face scanning electron microscopy was carried out as previously described (Denk and Horstmann, 2004). Data was

collected using an FEI Quanta 600 FEG SEM; serial images were 4k x 4k and acquired at 5 kV; z-dimension slices of 50 nm. 3D volume representations of the data were prepared using CHIMERA (Pettersen et al., 2004). CHIMERA and Amira were used to perform manual segmentation of membranes and to display the 3-dimensional volumes (Stalling et al., 2005).

Resin-embedded samples were trimmed with a thin razor blade to expose the area of interest on both the top and one side of the block. This was then glued to a SEM stub using colloidal silver paint. Milling and imaging of the block was carried out using a FEI Strata 235 Dual Beam FIB (FEI Inc., Hillsboro, OR). FIB milling at 50 pA generated a beam size of approximately 17 nm. 1k by 1k images were collected with a backscatter electron detector at 5 kv.

Antibody Staining

Staining for E-cadherin (Zymed, 13-1900), ZO-1 (Chemicon, MAB1520), β-catenin (Santa Cruz, sc-7199), and aPKC-ζ (Santa Cruz, sc-216) was done as previously reported (Ewald et al., 2008). Briefly, organoids were equilibrated in 25% sucrose in PBS for 1 hour, fixed in cold 1:1 methanol:acetone overnight at –20°C, then re-equilibrated in 25% sucrose in PBS for 1 hour. Samples were blocked 1 hour with 5% serum, incubated with primary antibody (all 1:250 in PBS) for two hours to overnight and rinsed three times in PBS. Secondary antibodies (Molecular Probes Alexa series, all 1:250 in PBS) were incubated with the organoids for 1-4 hours. Nuclei were stained with DAPI or propidium iodide (1:1000) (Molecular Probes). Antibody stains were done at least 3 independent times, inspecting a minimum of 25 organoids in each condition each time.

Confocal imaging

Confocal imaging was done on a Solamere Technology Group spinning disk confocal microscope (described in (Ewald, 2013b)), with a 40x C-Apochromat objective lens (Zeiss Microimaging). Acquisition of both fixed and time-lapse images was done using a combination of μManager (Edelstein et al., 2010) and Piper (Stanford Photonics). Levels were adjusted in Adobe Photoshop to maximize clarity of the images. Level adjustments were always done on the entire image.

Results

High-pressure frozen core biopsies of mammary glands of 7-10 week old mice illustrated the ideal sample preservation obtained in the simple epithelia which displayed typical epithelial apico-basal polarity. Luminal epithelial cells were columnar, banded together closely by apico-lateral tight junctions and lined at the apical surface with distinct microvilli. Luminal cells also display the expected polarized organelle orientation, with basally located nuclei and apically positioned Golgi apparatus. The epithelial and myoepithelial cells have occasional intercellular membrane protrusions, but do not display any large gaps between cells. A dense basement membrane lined the basal edge of the myoepithelial cells with hemidesmosomes populating the length of the membrane. In the stroma, occasional fibroblastic cells are observed amongst the cords of collagen and thatches of other filamentous matrix proteins, like fibronectin. These results conclusively demonstrated in an epithelial tissue, HPF-FS does not cause cellular rearrangements at any scale, micro or macro.

We investigated whether 3D Matrigel cell culture was able to permit the mammary gland primary culture to reform properly to mimic the *in vivo* gland. In the absence of growth factors, the *ex vivo* mammary gland will form a polarized cyst (Ewald et al., 2008). When subjected to high-pressure freezing and analysis by TEM it was confirmed that the polarized cysts have nearly identical ultrastructure as the *in vivo* mammary gland from which they originated (Figure 17). This suggested that the cell culture of mammary epithelial tissue was capable of robustly and comprehensively acting as a substitute for the *in vivo* mammary gland epithelium.

Having established the relevance of using the *ex vivo* system for recapitulation of the mammary gland in cell culture and demonstrating the ability of HPF-FS to faithfully preserve such tissues, we sought to determine the transitional ultrastructural changes that occur during branching morphogenesis. Specifically, we hypothesized that a reduction in apico-basal polarity marked by the occurrence of intercellular spaces filled with membrane protrusions would occur during the transiently stratified epithelium of mammary morphogenesis.

Upon epithelial growth factor stimulation, the simple mammary epithelium in 3D culture forms a transient multilayered epithelium, which bifurcates and expands out by elongation before returning to a polarized simple epithelium (Ewald et al., 2008; Ewald et al., 2012). During this transition, confocal microscopy of the TEB reveals that aPKC-ζ and F-actin relocate from the apical surface to all interior cell-cell contact surfaces, suggesting that interior cells lack segregated apical and basolateral membrane domains (Figure 18). Additionally, β-catenin and E-cadherin, two proteins known to be part of adherens and tight junctions, were observed along all interior cell surfaces. Transmission-EM two-dimensional micrographs reveal a complex mixture of cell shapes and features within the TEB. A range of cell shapes were observed, including long and nearly fibroblastic shaped, columnar, cuboidal and round, and squamous. Two types of intercellular spaces that appear to be lumen were identified: electron lucid with membrane protrusions and electron dense. A general reduction in observable cellular junctions was observed within the multilayered TEB, with the few tight junctions being confined to lining the electron dense lumens. Few desmosomes were observed as well, with the majority of those identified being immature. No basally located filamentous cellular projections were observed protruding from the expanding edges of the TEB into the surrounding ECM, which is consistent with previous confocal observations (Ewald et al., 2008).

Previously, small spaces with zona occludens protein 1 (ZO-1) staining, usually associated with tight junctions, were observed by confocal immunofluorescence within regions of the TEB (Figure 19 A-B') (Ewald et al., 2008). It remained unclear whether these ZO-1 stained regions indicated aggregates of junctional complexes, or molecular components of distinct small lumen. Though 3D confocal scanning could demonstrate that the ZO-1 stained regions were in some instances physically separated from the main lumen, it remained unclear what physical shape these staining markers were taking until TEM analysis (Figure 19 C-D""). The TEM ultrastructural analysis revealed small regionally isolated lumens sealed off by adjacent cells linked together through tight junctions. Additionally, the interior spaces of the microlumen were filled with characteristic microvilli brush border. Further, using 3D-SEM serial block face imaging, we discovered these microlumens are indeed separated from the main lumen and had an unexpected asymmetrical funnel shape (Figure 19 E'). The position and composition of these structures were consistent with the confocal studies and are likely the same structures.

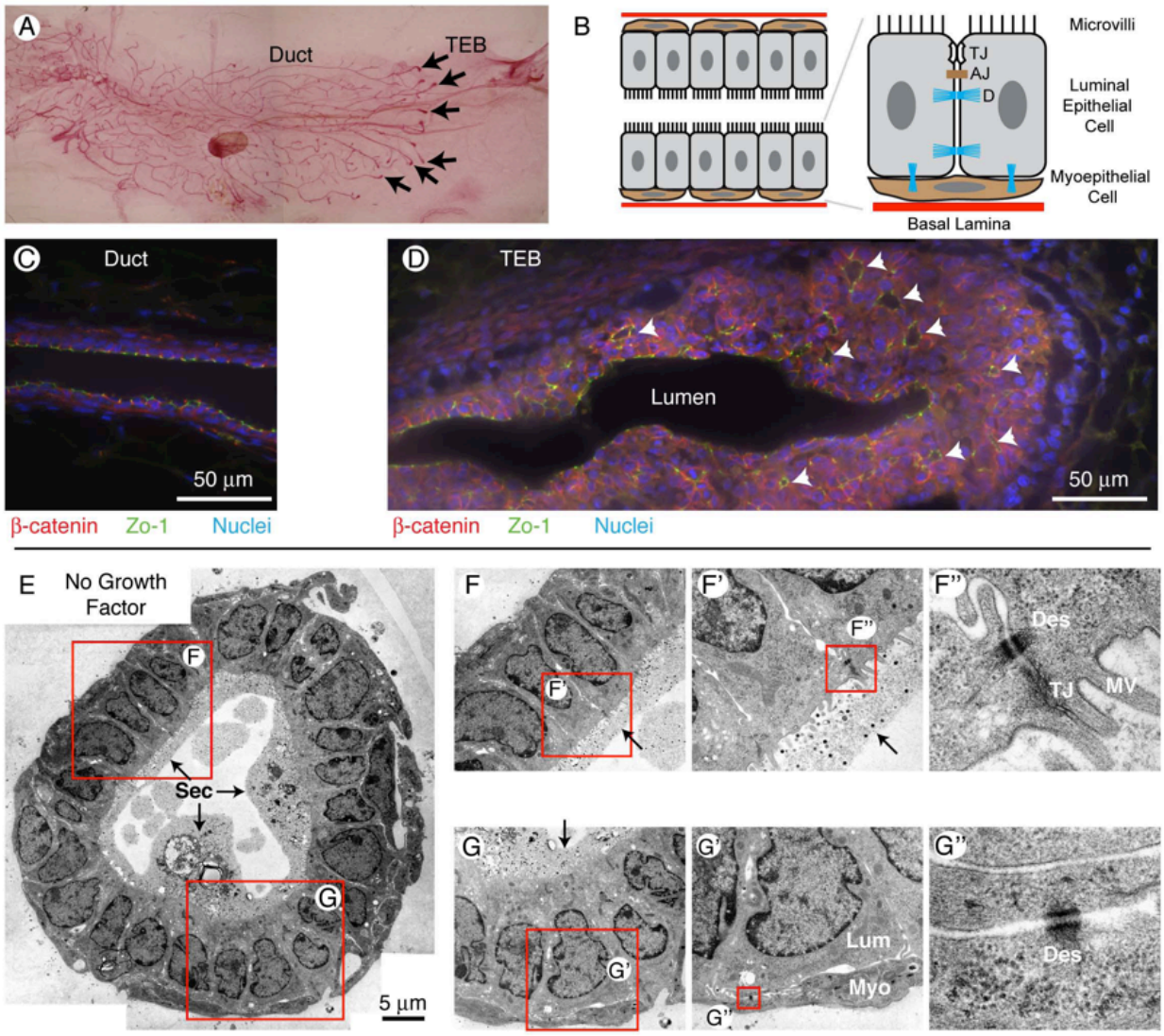

Figure 17. HPF-FS faithfully preserves ex vivo and in vivo mammary tissues. (A) 10 week old pubertal mouse mammary tissue contrasted with carmine-red (Ewald et al., 2008). Terminal end buds are indicated. Schematically represented (B) and fluorescently stained tissue (C) of polarized resting mammary epithelium depict apical basal polarity of cell junctions and microvilli. (D) Terminal end bud structures at caps of ducts elongate into the ECM. Altered ZO-1 and β-catenin staining indicate the stratified structure of the TEB may be un-polarized and have small regions of aggregated markers of polarity (white arrowheads). (E-G) TEM of HPF-FS prepared primary mammary duct grown in 3D matrigel cell culture. (F-G) Without growth factors, organoids develop into bilayered polarized cysts with apico-basal polarity in luminal and myoepithelial cells. (TJ, tight junction; Des, desmosome; Myo, myoepithelial; Lum, luminal; MV, microvillus; Sec, secretory material)

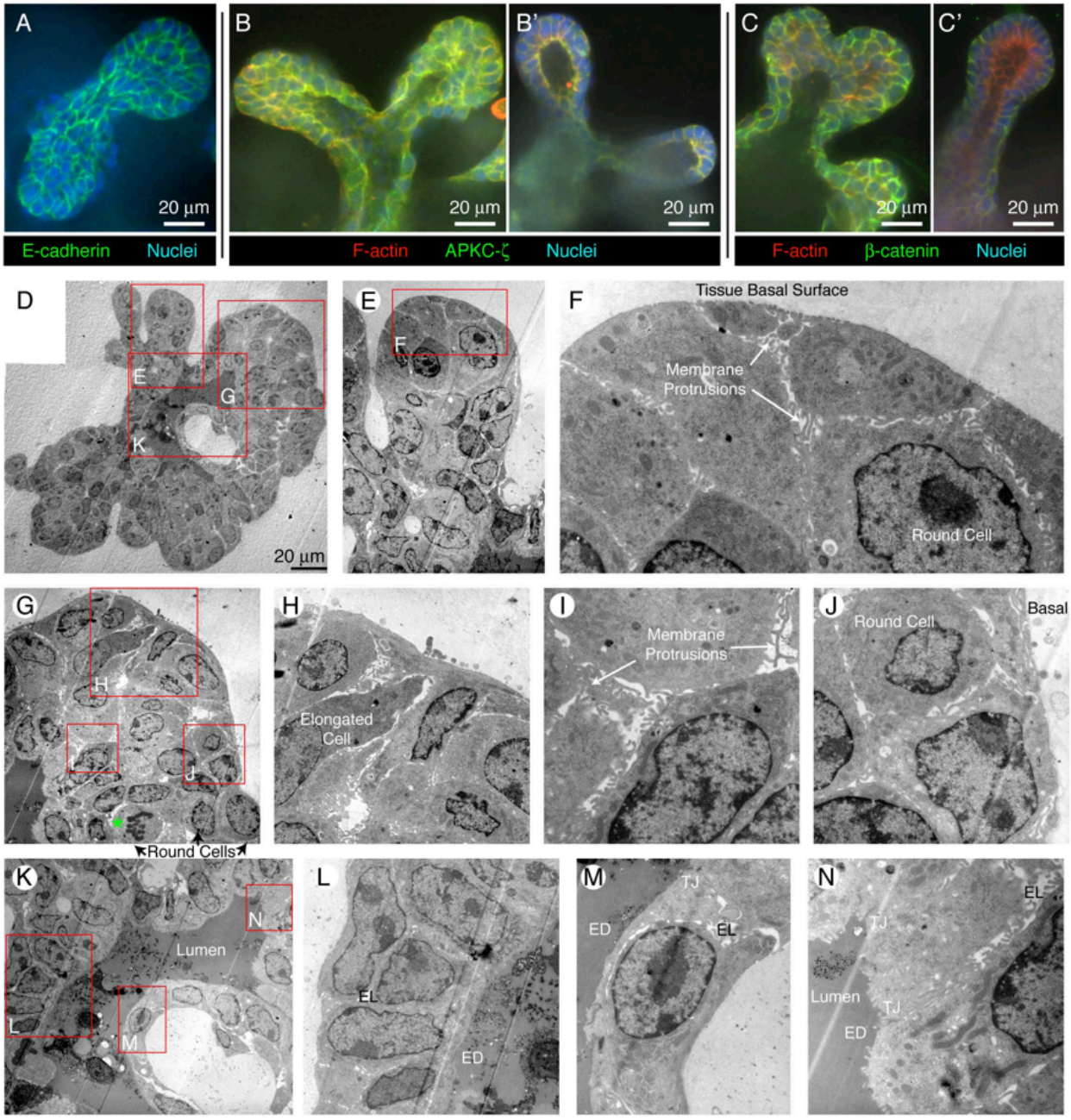

Figure 18. Mammary morphogenesis in ex vivo primary cell culture occurs by transiently stratified epithelium. (A-C') Confocal imaging verified the stratified epithelium was multi-layered and contained cells not physically in contact with the main lumen or basal-ECM surface. Molecular markers of epithelial polarization are observed on the interior facing cell surfaces, (A) E-cadherin, (B) aPKC-ζ, (C) β-catenin; and upon return to the resting state, the markers are again physically restricted to apical (B') or basal surfaces (C'), indicating a polarized simple epithelia. (D-N) Wide-field and high magnification TEM was employed to directly visualize ultrastructural markers of polarity. (D-F) The basal surface of the TEB in contact with the ECM is organized and lacks extracellular extensions into the ECM. Extensive membrane protrusions are observed between cells in an electron lucid space (F-J). Cell division of a round cell is observed away from the leading edge and lumen (G, *) and elongated cells spanning the length

of multiple cells within the TEB is observed (H). (K-N) Regions within the TEM form simple epithelia that line electron dense lumen sealed by tight junctions. (ED, electron dense; EL, electron light; TJ, tight junction)

One of the most prominent features of the TEB ultrastructure and one that is particularly ill-suited for study by confocal microscopy due to their size and uncertain molecular composition were the extensive and interdigitating membrane protrusions of the electron lucid intercellular spaces. The membrane protrusions were almost exclusively localized to regions with few visible cellular junctions. Confocal microscopy of these regions suggests the membrane protrusions are actin-rich structures, because of the significant enrichment of actin staining at interior intercellular regions, yet TEM analysis failed to identify any organized filamentous actin within. By TEM we observed that sometimes the membrane protrusions appeared to be interdigitating microvilli, but these finger like projections were far removed from the apical surface of the cells and would often occur intermixed with desmosomes. The membrane protrusions could be several microns in length or only a dozen nanometers. We first attempted to analyze the structure of the protrusions by serial section TEM, for which we used up to a dozen serially cut 90 nm sections. Technical limitations of this approach limited our ability to make concrete conclusions, largely because each section would suffer from warping, loss or damage during the process of section collection onto EM grids and post-contrast staining. This made tracking of features tremendously difficult; therefore, we decided to employ 3D-SEM to address our questions. Through analysis of the structures with 3D-SEM serial block face, we discovered that through the z-layers a membrane protrusion would embody both thick and thin characteristics, short and long lengths, and linear and branching morphology.. The dynamic sizes and shapes of the membrane protrusions were found throughout the TEB. The occurrence and prevalence of the membrane protrusions in the TEB resembled the same in the S1 acini. A comparison of the membrane protrusions of S1 and TEB samples rendered in 3D demonstrate the structural similarities.

After thoroughly characterizing the multilayered epithelia TEB grown in 3D cell culture and having found highly dynamic and somewhat unexpected features, we sought to verify that these structures were consistent with those found *in vivo*. The *in vivo* TEB also displayed reduced polarity as evidenced by a reduction in junctional complexes, proliferation of intercellular spaces filled with membrane protrusions and a variety of cell shapes. The lumen of the expanding duct was lined with tight junctions and microvilli brush border. Additionally, we also observed isolated microlumens within the TEB, which were properly sealed with tight junctions and lined with microvilli. The basal surface in contact with the ECM was well organized and we did not observed cellular protrusions into the stroma.

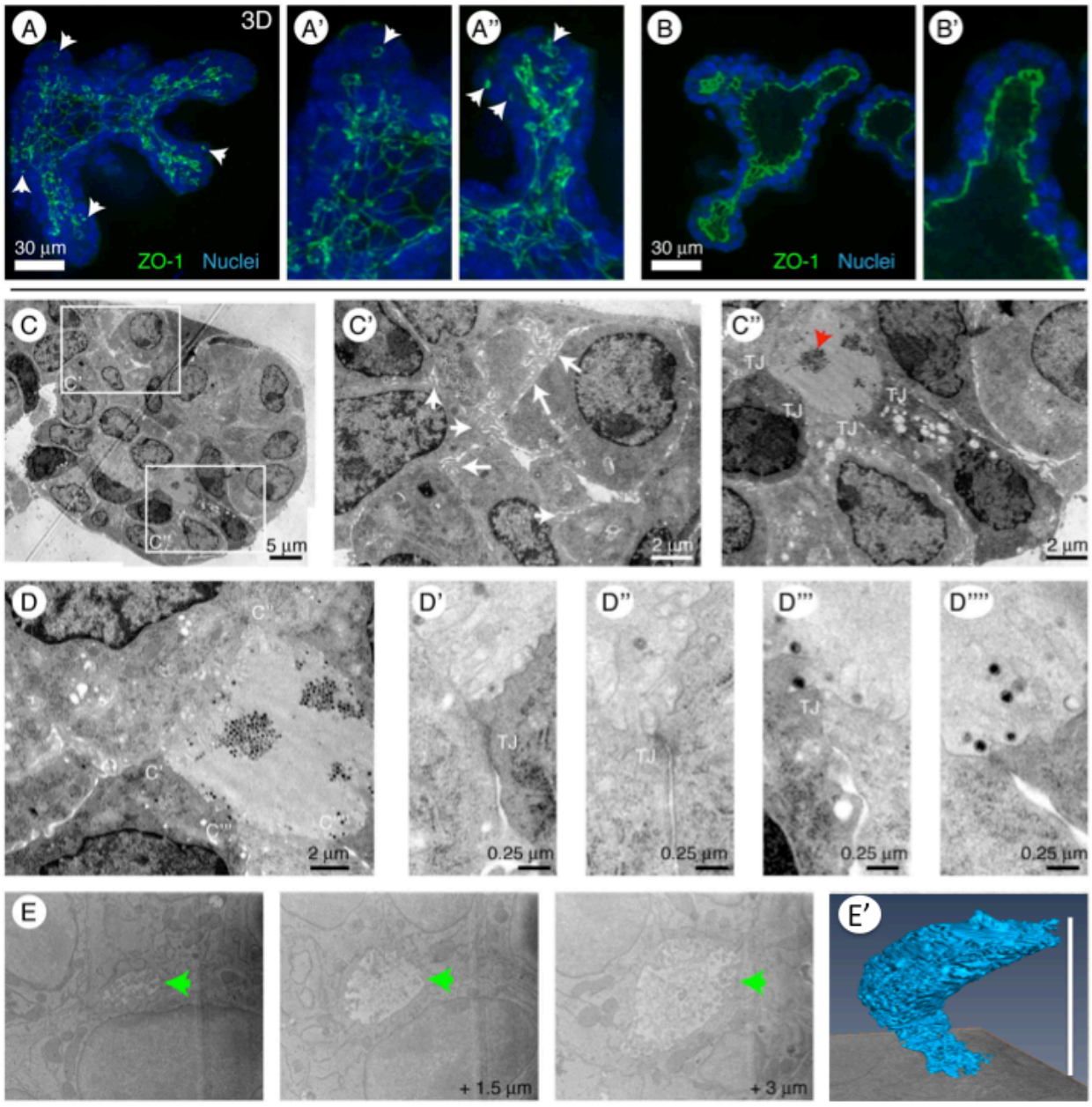

Figure 19. Punctae of ZO-1 staining correspond to isolated polarized microlumen within the multilayered epithelium. With confocal microscopy, small regions of ZO-1 staining were observed (A- B'). To investigate the nature of these areas, wide-field TEM imaging was employed (C-D). TEM revealed two types of intercellular spaces, electron lucid not framed by tight junctions (C') and those that are framed by tight junctions filled with secretory material (C''-D''''). 3D-SEM volumetric analysis revealed these spaces are isolated from the main lumen (E-E') and the microlumen have unusual asymmetric shapes (E' scale bar 10µm; TJ, tight junction).

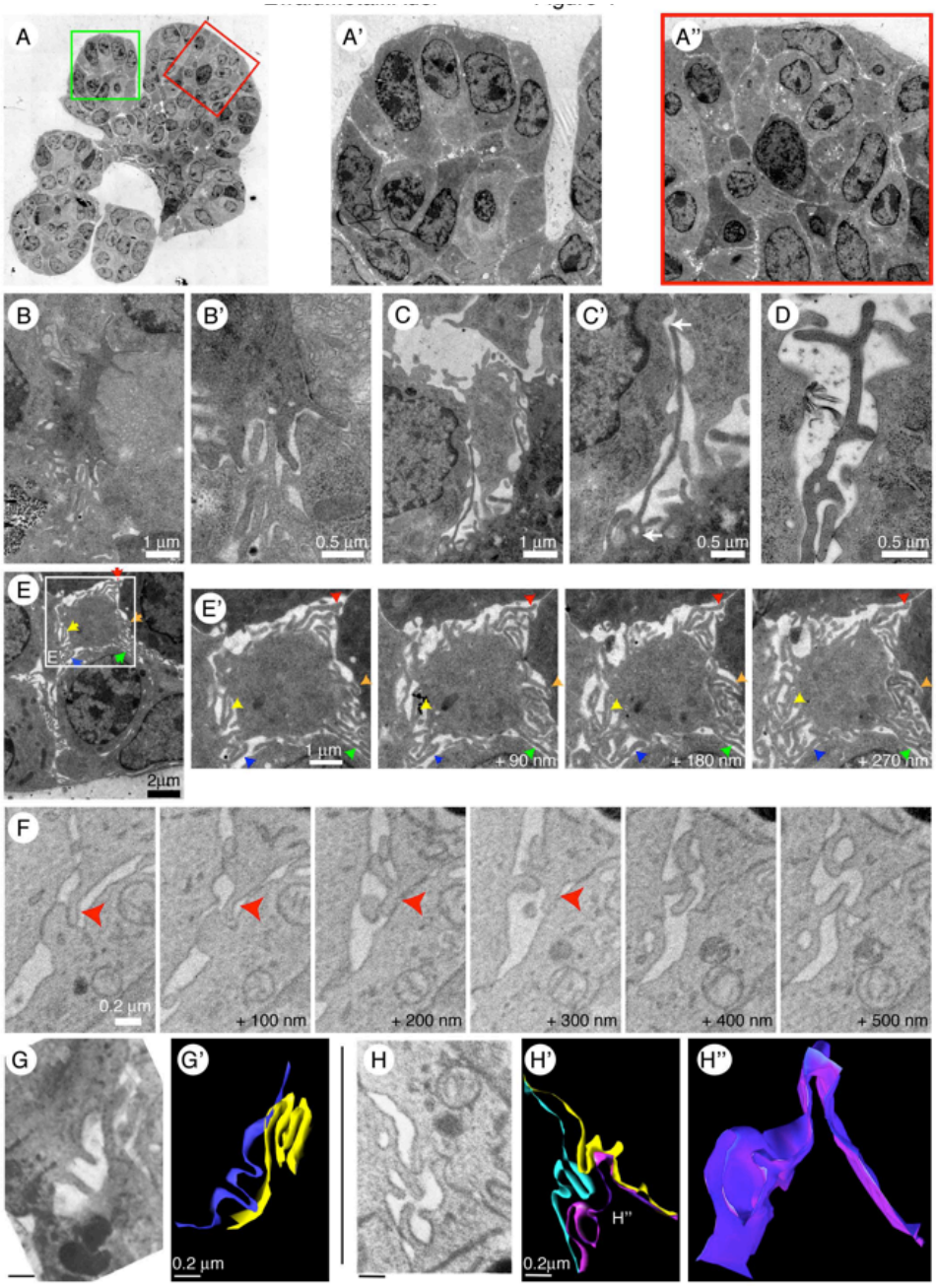

Figure 20. Cell shape heterogeneity and multi-modal investigation of membrane protrusions. Within adjacent regions of the TEB, a variety of cell shapes were observed (A-A"), where some cells have a typical epithelial columnar shape (A') and others have round to elongated shapes, at times wrapping around adjacent cells. (A"). Extensive membrane protrusions were often observed to interdigitate (B'), extend for microns (C, C') and appear as branched (D). Although serial sectioning with TEM analysis (E-E') revealed protrusions can extend through multiple sections (colored arrowheads), it proved too difficult to fully analyze the structures due to gaps in the z-direction (100 nm gaps). 3D-SEM, serial block face imaging (50 nm gaps) was therefore employed and revealed a variety of sizes of membrane protrusions that were often densely interdigitated (G-H")

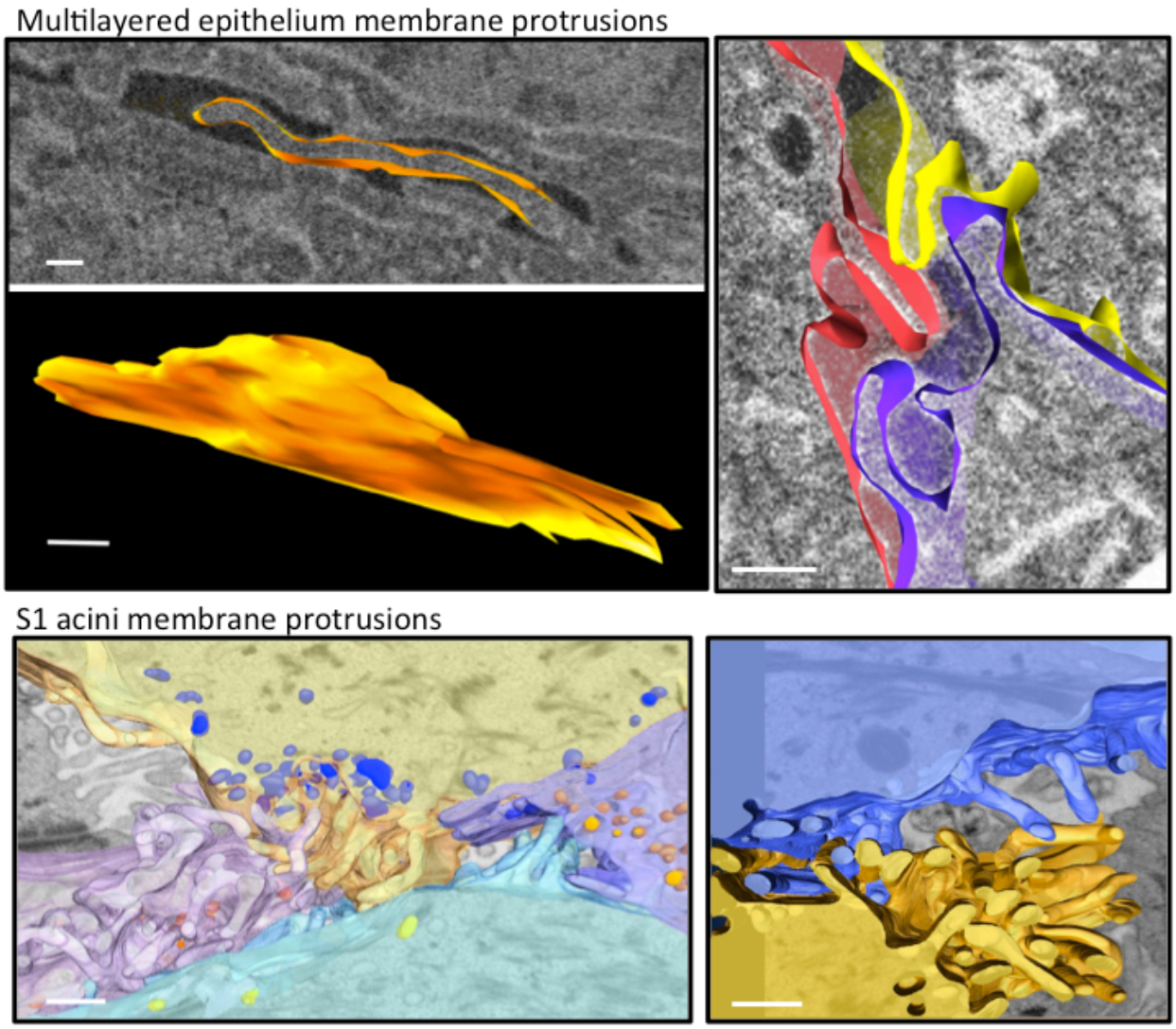

Figure 21. Structural and morphological similarities of membrane protrusions in multilayered epithelium and S1 acini. 3D-SEM imaging and 3D reconstructions of membrane protrusions within the inter-cellular spaces. Both multi-layered epithelia and S1 acini protrusions are similar diameter, varying lengths and orientations, and highly interdigitated. Both tissues were prepared by OTO-MW-HPF-FS; TEB imaged by SBF-SEM, S1 acini imaged by FIB-SEM. Scale bars are 200 nm.

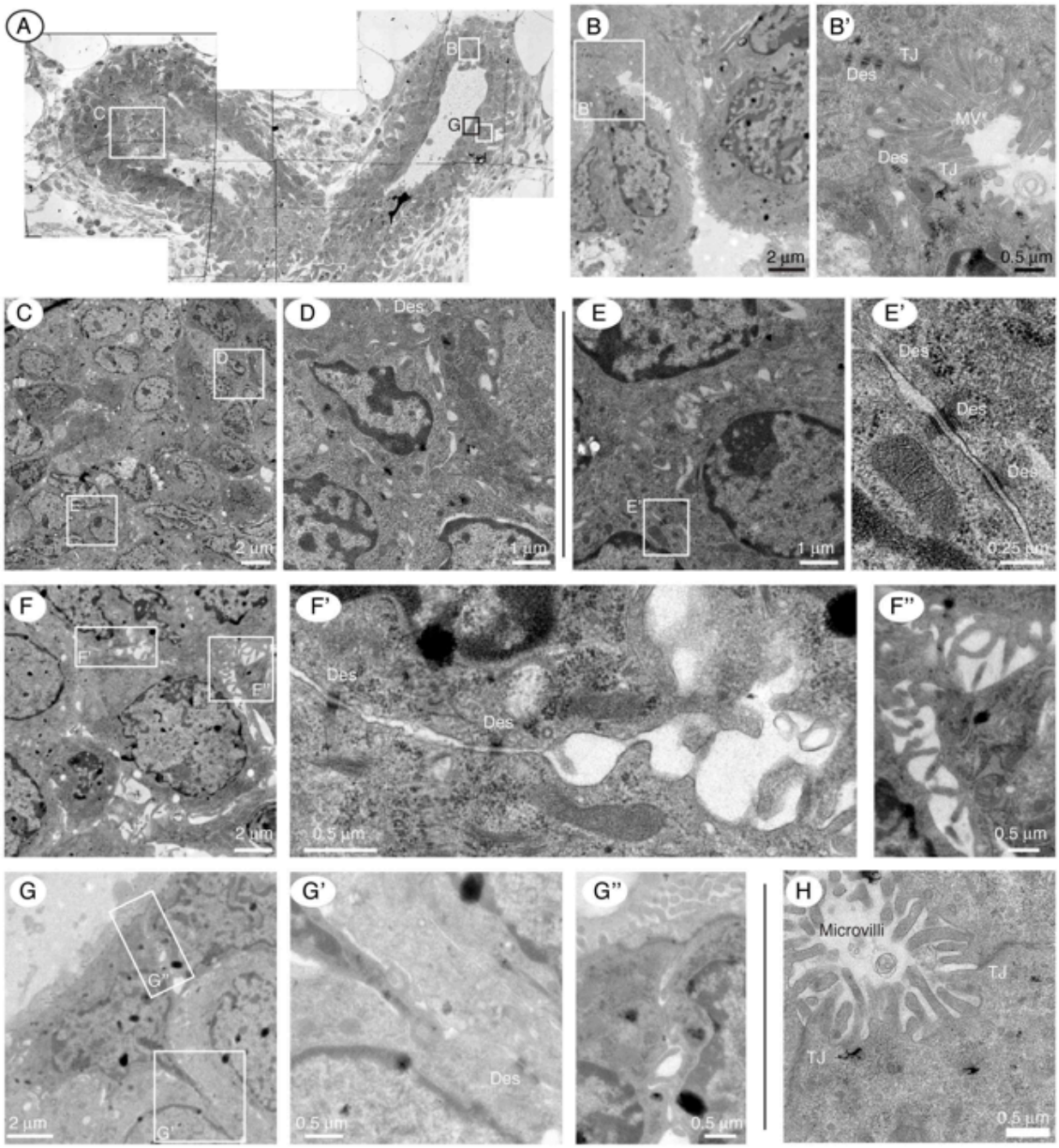

Figure 22. In vivo TEBs have high similarity to ex vivo TEBs, with reduced polarity and intercellular membrane protrusions within the multilayered epithelia. (A) Wide-field TEM of *in vivo* mammary gland undergoing branching morphogenesis. (B-B') Farthest edge of lumen displays cellular polarity, apical microvilli and properly ordered tight, adherens and desmosome junctions. (C-E') Cells within multilayered epithelium are unpolarized, primarily connected through multiple desmosomes and contain intercellular spaces. A variety of cell shapes within the multilayer are observed. (F-G") Cells along lumen display apical markers of polarity (G-G"), but not basal (F-F"). Just as in *ex vivo* TEBs, no polarity is displayed at the basal surface of lumen epithelial cells. Instead, desmosomes and membrane protrusion filled intercellular spaces are predominant (H).

Discussion

High pressure freezing and freeze substitution ensured that the mammary gland ultrastructure remained intact and unaltered by the sample processing, allowing for its thorough evaluation through TEM. As expected, HPF-FS was not found to alter the mammary gland's structure or organization from the macro-scale of microns down to the nanometer subcellular details. The ultrastructure of the *in vivo* sample was also directly comparable to that of the *ex vivo* primary mammary cyst formed in 3D cell culture without growth factor stimulation. The primary mammary organoid developed a bilayer epithelium with apically located microvilli brush border and continuous tight junctions sealing the lumen, with desmosomes closely connecting cells along the lateral surface. The organization of this epithelium is consistent with previously described ultrastructures of resting mammary epithelia (Ozzello, 1971; Pitelka et al., 1973).

During branching morphogenesis, the mammary epithelium undergoes a transient reduction in polarity as observed by molecular markers for cellular polarity. Unexpectedly, within the multilayered epithelium, this reduction in polarity is confined to the interior-facing cell surfaces. Cell surfaces that come into direct contact with lumen are apically polarized, while cells in contact with the ECM are basally polarized. Cells on the interior of the transiently stratified epithelium are loosely connected by interdigitating membrane protrusions and desmosomes. This semi-polarized state is paralleled in the human mammary epithelial cell S1 acinus. The highly disordered membrane protrusions of a variety of lengths and shapes are abundant in both epitheliums. Desmosomes serve as the main cellular junction between cells in both structures as well. Though desmosomes are typically more abundant in S1 acini than in TEB, the S1 have an occasional isolated tight junction next to an intercellular space. It is unclear whether these differences are the result of the S1 cells being human, being serially cultured, or generally being fewer in number. Both epithelial structures feature extensive interdigitating membrane protrusions within electron lucid intercellular spaces and polarized cell surfaces that contact the ECM.

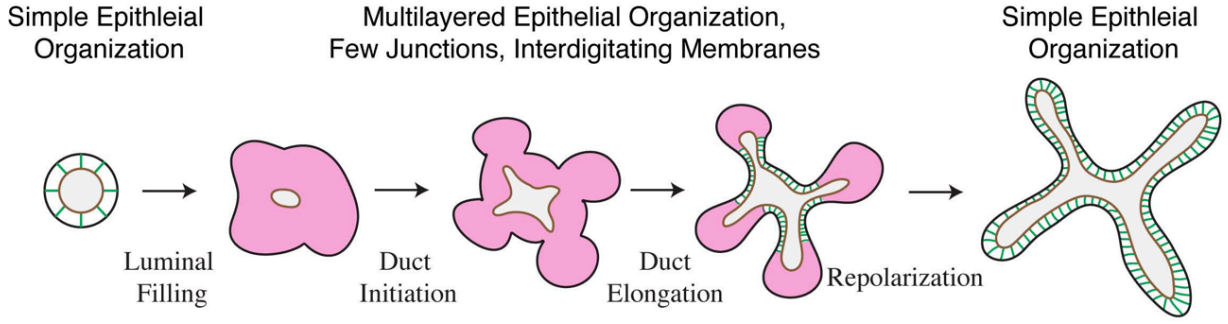

Figure 23. Overview of branching morphogenesis. Schematically displaying the transition from a resting mammary gland with polarized simple epithelium to ductal infiltration. The terminal end buds, or transient multilayered epithelium, present during bifurcated ductal elongation are the front edge of expansion into the surrounding stroma. Upon completion of expansion, the duct is re-polarized to form a bilayered simple epithelium with luminal epithelial cells surrounded by supporting myoepithelial cells.

Comparison of the growth factor stimulated 3D organoids to the *in vivo* developing mammary gland TEB was demonstrated to be strikingly similar. Both structures displayed features of reduced apico-basal polarity, a reduction in junctional complexes, multilayered epithelia and various cell morphologies within the stratified epithelium. Interestingly, this low polarity environment is highly similar to the previously documented morphogenesis of the mammary epithelia placode during embryogenesis (Hogg et al., 1983; Nanba et al., 2001). Further, a similar multilayered epithelia, or TEB, is involved in pubertal human mammary morphogenesis (Ozzello, 1971; Rudland, 1991). These data suggest that the semi-polarized epithelium of the TEB, which under growth factor stimulation initiates pubertal expansion of the mammary gland, utilizes the same programming for expansion as embryonic mammary gland morphogenesis.

The mammary epithelium is able to reconstruct itself multiple times during the lifespan. Research interests in processes that are involved in this reconstruction reflect the fact that both normal and neoplastic mammary epithelia undergo a reduction in polarity and adhesion while shifting from a simple to stratified epithelial organization. Epithelial to mesenchymal transition is the primary model for the expansion of mammary epithelial and neoplastic growth, the hallmarks of which are a reduction of polarity and acquisition of motility. Most models propose EMT occurs at epithelial-stromal or tumor-stromal border (Lee et al., 2011). However, our TEB data demonstrate it is actually the interior of the multilayered epithelium, which is out of contact with the ECM and stromal cells, where there is the largest reduction in polarity. In other words, the cells of the interior TEB seem to be the most motile and least physically connected of the tissue. Our results are consistent with models of a partial transient EMT (O'Brien et al., 2002). Furthermore, it is feasible to hypothesize that S1 acini are locked into a transient polarity state that possibly recapitulates the early stages of EMT for neoplasia.

Chapter 6.
Interference with actin polymerization in ex vivo mammary organoid mimics HMT-3522 T4-2 colonies

Introduction

The HMT-3522 cancer progression series has become widely utilized for insight into cancer therapeutic drug response and epithelial to mesenchymal transition. The HMT-3522 S1 acini are non-malignant EGF dependent human mammary epithelial cells with the ability to assemble a basement membrane in 3D cell culture (Briand et al., 1987). The series also includes the S1's derivative, the malignant and EGFR-independent T4-2 line, which descended from S1 cells following roughly 200 cell cycles *in vitro* (Briand et al., 1996). T4-2 cells grow continuously and invasively in 3D cell culture and become large masses of cells that loosely clump together but remain mostly spherical by observation via light microscopy. Having established that S1 acini ultrastructurally resemble primary mammary epithelial cell culture undergoing morphogenesis, we sought to determine whether the primary culture could be manipulated to mimic these malignant T4-2 cells.

The T4-2 cell cluster success as a model for malignant tumors led us to wonder if we could model malignant behavior through the growth factor stimulated *ex vivo* organoid. This would allow for a more direct study of malignant transformation in a tissue than achievable by typical single population 3D cell culture studies. While a single population of cells will expand to develop into a complex organized tissue, it is not well understood what long-lasting effects the starting point of a low density of cells may have on the outcome of the structure. To enable modeling in the most physiologically relevant system, we utilized the *ex vivo* organoid mammary morphogenesis previously described to provide the context of a normal tissue undergoing a normal transitive state before returning to normal. Disruptions of this process to produce a more malignant-like tumor will provide insight into the molecular and mechanical mechanisms at play.

We previously established that the transient morphogenesis of TEB is mimicked by the S1 acini and that both display a partial EMT. A large factor of the EMT is the reduction in polarity and appearance of intercellular spaces filled with membrane protrusions. We hypothesize that these membrane protrusions are actin-rich and disruption of actin polymerization may lead to malignant cell phenotypes. In the present study, we ultrastructurally characterize the disruption of the growth factor stimulated mammary organoid morphogenesis by inhibition of ROCK, Rac1 and MLCK. These results, in combination with an ultrastructural analysis of T4-2 colonies, shed light onto the underlying mechanisms of the epithelial to mesenchymal transition.

Experimental Procedures

Mouse models

Cre-lox E-cadherin

As described by (Shamir et al., 2013), the *ROSA26::Cre-ER^{T2}* transgenic line was a generous gift from Tamara Lotan (Johns Hopkins University). *E-cad$^{fl/fl}$, mT/mG*, and *ROSA26::LSL-rtTA-IRES-EGFP* mouse lines were acquired from the Jackson Laboratory.

HMT-3522 cell culture

2D cell culture: HMT-3522 T4-2 mammary epithelial cells (Briand et al 1987, 1996) were grown on Falcon tissue culture plastic flasks as two-dimensional (2D) monolayers in H14 medium (see Blaschke et al 1994). H14 medium is composed of DMEM:F12 medium (UCSF Cell Culture Facility) with 250ng/ml insulin (Sigma), 10ug/ml transferrin (Sigma), 2.6ng/ml sodium selenite (Sigma), 10^{-10} M estradiol (Sigma), 1.4 X 10^{-6} M hydrocortisone (Sigma) and 5ug/ml prolactin (Sigma). The T4-2 cells were propagated on collagen (Pure Col, Advanced Bio Matrix) coated Falcon tissue culture flasks.

3D cell culture: Three-dimensional (3D) cultures were constructed using confluent 2D monolayers of T4 cells. Cells were trypsinized with trypsin-EDTA (UCSF Cell Culture Facility), trypsin was quenched with Soybean Trypsin Inhibitor (SBTI, Sigma), cells were counted and the desired number of cells was spun down into a pellet. T4-2 cells are plated into 3D at 0.6 million cells per milliliter of matrigel. Each assay was composed with the appropriate number of pelleted cells (180K of T4-2) resuspended into 300ul of matrigel and pipetted into a 4-well Nunc plate ($1.9cm^2$/well) that had been pre-coated with 50ul of matrigel to prevent invasion to the bottom plastic surface. The matrigel assays were placed into a 37˚C incubator for 30 minutes for the matrigel to polymerize. The assays were fed with 500ul H14 medium. Assay medium was changed every 2-3 days. The assays were harvested after 10 days of growth.

Ex vivo organotypic culture

Epithelial fragments, "organoids", were generated and grown as described in Chapter 5.

Solutions and reagents for organotypic culture were as follows. DMEM (Dulbecco's modified Eagle's medium complete)/F12 (Gibco #11330). Collagenase solution consisted of: DMEM/F12, Fetal Bovine Serum (FBS, heat inactivated) (5% final), gentamicin (50 mg/mL), insulin (5 mg/mL final, Sigma I-5500), trypsin (2 mg/mL, Gibco #27250018), collagenase A (2 mg/mL, Type IV from Clostridium histolyticum, Sigma #C5138). DNAse I (Sigma #D4263) was resuspended at 4 U/mL in DMEM/F12. Bovine serum albumin (BSA; Invitrogen) was resuspended at 2.5 mg/mL in D-PBS. Basic medium: DMEM/F12, 1x Pen/Strep, 1x ITS (insulin, transferrin, sodium selenite, Sigma #I3146). Branching medium: Simple medium + 2.5 nM FGF2 (Sigma F0291). ROCK inhibitor (Y27632; Chemicon) and Rac-1 Inhibitor (NSC23766, Calbiochem) were used as indicated. All inhibitor experiments discussed in the text were done in FGF2 medium.

Tamoxifen-inducible Cre-mediated deletion

As described by (Shamir et al., 2013), Cre activity was induced in *Cre-ER;E-cad*$^{fl/fl}$*; mT/mG* epithelium by culturing organoids overnight with 50 nM tamoxifen once embedded in Matrigel. Tamoxifen will bind the ligand dependent Cre recombinase (Cre-estrogen receptor), causing the Cre to relocate into the nucleus where it can excise the lox-flanked target DNA, therefore deleting the gene of interest (E-cadherin). Following overnight incubation tamoxifen was then washed out and samples were cultured in fresh organoid medium. The tamoxifen-inducible system resulted in recombination in almost all cells without affecting branching morphogenesis.

Adenoviral delivery of Cre recombinase

As described by (Shamir et al., 2013), prior to embedment in Matrigel, mammary organoids were infected with Adeno-CMV-Cre (Vector Biolabs #1045) at a ratio of approximately $1x10^7$ PFU per 1,000 organoids. Infections were conducted in 50 µl of DMEM for 1-2 h at 37°C to yield recombination in 50-75% of cells. Percent recombination was raised by increasing viral titer or by overnight incubation with virus.

High-pressure freezing and freeze substitution

Samples were processed for high pressure freezing and freeze substitution as described in Chapter 5.

Transmission electron microscopy

70-100 nm sections were collected on formvar-coated grids and imaged as described in Chapter 5.

Desmosome quantification.

Desmosomes were counted among basally positioned cells in 5 *E-cad*$^{fl/fl}$ organoids and 4 *E-cad*$^{fl/+}$ organoids imaged by TEM. For each organoid, we selected 1-4 regions of 20-30 cells that were no more than 2 cells deep from the organoid-ECM interface. Regions were free of single-file invasion or epithelial buds. For desmosomes located between cells in the second and third layers deep to the surface, we counted the desmosome but not the third-layer cell. Adobe Photoshop CS4 was used to track the desmosomes and regions used for quantification.

3-dimensional SEM sample preparation

Samples were processed by the OTO-MW-HPF-FS method as described in Chapter 5.

Focused ion beam and Serial block face SEM

Focused ion beam and Serial block face SEM were performed as described in Chapter 4.

Antibody Staining

Antibody staining was performed as described in Chapter 5.

Confocal imaging

Confocal imaging was performed as described in Chapter 5.

Results

High pressure frozen freeze-substituted T4-2 3D cell cultures revealed a complex ultrastructure. Large intercellular gaps, the diameter of a cell or two, were not populated with membrane protrusions that usually occur between cells. When they were connected, the lateral and apical surfaces of adjacent cells touched by way of kissing points mediated by either desmosomes or plasma membranes alone. The basal surface of the colonies maintained a normal curvature but lacked a basement membrane. Also, along the basal surface is a proliferation of filamentous structures that protrude into the ECM. These protrusions were of various lengths, mostly appearing in irregular patterns but at times also as dense groups of small squat thin

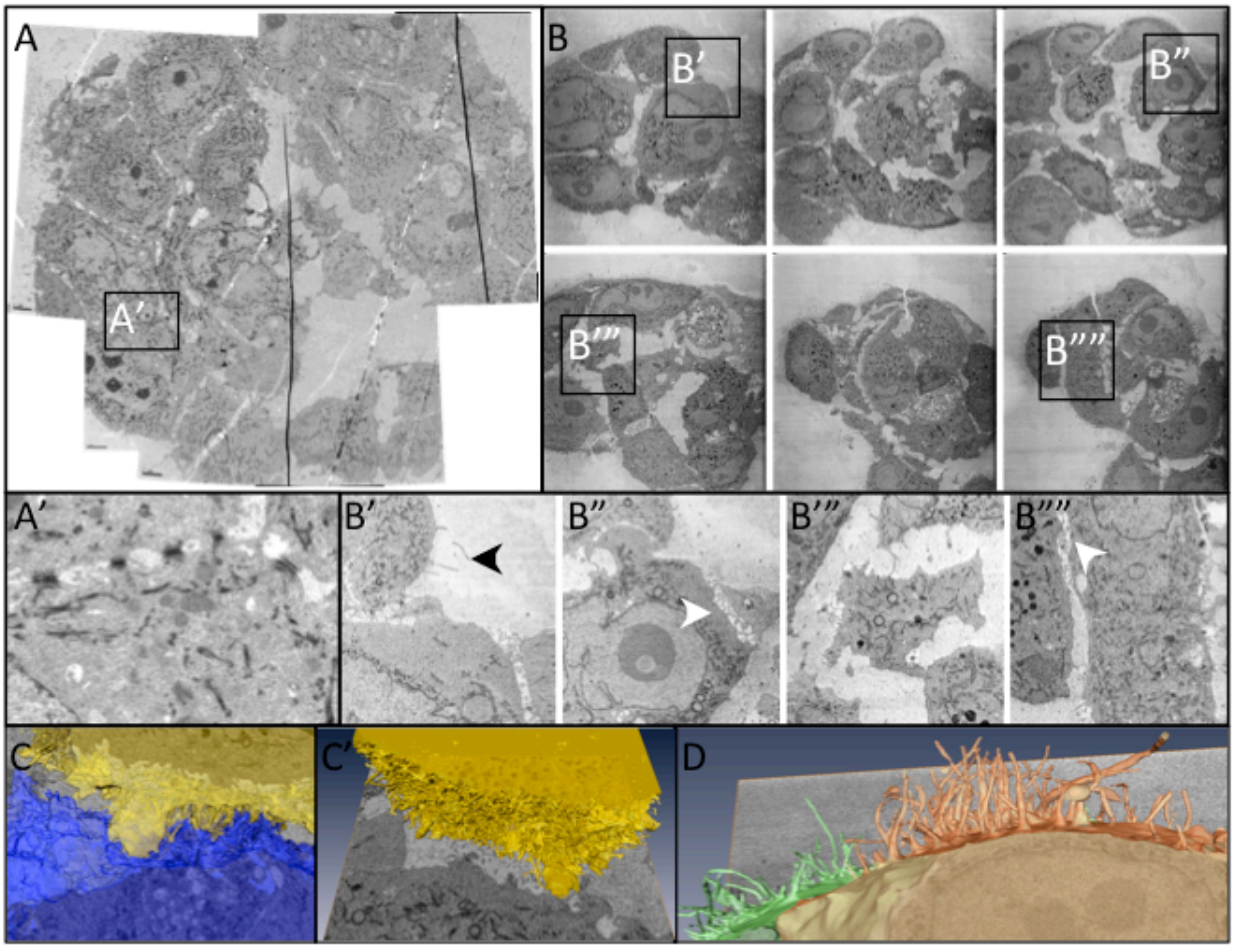

Figure 24. Ultrastructure of T4-2 colonies by TEM and 3D-SEM reveals disordered mass of cells. (A) TEM overview of a T4-2 colony highlights the heterogeneity of cell cohesiveness within one colony, displaying large regions of emptiness across which cells do not even come into contact; adjacent to those regions are (A') cell patches held together relatively tightly by desmosomes. 3D-SEM, serial block face imaging, exposed the entire colony as a conglomerate of loosely and tightly connected cells (B, each successive image is 12.5 μm deeper than the previous). (B') External facing, perpendicular protrusions are observed at intervals at the basal surface of the cells. (B") Areas of densely packed small protrusions are found within few intercellular spaces, and often occur directly next to large empty regions of intercellular space (B""). Large gaps within the center of the colony contain regions of cells that appear almost isolated from the surrounding cells (B'"). (C and C') Segmented 3D representations of the protrusions of the cell-cell interface. (D) Segmented 3D representations of the cell-ECM interface.

protrusions. Most of the basal protrusions extended at an angle directly perpendicular to the plasma membrane into the ECM. The protrusions along the intercellular space also appeared in patches rather than as a continuous layer. Frequently, nuclei had more than two nucleoli and the nuclear structure was highly irregular and invaginated. The shape of individual T4-2 cells that

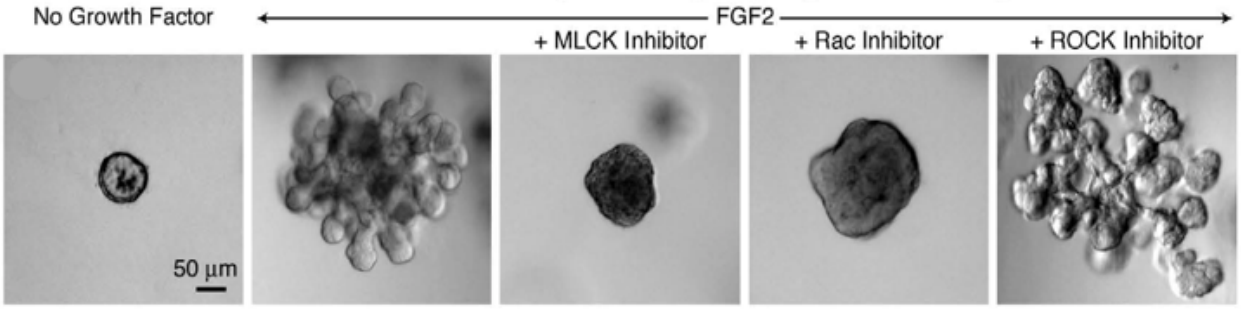

Figure 25. Light microscopy of drug treated primary mammary organoids. Organoids were growth factor stimulated prior to treatment with MLCK, Rac1 or ROCK inhibitors. For reference, organoid without growth factor stimulation is shown in the far left image, while the normal high branched growth factor stimulated organoid is second to far left. Drastic size differences of the drug treated organoids indicate there is a phenotype for these inhibitors.

make up an colony can no longer fit into simple descriptive terms like "round" or "elongated", as they were observed to be highly irregular polygonal shapes. These polygon shaped cells appeared to have no outside constraints defining their structure.

In order to test whether this ultrastructure could be induced in a physiologically similar terminal end bud of the *ex vivo* mammary organoid, we pharmacologically treated the organoids during morphogenesis. To test the direct inhibition of actin polymerization, we first treated the organoids with the inhibitor of Rho kinase (ROCK), Y27632. Exposure of the growth factor stimulated TEB to the pharmacological inhibitor Y27632 has been shown to cause hyperbranching in the multilayered epithelial structure and a reduction of E-cadherin (Ewald et al., 2008). Therefore, we predicted the Y27632 would cause a disruption of the cell-cell junctional complexes between luminal cells, specifically at sites of adherens and tight junctions.

We see this result in the confocal immunofluorescence of the treated TEB structures, in which upon treatment the lumen regresses and we observed disorder amongst the multilayered cells of the TEB. Staining for ZO-1, zona occludins protein 1, a molecular marker of adherens and tight junction complexes, changed from being exclusively localized at the apical surface of cells along a ductal structure to being either encapsulated in small separated puncta or not present at all. We also hypothesized that Y27632 would inhibit actin polymerization, thus disrupting the ubiquitous membrane protrusions observed in normal untreated TEB. TEM ultrastructural analysis of these Y27632 treated organoids revealed the incongruent nature of the connectivity between the cells, which was not apparent by confocal or light microscopy alone. In some regions, cells were connected by way of intercellular spaces containing some membrane protrusions. Yet in other regions, across large distances the cells were not connected to each other and mostly did not have membrane protrusions present on the cell surface. The membrane protrusions present were more often found to be branched and irregular in shape. In contrast to the ultrastructure of the T4-2 colonies, there were no observable membrane protrusions extending into the ECM.

The Y27632 treated TEB never re-formed bilayered simple epithelia, and instead they persisted as incongruous grape-like cell masses.

We also tested the myosin light chain kinase inhibitor ML-7, which inhibits the catalytic activity of MLCK (Saitoh et al., 1987), therefore blocking myosin II and endogenous contractility. Even with inhibition of MLCK, the organoids filled their lumen as normal and were

able to clear their lumens forming simple epithelia, but they did not initiate new branches. Lumens were lined with microvilli and sealed by tight junctions, desmosomes connected the cells laterally and small intercellular spaces were filled with membrane protrusions. Overall, the size of the structures were approximately 25% the size of the ROCK treated organoids. The cell shapes were limited to small cuboidal to round.

With inhibition of Rac1, with NSC23766, organoids still filled their lumens as normal; however, the multilayered epithelia persisted and did not clear the lumen and thus they did not return to a simple epithelium. TEM ultrastructural analysis revealed the cells connected through extensive interdigitating membrane protrusions and occasional small desmosomes. Between cells, few spaces no larger than the width of a cell are/were observed to be electron lucid but not full of membrane protrusions. Overall, the membrane protrusions were more prevalent in the Rac1 inhibited organoid than what was documented in the normal multilayered TEB. The cell shapes varied from small and round to large and elongated, and more often cells were the latter. Interestingly, we observed no protrusions into the ECM, as the cells maintained some basal polarity.

Finally, we suspected that the loss of cellular junctions could be preventing the T4-2, Rac1 and ROCK inhibited organoids from re-forming simple epithelia, leading us to directly alter the levels of E-cadherin and determine the ultrastructural consequences. Using a tamoxifen inducible Cre-lox system we deleted E-cadherin in an epithelial cell population before growing them into organoids. We used a Cre sensitive reporter to discriminate between cells that were expressing E-cadherin: the membrane-targeted tdTomato is expressed when the cell is not exposed to Cre recombinase, and membrane target EGFP is expressed when Cre recombinase has been used. Within the E-cadherin negative (E-cad$^{fl/fl}$) organoid population, >90% of cells did not express E-cadherin, as judged by EGFP expression. We consistently observed that E-cadherin negative cells self- sorted to the outside of the organoids, while the few remaining E-cadherin expressing cells sorted to center of the organoids. While the most outward cells of the multilayer organoid were E-cadherin negative, the cells did not disseminate into the ECM. Rather, by evaluation with light microscopy, only small clusters of cells appeared to protrude into the ECM before being ultimately re-absorbed into the main organoid cell cluster.

Using TEM ultrastructural analysis, we investigated the mechanism by which the cells remained cohesive in spite of lacking E-cadherin. TEM analysis of the E-cadherin negative organoids revealed interdigitating membranes and small desmosomes held the outermost cells together (Figure 28). While desmosomes were apparent between these cells, they were significantly reduced as compared to the control organoids, which had 3-fold more desmosomes for the same area of cells measured. Two types of small cell clusters were observed protruding into the ECM: cell clusters and single file invasions. The first, more prevalent type was characterized by small clusters of cells that formed half circular knobs on the outside of the organoid. For some of these the basal surface of these cells remained smooth, with no observable membrane protrusions into the ECM. In others, the cell clusters appeared to have patches of short membrane protrusions extending into the ECM. The interface between the cell cluster and the organoid was often bridged by membrane protrusions. The single file invasion phenotype was differentiated by the appearance of individual cells stacked in a line protruding out into the ECM. The outermost surface of these structures occasionally had membrane protrusions extending into the ECM. The cell-cell interfaces of the single file invasion were sometimes

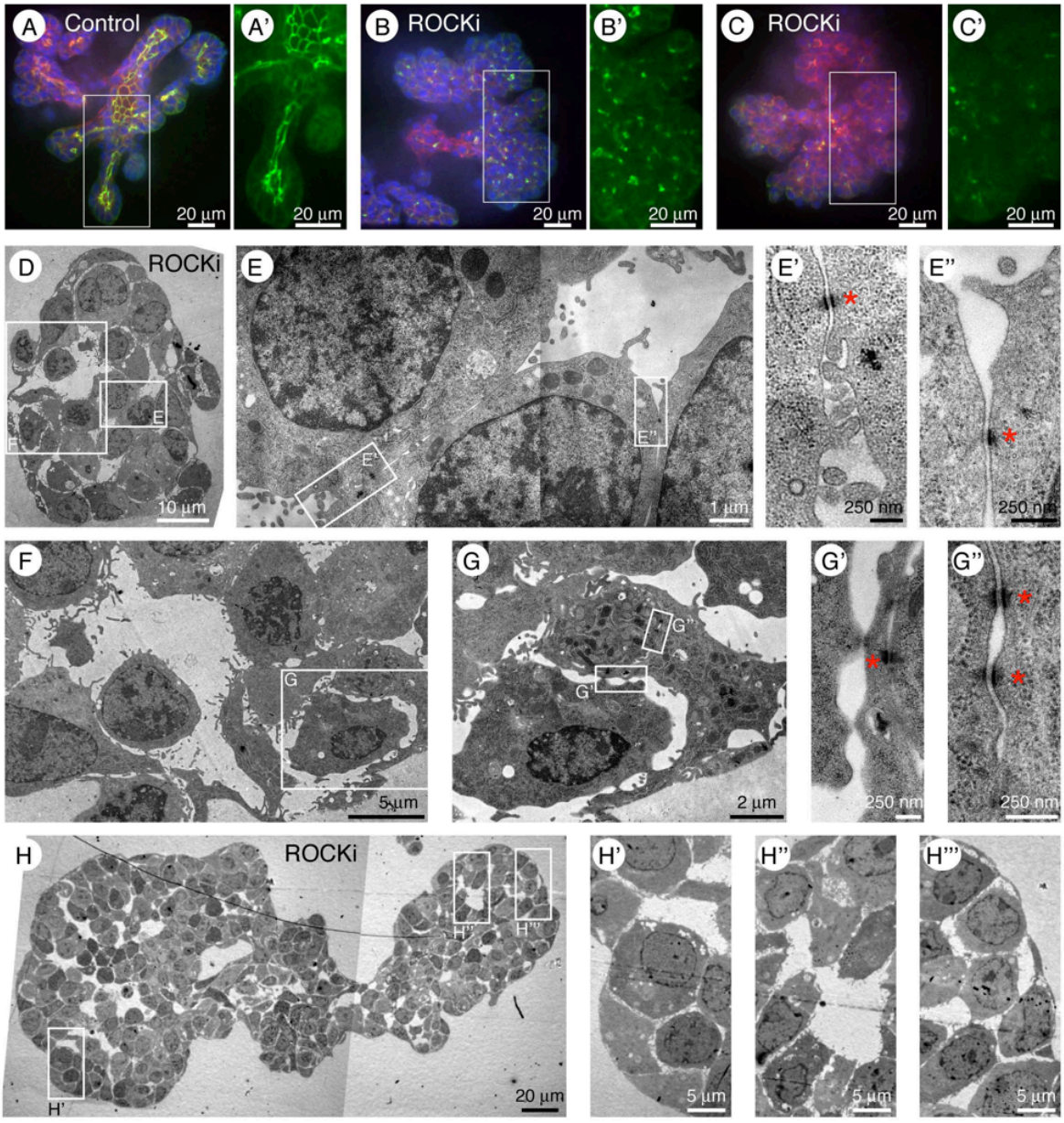

Figure 26. ROCK inhibition leads to loosely connected cellular masses with reduced apico-basal polarity. (A-C') Confocal microscopy evaluation demonstrates that compared to normal TEB (A, A'), Y-27632 treatment leads to reduction of ZO-1, which is observed as discrete puncta (B, B'). However, large regions without ZO-1 puncta were also observed (C, C') [red, phalloidin; green, ZO-1; blue, nuclei]. Analysis of ROCK-inhibited TEB by TEM revealed no electron dense lumen, and cells connected exclusively via desmosomes and membrane protrusions (D-H"'). Desmosomes, usually small, were often flanked by membrane protrusions (E-E", G'-G"). Large electron lucid gaps between cells were observed (F, G, H"), with occasional protrusions extending into the empty spaces. Y-27632 treated TEB did extend out into the ECM (H) to form structures up to 10x larger than the un-stimulated organoids; however, examination of the basal surface in contact with the ECM revealed no extracellular protrusions into the ECM (H"').

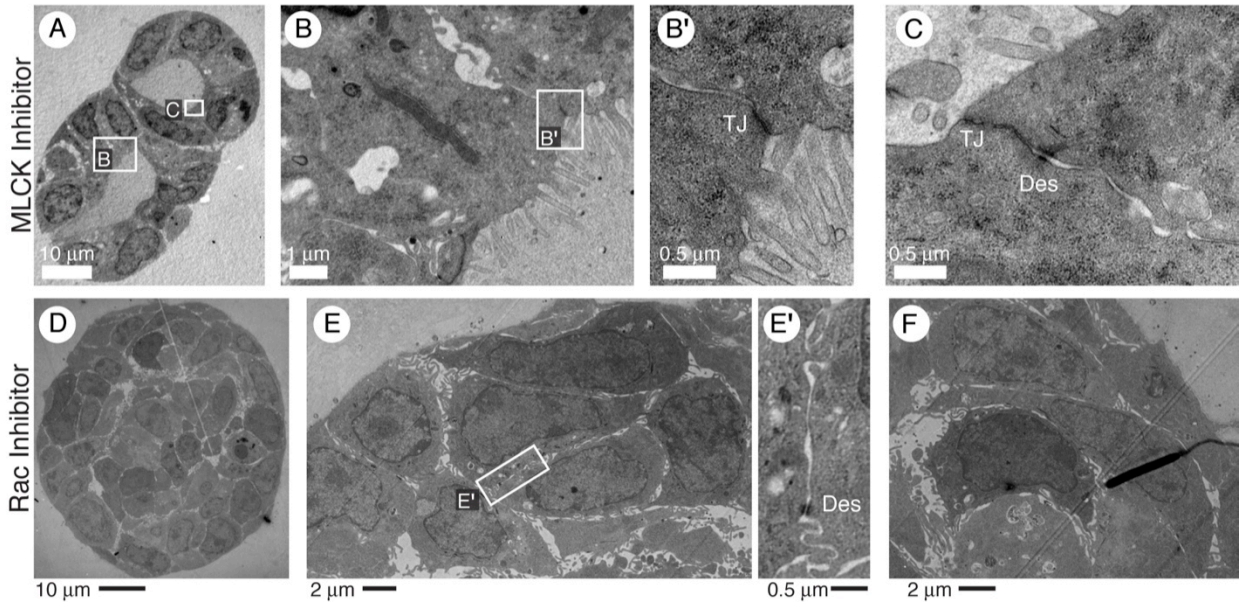

Figure 27. Rac1 and MCLK inhibition produces altered ultrastructure in growth factor stimulated TEBs. (A-C) MLCK inhibited TEBs will eventually develop into a single epithelium with tight-junction sealed lumen. However, these structures are significantly smaller in size than normal, as they appear to have reduced cell division and reduced expansion into the ECM. Intercellular spaces with membrane protrusions are observed at lateral cell interfaces and no protrusions are observed extending into the ECM. (D-F) Rac1 inhibition leads to a persistent multilayered epithelium closely resembling the size and ultrastructure of the normal transiently multilayered TEB. However, the Rac1 inhibited organoids do not form lumen or return to polarized epithelia. Extensive branching and interdigitated membrane protrusions are observed on every interior facing cell surface, while no protrusions are observed extending into the ECM.

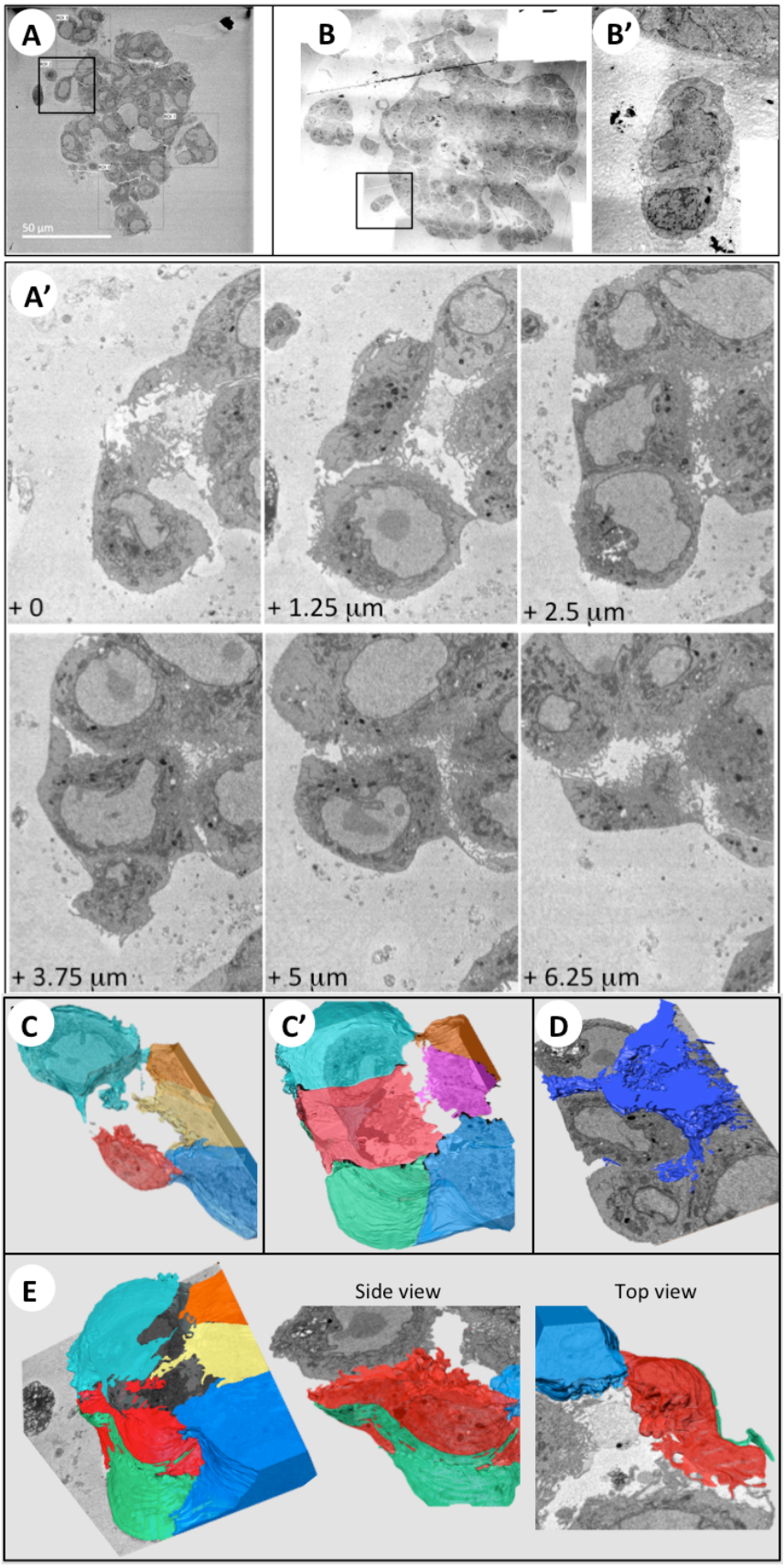

Figure 28. Knock out of E-cadherin produces small clusters of cells that protrude into the ECM. 3D-SEM, serial block face imaging (A-A'), and TEM (B-B') of these E-cadherin -/- organoids revealed protruding cell clusters extending from the basal surface of the organoids. The clusters were initially assessed by TEM (B-B') where we often observed isolate small clusters of cells not connected to the main organoid (B'). To directly investigate how these cell clusters were connected to the main organoid and cell-cell interactions of the clusters, we employed 3D-SEM (A-A'). (A') A series of images from a 10 µm data stack reveal these clusters to be lines of single cells protruding into the ECM that can retain some small connections to the main organoid mediated by membrane protrusions. 3D volumetric reconstructions of these cells highlight the few connections maintained with the main organoid (C – C'). The large gap between the single file invasion and the main organoid is displayed volumetrically in (D). (E) Often we observed a cell within the single file invasion wrapping around the adjacent cell with thin broad cellular extensions; this is especially visible in the top view of (E).

connected by immature desmosomes with no membrane protrusions between the cells. However, in these cases we did observe particularly long membrane protrusions on the outside edge of the single file cells, positioned in a fashion where one cell's protrusion would wrap around the outside of the adjacent cell. In other single file invasion examples, we observed small tufts of membrane protrusion in contact with the ECM.

We investigated these single file invasions with 3D-SEM, serial block face imaging. Interestingly, we observed these single file invasions were still in contact with the organoid, albeit only over a small portion of the structure. This contact was mediated solely by extensive membrane protrusions of a variety of lengths.

Discussion

Having previously discovered that the nonmalignant HMT-3522 S1 acini closely resembled *ex vivo* mammary epithelial terminal end buds during branching morphogenesis, we hypothesized that this normal physiological process could be manipulated to mimic the ultrastructure of T4-2. Defining the conditions around this transformation could provide insight into the mechanical and molecular features of epithelial to mesenchymal transition, which leads to malignant and invasive cell behavior. To this end, we focused our efforts on attempting to disrupt the ubiquitous membrane protrusions observed in the intercellular spaces of the S1 acini and normal TEB. The structures are likely filopodial protrusions and therefore rely on actin polymerization to form. Another target was disruption of cell polarity by elimination of E-cadherin expression, which ties the cell-cell adherens junction into the terminal web of actin. Loss of E-cadherin is often associated with EMT and breast cancer and is known to be dysregulated in T4-2 cells (Anders et al., 2003)].

A difficult series of questions to answer involve the annotation of the variety of membrane protrusions we have observed with the specific types of actin-rich membrane protrusions described by two-dimensional cell culture. While we are not the first to identify and wonder about these types of membrane protrusions, the question of their function and designation remains an open one. Furthermore, there remains the question of the impact of these membrane protrusions on normal or neoplastic cells in a state of semi-polarization (normal TEB, S1 acini) or complete unpolarization (T4-2). Here we have sought to begin to identify some of the molecular factors that may be involved with the regulation of these membrane protrusions in a complex 3D environment that simulates *in vivo* conditions.

The ultrastructure of the HMT-3522 T4-2 colonies had some unexpected features, namely the reduction in membrane protrusions present within intercellular spaces and the surprising level of cohesiveness within the entire colony, considering the invasive nature of the cells. We also were surprised by the heterogeneity of cohesiveness within the colonies; some areas of the cell clusters contained cells as tightly linked as in the nonmalignant S1 acini, while in other areas cells were loosely connected or not connected at all across large areas. In more closely connected cells, there remained intercellular spaces with occasional patches of small membrane protrusions. In line with the invasive potential of the cells, we anticipated and observed long membrane protrusions that extended, perpendicular to the colony, into the ECM.

Treatment of the *ex vivo* mammary organoids with ROCK inhibitor (Y27632) produced cysts with distinct ultrastructural similarities with the T4-2 colonies. The RhoA effector, RhoA

kinase (ROCK), works to initiate and stabilize focal adhesions and stress fibers through inhibition of myosin light chain phosphatase or by directly phosphorylating myosin light chain, resulting in activation of myosin II (Amano et al., 1996; Kimura et al., 1996; Leung et al., 1995). Thus, by inhibiting ROCK, we expected the resulting organoids to have fewer cell contacts, as the cells would lack the ability to form some cellular adhesions and mechanically sense their environment. Cell-cell junctions were in fact reduced following ROCK treatment, and cells lacked any ultrastructural signs of polarization. Furthermore, the cell shapes and occurrence of membrane protrusions closely mimicked those found in the T4-2 colonies. The structures diverged, however, when comparing the cell-ECM interface, as the ROCK inhibited organoids did not appear to produce any membrane protrusions that extended into the ECM, nor did the ROCK inhibited cells disseminate into the ECM, as is the case occasionally with T4-2 cells (Rizki et al., 2008; Weaver et al., 1997). The similarity between the interiors of these two structures is intriguing, in light of the fact that T4-2 cells express high levels of RhoA and ROCK (Paszek et al., 2005). In fact, ROCK inhibition in T4-2 cells produces a cyst that appears, by our assessment of the two studies results, more structurally similar to the non-malignant S1 acinus (Paszek et al., 2005).

ROCK is known to compensate for myosin light chain kinase (MLCK), therefore it was not surprising that MLCK-inhibition (ML7) produced only subtle changes in the organoid (Amano et al., 1996). The MLCK inhibited organoids formed multilayered transitional epithelia and were able to clear lumen and reform polarized simple epithelia. However, interestingly the overall size of the organoid changed little from the un-stimulated epithelial cyst; there were far fewer cells in the resulting MLCK inhibited organoids compared to the simple epithelia of growth factor stimulated organoids. Nor were the MLCK inhibited organoids capable of branching morphogenesis to extend ducts into the ECM. This result suggests that although Rho kinase can activate myosin II in the absence of MLCK, it is unable to fully compensate for MLCK. MLCK is necessary for expansion for mammary branching and likely to be involved in activating cell proliferation signaling networks.

Unlike MLCK inhibited organoids, Rac1 inhibition (NSC2376) produced the intriguing effect of more pronounced membrane protrusions within intercellular spaces of cysts that were unable to return to polarized epithelia. Rac1 inhibited organoids remained multilayered epithelia, strikingly similar to the normally transient TEB. Cells were connected only through interdigitating membrane protrusions and desmosomes. Rac1 has been demonstrated to play a role in establishing polarity in epithelial cells by organizing laminin deposition (O'Brien et al., 2001), thus its loss may explain why these cells do not reform a polarized epithelium. Again there is a wide range of cell shapes present, including many elongated cells implying a motile mesenchymal behavior. Rac1 has been shown to regulate motility in elongated, mesenchymal-like cells by signaling through WAVE/Arp2/3 to form cellular extensions; specifically, fibrosarcoma cells grown in collagen1 3D matrix (Yamazaki et al., 2005). Further, Rac1 inhibition led to a mesenchymal to amoeboid (round) transition in these cells. Recently, it has been demonstrated that different types of 3D cell culture media, particularly collagen1 matrix versus cell-derived matrix, can cause drastic biochemical and structural shifts in the mechanism of cell motility and polarity for cell movement (Petrie et al., 2012). It remains to be determined whether a similar phenomenon may be occurring in our study, as Rac1 inhibition did not affect cell shape, but did inhibit cell polarity and lumen formation.

Chapter 7.
Summary

The use of cell culture systems as tools for the study of dynamic cellular processes hinges on the faithful recapitulation of those cell dynamics within the cell culture. It has become well accepted that cell dynamics undergo different biochemical and structurally based changes when viewed in two-dimensional versus three-dimensional growth conditions; and that for many cells, epithelial cells in particular, a 3D matrix is necessary to recreate normal cell dynamics. Less widely accepted yet equally important is the need to validate the structural recapitulation of the small-scale tissue in 3D cell culture as structural changes indicate signaling differences. Too often confocal and immunofluorescence are used as stand-ins for TEM ultrastructural analysis; however, the inherent drawbacks of these systems, low resolution and user-biased feature imaging, can generate biased results that may obscure the larger pictures of the data. In pursuit of ultrastructural characterization of the HMT-3522 S1 cell line grown in 3D cell culture, we were surprised to discover the quite unpolarized nature of what had been previously reported to be highly polarized tissue. Our results were so surprisingly off-target, we thought it best to validate our methodology before proceeding with further studies.

The use of an entire zebrafish embryo for an ultrastructural-based comparison of different TEM sample preparation methods corroborated our suspicion that what we observed of the S1 acini was in fact representative of cells grown in 3D cell culture. The analysis across a range of tissues within the zebrafish provided evidence that cryo-immobilization based HPF-FS was the best method of preparing tissue for TEM analyses. The two chemical-fixation based conventional methods were adequate substitutes for most tissues, although these did produce well-known and easily identifiable artifacts on occasion such as membrane blebbing, protein aggregation and extraction. Using these results as a guide, we decided to create a protocol that would produce well preserved, artifact free, robust back-scattered electron content for 3D-SEM imaging. The 3D-SEM techniques require samples to be laden with heavy atoms, to a larger degree than TEM, for well contrasted data collection. The repeated applications of osmium tetroxide requires the sample undergo chemical fixation and staining, thus HPF-FS is not necessarily the first choice in modalities. However, we sought to reduce the artifacts created by chemical dehydration and reduce the length of time of exposure to chemicals for the samples. Thus combining the microwave-assisted and high pressure freezing freeze substitution approaches immediately appealed to our desired goals. The use of microwaves reduced exposure time of the chemical reagents 10 fold and the freeze substitution processing provided a way to eliminate dehydration artifacts. Testing of multiple staining protocols, most of which were developed in the 19060s-1980s, lead us to conclude that the OTO approach was viable and robust for BSE staining. The OTO-MW-HPF-FS protocol has subsequently been successfully applied to multiple sample types, including bacterial colonies and zebrafish, and requires little optimization between samples.

Having confirmed that the HPF-FS technique was ideal for preservation across a variety of tissues, we decided to test this method on an array of epithelial tissue relevant to the HMT-3522 series. We began this by investigating the ultrastructure of both wild type mouse mammary tissue *in vivo* and *ex vivo* primary tissue culture of mouse mammary glands. Our results demonstrated the efficacy of HPF-FS for faithful preservation of these tissues, again indicating the validity of our S1 acini ultrastructure results. We continued with the *ex vivo* mammary organoid samples as a way to easily investigate the phenomena of branching morphogenesis and

its ultrastructure. By induction with growth factors, we stimulated branching morphogenesis to investigate the structure of the terminal end bud in primary culture mammary gland cysts in 3D ECM culture. The terminal end bud is the site of ductal expansion into the ECM and remains an area of intense focus due to the potential for better understanding of the epithelial mesenchymal transition, which is thought to occur within the TEB. Ultrastructural analysis of the TEB revealed a semi-polarized organization of the multilayered epithelium. The inner-most layer of luminal cells maintained an apical polarization in which a microvilli-lined lumen was sealed off from the basal side of the cell by tight junctions. At the base of these cells, continuous across the multilayer epithelia, and up the basal surface of the outer most layer of cells in contact with the ECM, were cells with few cell-cell junctional complexes, the most proliferative being desmosomes, and large electron lucid intercellular spaces filled with membrane protrusions.

Upon the discovery of the electron lucid intercellular spaces filled with irregular membrane protrusions, we were at once reminded of the S1 acini structure and organization. Analysis of the membrane protrusions required a 3D imaging approach, beyond just 2D TEM projection imaging. Initially, we tried to visualize the membrane protrusion by serial section TEM, but this proved to be too inconsistent due to mechanical and human error. The method was lacking in the z-dimension resolution and failed to produce even a visual assessment of the membrane protrusion phenomena. We also applied TEM tomography and found this method quite limited in x- and y- dimension information as we could collect data on only a few protrusions due to technical limitations. Finally, we developed and tested a sample preparation method, OTO MW-HPF-FS, which allowed for high-resolution 3D study of the membrane protrusions and other features by way of serial block face and focused ion beam imaging, 3D-SEM techniques. This further analysis revealed the overall structure, size and shape, of the membrane protrusions to be highly varied. We found membrane protrusions to be between 50 and 200 nm in diameter and 100 and 2500 nm in length. The membrane protrusions were observed to often be interdigitated similar to fingers or hands holding together. Often the membrane protrusion would develop a bi-forked, sometimes a multi-forked, appearance in the latter end of the structure. At times protrusions appeared actin-rich, and other times it was more difficult to distinguish a filamentous pattern within. This is not inherent evidence of parallel, branched or not actin content, as some conditions of EM sample preparation can degrade actin, but we may use the global information provided by the TEM and 3D-SEM to enable conclusions.

To further investigate the role of these membrane protrusions within the TEB, we treated them with a series of inhibitors that disrupted actin polymerization. Treatment of the organoids with a Rac1 inhibitor produced multilayered epithelial cysts filled with roundish cells that never produced lumen, had few cell-cell junctions, flourished with intercellular spaces filled with membrane protrusions, and were surrounded by well formed basal lamina. ROCK inhibitor treatment generated multilayered epithelial cysts that were filled with large irregularly shaped gaps between loosely connected cells, no lumen and surrounded by a well formed basement membrane; cells were only connected via few cell-cell junctions, and while the amounts of intercellular spaces between cells were similar to those in the control, there was a significant reduction in the amount of membrane protrusions present. Production of organoids with at least 90% of cells lacking E-cadherin expression resulted in multilayered cysts with E-cadherin negative cells self-sorted to the outside of the structure. These cells, which we expected would undergo dissemination into the surrounding matrix, remained adhered to the cyst and only migrated out into the matrix via single file invasion with a single row of cells, 1 to 3 cells long,

protruding into the matrix. These single file invasive cells were tightly bound by interdigitating membrane protrusions and a few immature desmosomes.

We speculated/investigated if any of these perturbations of the TEB structure would be manifested in the HMT-3522 S1 and T4-2 cancer progression model. We prepared the malignant T4-2, a spontaneous derivation of the S1 cell line that is epidermal growth factor independent, for ultrastructural analysis. The architecture of the T4-2 colonies strongly resembled the ROCK inhibitor treated TEB. T4-2 colonies contain large gaps and the cells are loosely connected by desmosomes and have fewer membrane protrusions within the intercellular spaces than observed in S1 acini. Occasionally, within or toward the outside of the large grape-like T4-2 cyst, we observed small compact regions of organization similar to the order seen in the S1 acinus. Again, further analysis of the S1 acinar organization reveals basal surface polarity but no apical or lateral polarity. The S1 acinar structure is strongly reminiscent of the TEB organization.

From these data, we conclude that membrane protrusions may function in maintaining cell connectivity in mammary epithelia during events of semi- or non- polarity and are disrupted by Rho kinase inhibition. A difficult series of questions to answer involve the annotation of the variety of membrane protrusions we have observed with the specific types of actin-rich membrane protrusions described by two-dimensional cell culture. While we are not the first to identify and wonder about these types of membrane protrusions, the question of their function and designation remains an open one. To achieve a full understanding of each piece of the puzzle, tightly controlled experimental conditions are necessary. However, upon searching through the vast literature on membrane protrusions, the lack of consensus between data on different protrusion structures and the lack of clarity for which of these actin-mediated membrane protrusions are relevant *in vivo* is striking. To that end, future studies must carefully consider the environment in which these structures are studied and strive to validate findings made in 2D cell culture with *in vivo* systems.

The importance of the proper physiologically relevant 3D environment is supported by recent evidence that demonstrates differences in cell migration of fibroblasts grown in cell derived matrix and pure collagen 1 matrix (Petrie et al., 2012). Petrie et al., defined a form of protrusion called, lobopodia, which appeared as membrane blebs from all sides of the cells grown in three-dimensional linear elastic cell derived matrix. In 3D collagen1 matrix, nonlinear elasticity, the fibroblast lamellipodia-based motility was observed. With lobopodial motility the fibroblasts expression of Rac1, Cdc42 and RhoA were nonpolarized across the cell surface even though the cell moved directionally toward a chemotactic agent and Rac1 and Cdc42 were localized toward the leading edge (Petrie et al., 2012). Studying these membrane protrusions in a native environment may help unify the definitions of some of these structures (i.e. podosomes and invadopodia, microvilli and filopodia) and reveal the spectrum of mechanotransduction upon which each structure uniquely exists. An intriguing example of the convergent nature of these membrane protrusions is the overlap in molecular make-up and structure between filopodia and microvilli (Khurana and George, 2011). As suggested by the wide-range of data reviewed, the actin-bundling proteins villin and fascin may be responsible for the formation of microvilli and filopodia in polarized and non-polarized epithelial cells, respectively, and may provide good targets for disrupting their formation.

Careful studies of these structures are needed to fully understand the mechanical and biochemical role they are playing in epithelium dynamics. Data integrating multiple streams of experimental results covering biomarkers, fluorescent localization and high-resolution ultrastructure will be required to build a complete picture of membrane protrusion activity.

Cited Literature

Abramoff Magelhaes, P. J., Ram, S. J., M. D. (2004). Image Processing with ImageJ. *Biophotonics* **11**, 36–42.

Amano, M., Ito, M., Kimura, K., Fukata, Y., Chihara, K., Nakano, T., Matsuura, Y. and Kaibuchi, K. (1996). Phosphorylation and activation of myosin by Rho-associated kinase (Rho-kinase). *The Journal of biological chemistry* **271**, 20246–9.

Amatruda, J. F., Shepard, J. L., Stern, H. M. and Zon, L. I. (2002). Zebrafish as a cancer model system. *Cancer Cell* **1**, 229–231.

Anders, M., Hansen, R., Ding, R.-X., Rauen, K. a, Bissell, M. J. and Korn, W. M. (2003). Disruption of 3D tissue integrity facilitates adenovirus infection by deregulating the coxsackievirus and adenovirus receptor. *Proceedings of the National Academy of Sciences of the United States of America* **100**, 1943–8.

Armer, H. E. J., Mariggi, G., Png, K. M. Y., Genoud, C., Monteith, A. G., Bushby, A. J., Gerhardt, H. and Collinson, L. M. (2009). Imaging transient blood vessel fusion events in zebrafish by correlative volume electron microscopy. *PloS one* **4**, e7716.

Austin, C. D., Mazie, A. M. De, Pisacane, P. I., Dijk, S. M. Van, Eigenbrot, C., Sliwkowski, M. X., Klumperman, J. and Scheller, R. H. (2004). Endocytosis and Sorting of ErbB2 and the Site of Action of Cancer Therapeutics Trastuzumab and Geldanamycin □. *Molecular Biology of the Cell* **15**, 5268–5282.

Avanesov, A. and Malicki, J. (2010). Analysis of the retina in the zebrafish model. *Methods in cell biology* **100**, 153–204.

Belton, C. M. (1979). Application of ruthenium red ligand binding of osmium: Scanning electron microscopy of larval tapeworms. *Micron* **10**, 1–4.

Briand, P., Petersen, O. W. and Deurs, B. (1987). A new diploid nontumorigenic human breast epithelial cell line isolated and propagated in chemically defined medium. *In Vitro Cellular & Developmental Biology* **23**, 181–188.

Briand, P., Nielsen, K. V., Madsen, M. W. and Petersen, O. W. (1996). Trisomy 7p and Malignant Transformation of Human Breast Epithelial Cells following Epidermal Growth Factor Withdrawal Trisomy 7p and Malignant Transformation of Human Breast Epithelial Cells following Epidermal Growth Factor Withdrawal. *Cancer Research* **56**, 2039–2044.

Bryant, D. M. and Mostov, K. E. (2008). From cells to organs : building polarized tissue. *Nat Rev Mol Cell Biol* **9**, 887–901.

Cardona, A., Saalfeld, S., Preibisch, S., Schmid, B., Cheng, A., Pulokas, J., Tomancak, P. and Hartenstein, V. (2010). An integrated micro- and macroarchitectural analysis of the

Drosophila brain by computer-assisted serial section electron microscopy. *PLoS biology* **8**, 17.

Carre, AH, Horne, A. (1927). An Investigation of the Behaviour of Pectic Materials in Apples and other Plant Tissues. 1. *Annals of Botony* **XLL**,.

Chen, W. T. (1989). Proteolytic activity of specialized surface protrusions formed at rosette contact sites of transformed cells. *The Journal of experimental zoology* **251**, 167–85.

Daniel, C. W. and Smith, G. H. (1999). The mammary gland: a model for development. *Journal of mammary gland biology and neoplasia* **4**, 3–8.

Danilchik, M. V and Brown, E. E. (2008). Membrane dynamics of cleavage furrow closure in Xenopus laevis. *Developmental dynamics : an official publication of the American Association of Anatomists* **237**, 565–79.

David-Pfeuty, T. (1980). Altered Distributions of the Cytoskeletal Proteins Vinculin and alpha - actinin in Cultured Fibroblasts Transformed by Rous Sarcoma Virus. *Proceedings of the National Academy of Sciences* **77**, 6687–6691.

Debnath, J., Muthuswamy, S. K. and Brugge, J. S. (2003). Morphogenesis and oncogenesis of MCF-10A mammary epithelial acini grown in three-dimensional basement membrane cultures. *Methods* **30**, 256–268.

Denk, W. and Horstmann, H. (2004). Serial block-face scanning electron microscopy to reconstruct three-dimensional tissue nanostructure. *PLoS biology* **2**, e329.

DeRosier, D. J. and Tilney, L. G. (2000). F-Actin Bundles Are Derivatives of Microvilli: What Does This Tell US about How Bundles Might Form? *The Journal of Cell Biology* **148**, 1–6.

Dohnalkova, a, Kennedy, D., Mancuso, J., Marshall, M., Mainwaring, P. and Fredrickson, J. (2010). High-Throughput 3D Visualization of Large Volumes at High Resolution by 3ViewTM. *Microscopy and Microanalysis* **16**, 1870–1871.

Dooley, K. (2000). Zebrafish: a model system for the study of human disease. *Current Opinion in Genetics & Development* **10**, 252–256.

Eckert, M. a, Lwin, T. M., Chang, A. T., Kim, J., Danis, E., Ohno-Machado, L. and Yang, J. (2011). Twist1-induced invadopodia formation promotes tumor metastasis. *Cancer cell* **19**, 372–86.

Edelstein, A., Amodaj, N., Hoover, K., Vale, R. and Stuurman, N. (2010). Computer control of microscopes using μManager. *Current protocols in molecular biology* **Chapter 14**, 14–20.

Ewald, A. J. (2013a). Isolation of mouse mammary organoids for long-term time-lapse imaging. *Cold Spring Harbor protocols* **2013**, 130–3.

Ewald, A. J. (2013b). Practical considerations for long-term time-lapse imaging of epithelial morphogenesis in three-dimensional organotypic cultures. *Cold Spring Harbor protocols* **2013**, 100–17.

Ewald, A. J., Brenot, A., Duong, M., Chan, B. S. and Werb, Z. (2008). Collective epithelial migration and cell rearrangements drive mammary branching morphogenesis. *Developmental Cell* **14**, 570–81.

Ewald, A. J., Huebner, R. J., Palsdottir, H., Lee, J. K., Perez, M. J., Jorgens, D. M., Tauscher, A. N., Cheung, K. J., Werb, Z. and Auer, M. (2012). Mammary collective cell migration involves transient loss of epithelial features and individual cell migration within the epithelium. *Journal of cell science* **125**, 2638–54.

Fournier, M. V, Martin, K. J., Kenny, P. A., Xhaja, K., Bosch, I., Yaswen, P. and Bissell, M. J. (2006). Gene expression signature in organized and growth-arrested mammary acini predicts good outcome in breast cancer. *Cancer research* **66**, 7095–102.

Friedl, P. and Gilmour, D. (2009). Collective cell migration in morphogenesis, regeneration and cancer. *Nature reviews. Molecular cell biology* **10**, 445–57.

Friedman, P. L. and Ellisman, M. H. (1981). Enhanced visualization of peripheral nerve and sensory receptors in the scanning electron microscope using cryofracture and osmium-thiocarbohydrazide-osmium impregnation. *Journal of neurocytology* **10**, 111–31.

Galbraith, C. G., Yamada, K. M. and Galbraith, J. A. (2007). Polymerizing actin fibers position integrins primed to probe for adhesion sites. *Science* **315**, 992–995.

Giberson, R. T. and Demaree, R. S. (1995). Microwave fixation: Understanding the variables to achieve rapid reproducible results. *Microscopy Research and Technique* **32**, 246–254.

Gibson, M. C. and Perrimon, N. (2003). Apicobasal polarization: epithelial form and function. *Current Opinion in Cell Biology* **15**, 747–752.

Gimona, M., Buccione, R., Courtneidge, S. A. and Linder, S. (2008). Assembly and biological role of podosomes and invadopodia. *Current opinion in cell biology* **20**, 235–41.

Hayat, M. A. (2000). *Principles and Techniques of Electron Microscopy: Biological Applications*. Cambridge University Press.

Hernandez-Verdun, D., Roussel, P., Thiry, M., Sirri, V. and Lafontaine, D. L. J. (2010). The nucleolus: structure/function relationship in RNA metabolism. *Nucleolus* **1**, 415–31.

Hinck, L. and Silberstein, G. B. (2005). Key stages in mammary gland development: the mammary end bud as a motile organ. *Breast cancer research : BCR* **7**, 245–51.

Hogg, N. a, Harrison, C. J. and Tickle, C. (1983). Lumen formation in the developing mouse mammary gland. *Journal of embryology and experimental morphology* **73**, 39–57.

Hovey, R. C., Trott, J. F. and Vonderhaar, B. K. (2002). Establishing a framework for the functional mammary gland: from endocrinology to morphology. *Journal of mammary gland biology and neoplasia* **7**, 17–38.

Hurd, T. W., Gao, L., Roh, M. H., Macara, I. G. and Margolis, B. (2003). Direct interaction of two polarity complexes implicated in epithelial tight junction assembly. *Nature cell biology* **5**, 137–42.

Ilina, O. and Friedl, P. (2009). Mechanisms of collective cell migration at a glance. *Journal of cell science* **122**, 3203–8.

Johnson, N., Krebs, M., Boudreau, R., Giorgi, G., Legros, M., Larabell, C. and Krebs, Á. M. (2003). Actin-filled nuclear invaginations indicate degree of cell. *Differentiation* **71**, 414–424.

Jongebloed, W. L., Stokroos, I., Kalicharan, D. and Want, J. J. L. Van Der (1999a). Is cryopreservation superior over tannic acid / arginine / osmium tetroxide non-coating preparation in field emission scanning electron microscopy ? *Scanning Microscopy* **13**, 93–109.

Jongebloed, W. L., Stokroos, I., Van der Want, J. J. and Kalicharan, D. (1999b). Non-coating fixation techniques or redundancy of conductive coating, low kV FE-SEM operation and combined SEM/TEM of biological tissues. *Journal of microscopy* **193**, 158–70.

Kenny, P. A., Lee, G. Y., Myers, C. A., Neve, R. M., Semeiks, J. R., Spellman, P. T., Lorenz, K., Lee, E. H., Barcellos-hoff, M. H., Petersen, O. W., et al. (2007). The morphologies of breast cancer cell lines in three-dimensional assays correlate with their profiles of gene expression. *Molecular Oncology* **1**, 84–96.

Khurana, S. and George, S. P. (2011). The role of actin bundling proteins in the assembly of filopodia in epithelial cells. *Cell adhesion & migration* **5**, 409–20.

Kimura, K., Ito, M., Amano, M., Chihara, K., Fukata, Y., Nakafuku, M., Yamamori, B., Feng, J., Nakano, T., Okawa, K., et al. (1996). Regulation of myosin phosphatase by Rho and Rho-associated kinase (Rho-kinase). *Science* **273**, 245–8.

Lange, K. (2011). Fundamental role of microvilli in the main functions of differentiated cells: Outline of an universal regulating and signaling system at the cell periphery. *Journal of cellular physiology* **226**, 896–927.

Lee, G. Y., Kenny, P. A., Lee, E. H. and Bissell, M. J. (2007). Three-dimensional culture models of normal and malignant breast epithelial cells. *Nature Methods* **4**, 359–365.

Lee, K., Gjorevski, N., Boghaert, E., Radisky, D. C. and Nelson, C. M. (2011). Snail1, Snail2, and E47 promote mammary epithelial branching morphogenesis. *The EMBO journal* **30**, 2662–74.

Leong, A. S.-Y., Daymon, M. E. and Milios, J. (1985). Microwave irradiation as a form of fixation for light and electron microscopy. *The Journal of Pathology* **146**, 313–321.

Leser, V., Drobne, D., Pipan, Z., Milani, M. and Tatti, F. (2009). Comparison of different preparation methods of biological samples for FIB milling and SEM investigation. *Journal of microscopy* **233**, 309–19.

Leung, T., Manser, E., Tan, L. and Lim, L. (1995). A novel serine/threonine kinase binding the Ras-related RhoA GTPase which translocates the kinase to peripheral membranes. *The Journal of biological chemistry* **270**, 29051–4.

Lieschke, G. J. and Currie, P. D. (2007). Animal models of human disease: zebrafish swim into view. *Nature reviews. Genetics* **8**, 353–67.

Linder, S. (2007). The matrix corroded: podosomes and invadopodia in extracellular matrix degradation. *Trends in cell biology* **17**, 107–17.

Lo, A. T., Mori, H., Mott, J. and Bissell, M. J. (2012). Constructing three-dimensional models to study mammary gland branching morphogenesis and functional differentiation. *Journal of mammary gland biology and neoplasia* **17**, 103–10.

Login, G. R., Dwyer, B. K. and Dvorak, A. M. (1990). Rapid primary microwave-osmium fixation. I. Preservation of structure for electron microscopy in seconds. *Journal of Histochemistry & Cytochemistry* **38** , 755–762.

Luft, J. H. (1971a). Ruthenium Red and Violet: Part II. *The Anatomical Record* **171**, 369–416.

Luft, J. H. (1971b). Ruthenium Red and Violet: Part I. *The Anatomical Record* **171**, 347–368.

Madsen, M. W., Lykkesfeldt, A. E., Laursen, I., Nielsen, K. V. and Briand, P. (1992). Altered Gene Expression of c-myc, Epidermal Growth Factor Receptor, Transforming Growth Factor-{alpha}, and c-erb-B2 in an Immortalized Human Breast Epithelial Cell Line, HMT-3522, Is Associated with Decreased Growth Factor Requirements. *Cancer Res.* **52**, 1210–1217.

McConnell, R. E. and Tyska, M. J. (2007). Myosin-1a powers the sliding of apical membrane along microvillar actin bundles. *The Journal of cell biology* **177**, 671–81.

McDonald, K. (1999). High-pressure freezing for preservation of high resolution fine structure and antigenicity for immunolabeling. *Methods Mol Biol* **117**, 77–97.

McDonald, K. (2007). Cryopreparation methods for electron microscopy of selected model systems. *Methods Cell Biol* **79**, 23–56.

McDonald, K. and Auer, M. (2006). High-pressure freezing, cellular tomography, and structural cell biology. *Biotechniques* **41**, 137, 139, 141.

McDonald, K. and Muller-Reichert, T. (2002). Cryomethods for thin section electron microscopy. *Methods Enzymol* **351**, 96–123.

McDonald, K. L. and Webb, R. I. (2011). Freeze substitution in 3 hours or less. *Journal of microscopy* **243**, 227–33.

McDonald, K., Schwarz, H., Müller-Reichert, T., Webb, R., Buser, C. and Morphew, M. (2010). "Tips and tricks" for high-pressure freezing of model systems. *Methods in cell biology* **96**, 671–93.

Mikula, S., Binding, J. and Denk, W. (2012). Staining and embedding the whole mouse brain for electron microscopy. *Nature methods* **9**, 1198–1203.

Moor, H. (1987). *Cryotechniques in Biological Electron Microscopy*. Berlin, Heidelberg: Springer Berlin Heidelberg.

Muller-Reichert, T., Hohenberg, H., O'Toole, E. T. and Mcdonald, K. (2003). Cryoimmobilization and three-dimensional visualization of C. elegans ultrastructure. *Journal of Microscopy* **212**, 71–80.

Munroe, P. R. (2009). The application of focused ion beam microscopy in the material sciences. *Materials Characterization* **60**, 2–13.

Murphy, D. a and Courtneidge, S. a (2011). The "ins" and "outs" of podosomes and invadopodia: characteristics, formation and function. *Nature Reviews Molecular Cell Biology* **12**, 413–26.

Nanba, D., Nakanishi, Y. and Hieda, Y. (2001). Changes in adhesive properties of epithelial cells during early morphogenesis of the mammary gland. *Development, Growth and Differentiation* **43**, 535–544.

Nelson, C. M. and Bissell, M. J. (2005). Modeling dynamic reciprocity: engineering three-dimensional culture models of breast architecture, function, and neoplastic transformation. *Seminars in cancer biology* **15**, 342–52.

Neve, R. M., Chin, K., Fridlyand, J., Yeh, J., Baehner, F. L., Fevr, T., Clark, L., Bayani, N., Coppe, J.-P., Tong, F., et al. (2006). A collection of breast cancer cell lines for the study of functionally distinct cancer subtypes. *Cancer cell* **10**, 515–27.

O'Brien, L. E., Jou, T. S., Pollack, a L., Zhang, Q., Hansen, S. H., Yurchenco, P. and Mostov, K. E. (2001). Rac1 orientates epithelial apical polarity through effects on basolateral laminin assembly. *Nature cell biology* **3**, 831–8.

O'Brien, L. E., Zegers, M. M. P. and Mostov, K. E. (2002). Opinion: Building epithelial architecture: insights from three-dimensional culture models. *Nature reviews. Molecular cell biology* **3**, 531–7.

Oakes, S. R., Rogers, R. L., Naylor, M. J. and Ormandy, C. J. (2008). Prolactin regulation of mammary gland development. *Journal of mammary gland biology and neoplasia* **13**, 13–28.

Orkin, R. W. (1977). A murine tumor producing a matrix of basement membrane. *Journal of Experimental Medicine* **145**, 204–220.

Ounjai, P., Kim, K. D., Liu, H., Dong, M., Tauscher, A. N., Witkowska, H. E. and Downing, K. H. (2013). Architectural insights into a ciliary partition. *Current biology : CB* **23**, 339–44.

Ozzello, L. (1971). Ultrastructure of the human mammary gland. *Pathology annual* **6**, 1–59.

Paszek, M. J., Zahir, N., Johnson, K. R., Lakins, J. N., Rozenberg, G. I., Gefen, A., Reinhart-King, C. a, Margulies, S. S., Dembo, M., Boettiger, D., et al. (2005). Tensional homeostasis and the malignant phenotype. *Cancer cell* **8**, 241–54.

Petersen, O. W., Rønnov-Jessen, L., Howlett, a R. and Bissell, M. J. (1992). Interaction with basement membrane serves to rapidly distinguish growth and differentiation pattern of normal and malignant human breast epithelial cells. *Proceedings of the National Academy of Sciences of the United States of America* **89**, 9064–8.

Petrie, R. J., Gavara, N., Chadwick, R. S. and Yamada, K. M. (2012). Nonpolarized signaling reveals two distinct modes of 3D cell migration. *The Journal of cell biology* **197**, 439–55.

Pettersen, E. F., Goddard, T. D., Huang, C. C., Couch, G. S., Greenblatt, D. M., Meng, E. C. and Ferrin, T. E. (2004). UCSF Chimera—A visualization system for exploratory research and analysis. *Journal of Computational Chemistry* **25**, 1605–1612.

Pitelka, D. R., Hamamoto, S. T., Duafala, J. G. and Nemanic, M. K. (1973). Cell contacts in the mouse mammary gland: I. Normal gland in postnatal development and the secretory cycle. *The Journal of Cell Biology* **56**, 797–818.

Potter, C. R. and Quatacker, J. (1993). The p185 erbB2 protein is localized on cell organelles involved in cell motility. *Clinical & Experimental Metastasis* **11**, 453–461.

Prewett, P. D. (1984). Focused ion beam systems for materials analysis and modification. *Vacuum* **34**, 931–939.

Raich, W. B., Agbunag, C. and Hardin, J. (1999). Rapid epithelial-sheet sealing in the Caenorhabditis elegans embryo requires cadherin-dependent filopodial priming. *Current biology : CB* **9**, 1139–46.

Reyntjens, S. and Puers, R. (2001). A review of focused ion beam applications in microsystem technology. *Journal of Micromechanics and Microengineering* **11**, 287.

Rigort, A., Bäuerlein, F. J. B., Villa, E., Eibauer, M., Laugks, T., Baumeister, W. and Plitzko, J. M. (2012). Focused ion beam micromachining of eukaryotic cells for cryoelectron tomography. *PNAS* **109**, 4449–54.

Rizki, A., Weaver, V. M., Lee, S.-Y., Rozenberg, G. I., Chin, K., Myers, C. a, Bascom, J. L., Mott, J. D., Semeiks, J. R., Grate, L. R., et al. (2008). A human breast cell model of preinvasive to invasive transition. *Cancer research* **68**, 1378–87.

Robertson, D., Monaghan, P., Clarke, C. and Atherton, A. J. (1992). An appraisal of low-temperature embedding by progressive lowering of temperature into Lowicryl HM20 for immunocytochemical studies. *Journal of Microscopy* **168**, 85–100.

Rubino, S., Akhtar, S., Melin, P., Searle, A., Spellward, P. and Leifer, K. (2012). A site-specific focused-ion-beam lift-out method for cryo Transmission Electron Microscopy. *Journal of Structural Biology* **180**, 572–576.

Rudland, P. S. (1991). Generation of lobuloalveolar development from isolated rat mammary ducts and end buds. *J Histochem Cytochem 1991*.

Ruijter, E. T., Miller, G. J., Aalders, T. W., Van de Kaa, C. A., Schalken, J. A., Debruyne, F. M. and Boon, M. E. (1997). Rapid microwave-stimulated fixation of entire prostatectomy specimens. Biomed-II MPC Study Group. *The Journal of pathology* **183**, 369–75.

Russo, J. and Russo, I. H. (2004). Development of the human breast. *Maturitas* **49**, 2–15.

Rzadzinska, A. K., Schneider, M. E., Davies, C., Riordan, G. P. and Kachar, B. (2004). An actin molecular treadmill and myosins maintain stereocilia functional architecture and self-renewal. *The Journal of cell biology* **164**, 887–97.

Saalfeld, S., Cardona, A., Hartenstein, V. and Tomančák, P. (2010). As-rigid-as-possible mosaicking and serial section registration of large ssTEM datasets. *Bioinformatics* **26**, i57–63.

Saitoh, M., Ishikawa, T., Matsushima, S., Naka, M. and Hidaka, H. (1987). Selective inhibition of catalytic activity of smooth muscle myosin light chain kinase. *J. Biol. Chem.* **262**, 7796–7801.

Schmid, B., Schindelin, J., Cardona, A., Longair, M. and Heisenberg, M. (2010). A high-level 3D visualization API for Java and ImageJ. *BMC bioinformatics* **11**, 274.

Schoumacher, M., Goldman, R. D., Louvard, D. and Vignjevic, D. M. (2010). Actin, microtubules, and vimentin intermediate filaments cooperate for elongation of invadopodia. *The Journal of cell biology* **189**, 541–56.

Schroeder-Reiter, E., Pérez-Willard, F., Zeile, U. and Wanner, G. (2009). Focused ion beam (FIB) combined with high resolution scanning electron microscopy: a promising tool for 3D analysis of chromosome architecture. *Journal of structural biology* **165**, 97–106.

Schwarz, H. and Humbel, B. M. (2007). Correlative light and electron microscopy using immunolabeled resin sections. *Methods in molecular biology* **369**, 229–56.

Seligman, AM, Wasserkrug, HL, Hanker, J. (1966). A new staining method (OTO) for enhancing contrast of lipid-containing membranes and droplets in osmium tetroxide-fixed tissue with osmiophilic thiocarbohydrazide (TCH). *Journal Of Cell Biology* **Aug**, 424–32.

Serebriiskii, I., Castelló-Cros, R., Lamb, A., Golemis, E. A. and Cukierman, E. (2008). Fibroblast-derived 3D matrix differentially regulates the growth and drug-responsiveness of human cancer cells. *Matrix biology : journal of the International Society for Matrix Biology* **27**, 573–85.

Shamir, E. R., Jorgens, D. M., Coutinho, K., Tsai, W.-T., Aziz, K., Auer, M., Tran, P. T. and Ewald, A. J. (2013). Distinct roles for E-cadherin and Twist1 in epithelial invasion and dissemination. *Nature cell biology* **Submitted** ,.

Shibue, T., Brooks, M. W., Inan, M. F., Reinhardt, F. and Weinberg, R. a. (2012). The Outgrowth of Micrometastases Is Enabled by the Formation of Filopodium-like Protrusions. *Cancer Discovery* **2**, 706–721.

Sosinsky, G. E., Crum, J., Jones, Y. Z., Lanman, J., Smarr, B., Terada, M., Martone, M. E., Deerinck, T. J., Johnson, J. E. and Ellisman, M. H. (2008). The combination of chemical fixation procedures with high pressure freezing and freeze substitution preserves highly labile tissue ultrastructure for electron tomography applications. *J Struct Biol* **161**, 359–371.

Stalling, D., Westerhoff, M. and Hege, H. (2005). Amira: A Highly Interactive System For Visual Data Analysis. *The visualization handbook* **38**, 749–67.

Steffen, A., Faix, J., Resch, G. P., Linkner, J., Wehland, J., Small, J. V., Rottner, K. and Stradal, T. E. B. (2006). Filopodia formation in the absence of functional WAVE- and Arp2/3-complexes. *Molecular biology of the cell* **17**, 2581–91.

Sternlicht, M. D., Kouros-Mehr, H., Lu, P. and Werb, Z. (2006). Hormonal and local control of mammary branching morphogenesis. *Differentiation* **74**, 365–381.

Stradalova, V., Gaplovska-Kysela, K. and Hozak, P. (2008). Ultrastructural and nuclear antigen preservation after high-pressure freezing/freeze-substitution and low-temperature LR White embedding of HeLa cells. *Histochem Cell Biol* **130**, 1047–1052.

Svitkina, T. M. and Borisy, G. G. (1999). Arp2/3 Complex and Actin Depolymerizing Factor/Cofilin in Dendritic Organization and Treadmilling of Actin Filament Array in Lamellipodia. *The Journal of Cell Biology* **145**, 1009–1026.

Tanentzapf, G., Smith, C., McGlade, J. and Tepass, U. (2000). Apical, lateral, and basal polarization cues contribute to the development of the follicular epithelium during Drosophila oogenesis. *The Journal of cell biology* **151**, 891–904.

Tarone, G., Cirillo, D., Giancotti, F. G., Comoglio, P. M. and Marchisio, P. C. (1985). Rous sarcoma virus-transformed fibroblasts adhere primarily at discrete protrusions of the ventral membrane called podosomes. *Experimental Cell Research* **159**, 141–157.

Thiry, M., Cheutin, T., Donohue, M. F. O., Kaplan, H., Ploton, D., Thiry, M., Cheutin, T., Donohue, M. O. and Kaplan, H. (2000). Dynamics and three-dimensional localization of ribosomal RNA within the nucleolus. *RNA* 1750–1761.

Thiry, M., Lamaye, F. and Lafontaine, D. L. J. (2011). The nucleolus: When two became three. *Nucleus* **2:4**, 289–293.

Tolde, O., Rösel, D., Veselý, P., Folk, P. and Brábek, J. (2010). The structure of invadopodia in a complex 3D environment. *European journal of cell biology* **89**, 674–80.

Triffo, W. J., Palsdottir, H., McDonald, K. L., Lee, J. K., Inman, J. L., Bissell, M. J., Raphael, R. M. and Auer, M. (2008). Controlled microaspiration for high-pressure freezing: a new method for ultrastructural preservation of fragile and sparse tissues for TEM and electron tomography. *J Microsc* **230**, 278–287.

Underwood, J. M., Imbalzano, K. M., Weaver, V. M., Fischer, A. H., Imbalzano, A. N. and Nickerson, J. A. (2006). The Ultrastructure of MCF-10A Acini. *Journal of Cellular Physiology* **208**, 141–148.

Vasioukhin, V., Bauer, C., Yin, M. and Fuchs, E. (2000). Directed Actin Polymerization Is the Driving Force for Epithelial Cell–Cell Adhesion. *Cell* **100**, 209–219.

Vermeer, P. D., Einwalter, L. A., Moninger, T. O., Rokhlina, T., Kern, J. A., Zabner, J. and Welsh, M. J. (2003). Segregation of receptor and ligand regulates activation of epithelial growth factor receptor. *Nature* **422**, 322–6.

Wang, F., Weaver, V. M., Petersen, O. W., Larabell, C. A., Dedhar, S., Briand, P., Lupu, R. and Bissell, M. J. (1998). Reciprocal interactions between NL 1-integrin and epidermal growth factor receptor in three-dimensional basement membrane breast cultures : A different perspective in epithelial biology. *Proc Natl Acad Sci U S A* **95**, 14821–14826.

Wang, L., Humbel, B. M. and Roubos, E. W. (2005). High-pressure freezing followed by cryosubstitution as a tool for preserving high-quality ultrastructure and immunoreactivity in the Xenopus laevis pituitary gland. *Brain Res Brain Res Protoc* **15**, 155–163.

Watson, C. J. (2006). Involution: apoptosis and tissue remodelling that convert the mammary gland from milk factory to a quiescent organ. *Breast cancer research* **8**, 203–208.

Weaver, V. M., Howlett, A. R., Langton-Webster, B., Petersen, O. W. and Bissell, M. J. (1995). The development of a functionally relevant cell culture model of progressive human breast cancer. *Semin Cancer Biol* **6**, 175–184.

Weaver, V. M., Fischer, A. H., Peterson, O. W. and Bissell, M. J. (1996). The importance of the microenvironment in breast cancer progression: recapitulation of mammary tumorigenesis using a unique human mammary epithelial cell model and a three-dimensional culture assay. *Biochem Cell Biol* **74**, 833–851.

Weaver, V. M., Petersen, O. W., Wang, F., Larabell, C. a, Briand, P., Damsky, C. and Bissell, M. J. (1997). Reversion of the malignant phenotype of human breast cells in three-dimensional culture and in vivo by integrin blocking antibodies. *The Journal of cell biology* **137**, 231–45.

Weaver, V. M., Lelièvre, S., Lakins, J. N., Chrenek, M. a, Jones, J. C. R., Giancotti, F., Werb, Z. and Bissell, M. J. (2002). Beta4 Integrin-Dependent Formation of Polarized Three-Dimensional Architecture Confers Resistance To Apoptosis in Normal and Malignant Mammary Epithelium. *Cancer cell* **2**, 205–16.

Webster, P. (2007). Microwave-assisted processing and embedding for transmission electron microscopy. *Methods in molecular biology (Clifton, N.J.)* **369**, 47–65.

Wendt, K. D., Jensen, C. A., Tindall, R. and Katz, M. L. (2004). Comparison of conventional and microwave-assisted processing of mouse retinas for transmission electron microscopy. *Journal of Microscopy* **214**, 80–88.

Westerfield, M. (2000). *The Zebrafish Book*. University of Oregon press.

White, D. L., Mazurkiewicz, J. E. and Barrnett, R. J. (1979). A chemical mechanism for tissue staining by osmium tetroxide-ferrocyanide mixtures. *Journal of Histochemistry & Cytochemistry* **27**, 1084–1091.

Wierzbicki, R., Køber, C., Jensen, M. R. B., Lopacińska, J., Schmidt, M. S., Skolimowski, M., Abeille, F., Qvortrup, K. and Mølhave, K. (2013). Mapping the complex morphology of cell interactions with nanowire substrates using FIB-SEM. *PloS one* **8**, e53307.

Willingham, M. C. and Rutherford, a. V. (1984). The use of osmium-thiocarbohydrazide-osmium (OTO) and ferrocyanide-reduced osmium methods to enhance membrane contrast and preservation in cultured cells. *Journal of Histochemistry & Cytochemistry* **32**, 455–460.

Yamazaki, D., Kurisu, S. and Takenawa, T. (2005). Regulation of cancer cell motility through actin reorganization. *Cancer science* **96**, 379–86.